Revised for *J. Non-Newtonian Fluid Mech.* February 25, 1999

DYNAMICS OF WEAKLY STRAIN-HARDENING FLUIDS IN FILAMENT STRETCHING DEVICES

Minwu Yao
Ohio Aerospace Institute, Brook Park, Ohio 44142 U.S.A.

Stephen H. Spiegelberg and Gareth H. McKinley
Department of Mechanical Engineering, M.I.T.,
77 Massachusetts Ave, Cambridge, MA 02139 USA

Key Words: Extensional flow, Fluid dynamics,
Finite element method, Liquid bridge,
Filament stretching device, Viscoelasticity,
Giesekus model, Moving boundary problem,
Considère theory

Address for Proofs: Prof. Gareth H. McKinley
Massachusetts Institute of Technology
Room 3-250
77 Massachusetts Avenue
Cambridge, MA 02139-4307 U.S.A.
Tel: (617) 258-0754
Fax: (617) 258-8559
E-mail: gareth@mit.edu

ABSTRACT

We investigate the transient viscoelastic response of weakly strain-hardening fluids to imposed elongational deformation in filament stretching devices. We combine time-dependent finite-element simulations with quantitative experimental measurements on a rheologically well-characterized test fluid to investigate how well the device reproduces the ideal transient uniaxial extensional viscosity predicted theoretically. A concentrated polymer solution containing 5.0 wt.% monodisperse polystyrene is used as the test fluid and the experiments are conducted using the filament stretching rheometer developed by Spiegelberg et al. The axisymmetric numerical simulations incorporate the effects of viscoelasticity, surface tension, fluid inertia and a deformable free surface. Single and multi-mode versions of the Giesekus constitutive equation are used to model the rheology of the shear-thinning test fluid. Excellent agreement between the measured transient Trouton ratio and the numerical predictions over a range of deformation rates is reported. The numerical simulations also reveal some important aspects of the fluid kinematics exhibited by weakly strain-hardening fluids during stretching; including a rapid necking of the filament diameter near the axial mid-plane of the fluid column, and an associated elastic recoil phenomenon near the rigid end-plates. This necking instability of a viscoelastic filament can be understood through a generalized Considère criterion, as recently documented by Hassager et al. As a consequence of this necking, spatial and temporal homogeneity in the extensional deformation of the filament is never achieved, even at large Hencky strains. This is in sharp contrast to the numerical and experimental studies for strongly strain-hardening dilute polymer solutions that have been reported to date. Nonetheless, the present computational rheology study shows that filament stretching devices can still be used to accurately extract the transient extensional viscosity function for weakly strain-hardening fluids, provided that the evolution history of the tensile force at the end-plate and the filament radius at the mid-plane are carefully measured and that the experimental data are correctly processed.

1. INTRODUCTION

The kinematics of many industrial applications, such as fiber-spinning, injection molding, extrusion and film coating operations, are often dominated by extensional deformations. Accurate design calculations and numerical simulations for such processes therefore require detailed knowledge of the dynamical response of viscoelastic fluids in strong extensional flows, and the use of constitutive models which faithfully reproduce the experimentally measured data. The filament stretching device pioneered by Matta & Tytus [1] and Sridhar et al. [2] is one of the most promising experimental techniques that has been developed for providing accurate measurements of the transient extensional viscosity for polymer solutions. Numerous variants of such devices are currently being developed worldwide by several research groups: Tirtaatmadja & Sridhar [3], Berg et al. [4], Spiegelberg & McKinley [5], Solomon and S.J. Muller [6], Koelling et al. [7], van Nieuwkoop & Muller von Czernicki [8] and Verhoef et al. [9].

In the filament stretching apparatus, a cylindrical liquid column is first generated between two concentric circular plates and then elongated by pulling one or both of the end-plate fixtures at an exponentially-increasing rate. It is hoped that the resulting flow kinematics in the liquid column approximate an ideal uniaxial elongational flow; the extensional viscosity function is determined from the axial force at the end-plate which is measured as a function of time, and the total Hencky strain applied to the material is computed from the total stretch imposed on the sample [10].

Accompanying the rapid proliferation of filament stretching rheometers, theoretical and numerical efforts have been devoted to studying the complex time-dependent free-surface extensional deformations which are generated in such devices. In a pioneering numerical study using a free-surface finite element method and the Oldroyd-B model, Shipman et al. [11] simulated one of the low-extension-rate falling-plate experiments conducted by Sridhar & co-workers [2]. Reasonable agreement in terms of free surface shapes was obtained; however, numerical difficulties limited the range of calculations. Gaudet et al. [12] used the boundary element method to perform a quasi-steady analysis of a Newtonian fluid filament constrained between two rigid disks (i.e. a 'liquid bridge') for a wide range of aspect ratios and capillary numbers. In this study the end-plates were separated linearly in time rather than in the exponential manner employed in filament stretching rheometers. The effects of exponential separation and the role of viscoelastic stresses have also recently been investigated using the boundary element method [13].

Finite element calculations of elongating liquid bridges were performed by Yao and McKinley [14] using the Oldroyd-B model to investigate the extensional dynamics of highly elastic materials such as Boger fluids. Profiles showing the evolution of free surface shape and kinematics within the

fluid filament were presented, and the resulting evolution of the polymeric contribution to the total tensile stress was studied in detail. Similar calculations have also been performed by Sizaire et al. [15] using several variants of the finitely extensible non-linear elastic (FENE) dumbbell model, and by Kolte et al. [16] using an integral model of K-BKZ type. By integrating the momentum equation over the upper half of an elongating liquid bridge, Szabo [17] has recently derived a complete force balance for the liquid filament incorporating the tensile stress differences, the shear stress and the inertial accelerations in the fluid, plus the curvature of the free surface.

From the experimental and numerical studies of filament stretching devices outlined above, the overall picture of the evolution of the axial elongation of a liquid column exhibiting pronounced strain-hardening is now clear. The key observations may be summarized as follows:

i) At short times or small Hencky strains ($\varepsilon \equiv \dot{\varepsilon} t \leq 2$), the kinematics generated by the device are non-homogeneous and consist of a uniaxial elongation plus an additional shearing contribution arising from the no-slip boundary condition imposed at the rigid end-plates. The stresses in the fluid arise predominately from the Newtonian solvent, and the filament evolution is well-described by a lubrication approximation similar to that derived for radial squeeze-flows.

ii) For Deborah numbers $De > 0.5$, strain hardening occurs beyond $\varepsilon \approx 2$. Strain hardening is manifested by three observations: 1) a change in the slope of the mid-point radius vs. time; 2) the filament radius becomes progressively more axially uniform; and 3) there is a concomitant rapid increase in the tensile stress in the filament. The strain hardening behavior predicted in simulations agrees well with available experimental observations [3–9]. The pronounced strain hardening leads to an increasingly homogeneous extensional deformation at large strains. Measurements of the extensional viscosity based on the assumption of homogeneous kinematics are then appropriate. Kolte et al. [16] show that with careful time-resolved measurements of both the tensile stress difference and the local rate of extensional deformation, filament stretching devices can provide an accurate measure of the transient stress growth function in uniaxial elongation.

iii) At very large strains $\varepsilon \geq 3.5$, the large tensile stresses in the mid-region of the column inhibit further elongation and the fluid reservoirs near either rigid end-plate are rapidly drained of fluid. This can lead to non-monotonic axial variations in the local free surface shape, and the combined effects of the large elastic stresses and sharp interfacial curvature leads experimentally to the onset of a local elastic instability. Two-dimensional numerical calculations of free surface evolution [14,16] agree well with the experimental observations [18] at large strains prior to the onset of the axisymmetry-breaking instability. Recent three-dimensional

time-dependent calculations with the Upper-Convected Maxwell model have also been able to simulate the growth of periodic azimuthal perturbations near the end-plates [19]

In contrast to the failure mechanism described in (iii) above, Newtonian fluids exhibit no strain-hardening and the elongating filaments always develop a concave shape with a narrow neck connecting two quasi-static fluid reservoirs near the rigid end-plates. As the axial length of the filament is increased, the radius of the fluid column will decrease towards zero at some position at, or near, the axial mid-point of the fluid column and two unconnected fluid regions will be formed, each attached to one of the rigid disks. The precise location and dynamic evolution of this capillary-driven failure depend on the relative importance of the surface tension, the viscosity of the inner and outer fluid [12] and the fluid inertia [20].

A similarity solution for this finite-time mathematical singularity incorporating capillary and viscous stresses plus fluid inertia has been given by Eggers & Dupont and a detailed review of such mechanisms has recently appeared [21]. In general, the tensile stresses that develop during exponential stretching of a cylindrical column of a viscous Newtonian liquid help to stabilize the capillarity-driven Rayleigh instability [22]. In a filament stretching device, this stabilization shifts the capillary-driven necking instability to high Hencky strains, and experiments [5] and numerical simulations [14,16] have shown that it is possible to obtain the expected Trouton ratio of 3 for viscous Newtonian filaments at moderate strains ($2 \leq \varepsilon \leq 4$). Indeed, in the absence of surface tension, it has been proven theoretically [23] that a filament of viscous Newtonian fluid does not 'fail' (i.e. break) in a finite time

The experiments and calculations performed to date suggest that it is now possible to use filament stretching devices to systematically investigate differences in the extensional rheology of different fluid formulations, e.g. the effect of concentration and solvent quality. However, it is unclear whether the sequence of events described above for the dynamical evolution of the liquid bridge (based primarily on experimental observations in Boger fluids and computed using constant-viscosity dumbbell models) is still valid for other viscoelastic fluids. Experimental determination of the extensional behavior is especially important for semi-dilute or concentrated polymer solutions. Such materials typically exhibit shear-thinning viscometric rheological properties and significantly less pronounced strain-hardening in extension (see for example Meissner [24]). It is expected that the absence of a dominant Newtonian solvent viscosity at short times, the broad spectrum of relaxation times and a low bound on the maximum extensional viscosity will all affect the dynamical evolution of the liquid bridge. For such materials, the need for direct comparison between experiments and numerical simulations is more pressing [25] since the kinematics in

the device never become spatially or temporally homogeneous [14,16] and it is this issue which we address in the present work. Experimental measurements by Sridhar and co-workers [3,26] have shown that in some concentrated polymer solutions which exhibit shear-thinning viscometric properties (e.g. the 'A1' and 'S1' fluids), a strain-hardening extensional stress growth function still exists and Trouton ratios in the range $100 - 1000$ are obtained. For such materials, the computations of Kolte et al. with the Papanastasiou-Scriven-Macosko (PSM) integral model show that the stress growth measured in a filament stretching device provides a very good agreement with the ideal extensional viscosity function expected in a homogeneous uniaxial elongation. For the values of the nonlinear parameters selected in [16] for the PSM constitutive model, Trouton ratios of $O(100)$ were obtained at moderate Hencky strains $\varepsilon \sim 4$ and the radial profile of the elongating fluid column becomes increasingly uniform with time, in agreement with computations and experiments for strain-hardening Boger fluids. However, in a more recent study, Hassager et al. [23] show that as the parameter controlling the level of strain-hardening in the fluid is varied and the ultimate steady-state extensional viscosity is gradually decreased then the filament can undergo a ductile failure in which the radius of the filament rapidly decreases to zero at the axial mid-plane.

The conditions necessary for rupture of polymeric fluids undergoing elongation have recently been discussed by Malkin & Petrie [27]. The ductile failure mode observed in [23] and in the present work is cohesive in nature (i.e. it occurs within the homogeneous bulk of the material and not at the solid-fluid interface) and may be characterized as an *unstable necking* of the filament mid-section. it is important to note that, as a result of the no-slip boundary conditions at the rigid end-plates of a filament stretching rheometer, a fluid sample that is initially cylindrical at $t = 0$ and subsequently elongated will develop a concave or 'necked' configuration for any imposed deformation history. Since the original design motivation for filament stretching devices was predicated on the observation that – at least for elastic fluids – the sample became increasingly cylindrical at high Hencky strains, it is thus useful to define a dimensionless measure that can be used to ascertain if the degree of necking in a fluid filament is increasing or decreasing. In the present work, we report this shape perturbation in terms of a relative difference of the computed free surface shape with respect to a reference state,

$$\delta R(z,\varepsilon) \equiv [R(z,\varepsilon) - R_{\rm ref}(z,\varepsilon)]/R_{\rm ref}(z,\varepsilon) \tag{1}$$

where $R_{\rm ref}(z,\varepsilon)$ represents a reference axial profile of the free surface at a specified strain ε. For experiments with highly elastic Boger fluids and computations with the Oldroyd-B model, we may select the ideal uniaxial elongational flow as the reference state and thus $R_{\rm ref} \equiv R_{\rm ideal} = R_0 \exp(-0.5\varepsilon)$. In this case, the variation of δR with increasing Hencky strain reflects the

discrepancy between the shape of the free surface obtained in the filament rheometer and the ideal homogeneous uniaxial elongation of a fluid cylinder. A similar definition was used in the numerical computations of Hassager et al. [23], and – for strongly strain-hardening fluids – the necking perturbation is observed both experimentally and numerically to decrease with increasing strain. A recent linear stability analysis of the non-autonomous one-dimensional slender body equations for an elongating filament of an Oldroyd-B fluid also shows that disturbances are expected to decay for $De > 0.5$ [28].

However, for experiments and calculations with a Newtonian or weakly-straining fluid, the choice of R_{ideal} as the reference state is inappropriate since the fluid filament is never close to the ideal cylindrical configuration, except at $t = 0$. For such fluids, we thus choose as a reference curve the profile obtained from the numerical simulation of a viscous Newtonian fluid with the same stretching history. In this case, δR describes the relative difference in free surface profiles between a viscoelastic fluid and a Newtonian fluid under the same flow conditions (i.e. with the same imposed end-plate boundary conditions and with all material parameters held fixed, except for the relaxation time which is set to zero). The necking perturbation δR is thus very small for low Hencky strains before nonlinear viscoelastic effects modify the filament profile. If the magnitude of the perturbation near the axial mid-plane (located at $z = 0$) of a viscoelastic fluid filament increases monotonically with time, we refer to the necking as 'viscoelastically destabilized' or 'unstable' with respect to the corresponding response of a Newtonian fluid; conversely, if the magnitude of the shape perturbation for the fluid elements near the mid-plane decreases with time we refer to the necking as 'stabilized' by fluid viscoelasticity.

We realize, of course, that the use of numerical simulations combined with this choice of necking criterion does not show unambiguously if there is, in fact, a finite time singularity in the governing equations corresponding to rupture of a viscoelastic fluid filament during exponential stretching. Such an analysis remains to be performed, possibly using the one-dimensional Lagrangian formulation of Renardy [29] which we have recently shown provides an accurate description of stress relaxation and necking breakup of viscoelastic fluid filaments following the *cessation* of elongation [30]. However, our definition does form a useful criterion for rheometry since this unstable necking phenomenon may be expected to severely compromise the ability of the filament stretching device to quantitatively measure the extensional viscosity of weakly strain-hardening fluids such as polymer melts and concentrated polymer solutions. To date, no experimental data for such materials has been available.

The primary goal of the present work may thus best be described as *computational rheometry*.

We combine experimental observations of the axial tensile force and filament profile evolution in a well-characterized concentrated polymer solution with time-dependent, two-dimensional finite element simulations using a nonlinear viscoelastic constitutive equation. By quantitatively comparing this information, we can investigate how closely the filament stretching device achieves the rheometric goal of providing a means for measuring the transient uniaxial viscosity of the test fluid in a hypothetical homogeneous uniaxial elongational deformation. Finally, having demonstrated both the feasibility of using the filament stretching device to measure the transient uniaxial extensional viscosity and the accuracy of the finite element simulations, we investigate the role of constitutive effects on the necking instability of a viscoelastic filament first documented by Hassager et al. [23]. Calculations with a FENE-P dumbbell model and with a Giesekus model that predict identical values of the *steady* elongational viscosity at a given Deborah number, but a different time evolution, demonstrate that it is the transient uniaxial stress growth in the filament that governs the dynamical evolution in the elongating and necking filament. These findings can be understood, at least qualitatively, in terms of a generalized Considère criterion [31]. This construction is commonly used in solid mechanics to understand necking in metallic and polymeric tensile test specimens [32].

Our experimental measurements are performed using a concentrated solution of 5.0 wt% polystyrene that has been extensively characterized in steady and transient shear flows by Li et al. [25]. The linear viscoelastic spectrum and the nonlinear rheological parameters for this fluid were determined by these authors and numerical calculations (using a multi-mode Giesekus model) of the stress field in the complex shearing and extensional flow near an axisymmetric stagnation point were shown to agree well with experimental measurements of the radially-averaged flow-induced birefringence. The majority of the time-dependent finite-element simulations in the present work are performed using a single-mode Giesekus model. Although a single relaxation mode does not represent a perfect fit of the viscometric properties of the test fluid, the predicted transient Trouton ratio agrees quantitatively well with experimental measurements except at small strains. Exploratory simulations with a multi-mode model show that this discrepancy can be resolved by accurately capturing the dynamical response of the shorter time-scales present in the fluid to the non-homogeneous deformation initially generated in the filament stretching device.

2. EXPERIMENTAL

2.1 Fluid Characterization

The test fluid used in the present work is a 5.0 wt% solution of high molecular weight, narrow distribution polystyrene obtained from Pressure Chemical, dissolved in a mixture of tricresyl phosphate (TCP) and dioctyl phthalate (DOP). The preparation and viscometric characterization of the fluid is described by Li and Burghardt [25]. Fig. 1 shows the steady-state shear viscosity and the first normal stress difference of the test fluid measured at a reference temperature of 22°C together with the predictions of the Giesekus model. As seen from Fig. 1, the experimental data can be well represented by a 3-mode Giesekus model using the parameter values given in Table 1. The 3-mode fit was obtained by Li & Burghardt by first fitting the small-amplitude oscillatory shear data ($G'(\omega)$, $G''(\omega)$) to obtain the linear viscoelastic parameters, η_i & λ_i, then by adjusting the values of α_i for each mode to describe the first normal stress difference and the nonlinear fluid response during start-up of steady shear flow. Detailed comparisons among the Phan-Thien-Tanner (PTT), modified PTT-White-Metzner and Giesekus models presented in [25] suggest that the 3-mode Giesekus model provides the best approximation for the measured transient and steady-state rheological data. We do not adjust the parameter values given in Table 1, but rather seek to evaluate how well they describe the transient uniaxial extensional viscosity of the 5.0 wt% polystyrene solution as measured in a filament stretching rheometer. In our single-mode finite element simulations, we retain the values of η_1 and λ_1 given in Table 1 and let $\lambda_2 \rightarrow 0$ and $\lambda_3 \rightarrow 0$ such that the total Newtonian solvent viscosity becomes $\eta_s = 0.069 + \eta_2 + \eta_3 = 9.15$ Pa.s. The solvent viscosity ratio for the single-mode model thus becomes $\beta = \eta_s/\eta_0 = 0.262$. This value limits the extent of the shear-thinning in the viscosity and leads to the plateau observed at high shear rates in Figure 1(a). Since the experimental measurements in the filament stretching device are typically performed at deformation rates in the range 0.1 - 10 s^{-1} this limitation of the single-mode model appears, at first glance, to be unimportant. However, the reciprocal duality between deformation rates and time-scales in viscoelastic fluids leads to errors in the modeling of the transient rheological properties of the material. In particular, the elimination of the shorter viscoelastic time scales and the introduction of a large, instantaneous viscous response may be expected to lead to an overly rapid growth of the predicted transient uniaxial stress in simulations of the filament stretching device.

2.2 Apparatus

The experiments were conducted using the filament stretching rheometer developed by Spiegelberg, Ables and McKinley [5]. A schematic diagram of the apparatus and discussion of the ex-

perimental subsystems are given elsewhere [5]. For the present experiments, the fluid sample is extruded through a positive-displacement syringe system onto rigid aluminum end-plates. The diameter of the circular end-plates used in this study was $d_0 = 0.7$cm. The initial separation between the two end-plates, L_0, is adjusted to ensure the sample configuration is initially cylindrical. The geometric parameters used in the tests are summarized in Table 2. During each filament stretching test, the lower plate is held stationary and is attached to a force transducer. A computer-controlled linear positioning system translates the upper end-plate so that the position and velocity of the end-plate both increase exponentially with time (i.e. eqn. (3) in ref. [14]). The measured tensile force $F_z(t)$, corrected for surface tension and gravitational body force contributions [5], and the filament radius, $R_{\mathrm{mid}}(t)$ are then used to compute the evolution of the tensile stress difference in the column with time. No velocity compensation algorithm of the type discussed in [3] & [5] is used in the present work.

Thermal environmental control was not incorporated into the rheometer. All measured results were shifted to a reference temperature of $22^{\circ}C$ by using the time-temperature superposition principle with the Arrhenius shift factor given by Li & Burghardt [25].

2.3 Operation Conditions

It is desired to perform rheological measurements in homogeneous flows characterized by a spatially uniform deformation rate. The key to a successful extensional rheological measurement is therefore to generate a simple, homogeneous elongational flow. The theoretical operating condition to be achieved in filament stretching devices is the ideal uniaxial elongational flow. The Eulerian velocity field in cylindrical coordinate system is well known (e.g. see eq. (26) in [14]), and the Lagrangian description of this flow field leads to an exponential separation between the two end-plates (i.e. eq. (3) in [14]).

In the ideal uniaxial elongational flow, the local axial strain rate $\partial u_z/\partial z$ is homogeneous everywhere in the liquid and identical to the imposed global extension rate, $\dot{E}$. However, the flow kinematics in filament stretching devices are spatially non-homogeneous, as has been shown both experimentally [2,5] and numerically [14-16]. As a result, the local effective strain rate will vary throughout the elongating liquid column and the Hencky strain accumulated by material elements in the filament will be non-homogeneous. For example, the Hencky strain based on the separation of the two end-plates, i.e.

$$\varepsilon_p \equiv \dot{E}t = \ln(L_p/L_0) \tag{2}$$

in general represents only the average of the local strain and strain rates experienced by all the fluid particles within the whole domain, as indicated by the first-order lubrication solution [5,14].

This 'reverse squeeze flow' results in a local strain rate at the axial mid-plane between the two end-plates, $z = L_p(t)/2$, which is 50% higher than the imposed global extension rate.

Since the local extensional strain rate at the mid-plane is extremely important for the experimental data analysis, the following *effective extension rate* is defined based on the free surface deformation at the mid-plane, $R_{\rm mid}$,

$$\dot{\varepsilon}_{\rm eff} \equiv -2d(\ln R_{\rm mid})/dt = -2U_{r,\rm mid}/R_{\rm mid} \tag{3}$$

where $U_{r,\rm mid}$ is the radial velocity component of the free surface at the mid-plane. The first equality in eq. (3) is widely used in experiments since $R_{\rm mid}$ can be obtained directly from the evolution of the free surface profile. The second equality is convenient for numerical analysis when the velocity-pressure formulation is used. An effective Hencky strain based on $\dot{\varepsilon}_{\rm eff}$ can be calculated directly from eq. (3) by the following integral,

$$\varepsilon_{\rm eff} = \int_0^t \dot{\varepsilon}_{\rm eff}(t')dt' \ = 2\ln[R_0/R_{\rm mid}(t)] \ . \tag{4}$$

If the deformation near the axial mid-plane is essentially uniform in the radial direction, then this effective Hencky strain represents the actual strain experienced by cylindrical fluid elements in the vicinity of the mid-plane.

2.4 Measurements of Extensional Viscosity

For the ideal homogeneous uniaxial elongational flow, the extensional viscosity can be expressed in non-dimensional form as a transient Trouton ratio, namely

$$Tr \equiv \bar{\eta}^+(\dot{E}, t)/\eta_0 = (\tau_{zz} - \tau_{rr})/(\eta_0 \dot{E}) \tag{5}$$

where τ_{zz}, τ_{rr} are the normal components of the extra stress tensor defined in the next section; η_0 is the total zero-shear viscosity. In the ideal uniaxial elongational flow of a Newtonian fluid, the Trouton ratio is simply a constant with value $Tr = 3$.

In filament stretching devices, the time-dependent quantities to be experimentally measured are the normal force on the end-plate, $F_z(t)$, and the mid-plane radius of the fluid filament, $R_{\rm mid}(t)$. From these experimental measurements, it is necessary to compute the extra stress difference and the extension rate in the fluid. Since these quantities vary spatially throughout the material, a number of different formulae for the 'apparent extensional viscosity' measured by the device are thus possible. Such problems have plagued the analysis of experimental data obtained from other devices proposed as extensional rheometers for polymer solutions (see for example Ref. [33]). For

filament stretching devices, numerical studies by Kolte et al. [16] and by Gaudet & McKinley [13] have considered a number of different possible formulae. Following the notation of Kolte et al. [16] we define two different quantities appropriate for an experiment in which a single exponential velocity profile is imposed. In a *Type I* experiment the axial deformation rate $\dot{E}$ and the average, or idealized, radius is used to compute the extensional viscosity function from the experimentally measured force,

$$\bar{\eta}^{+}_{(\mathrm{I})}(\dot{E},t) = \frac{F_z}{\dot{E}\pi R^2_{\mathrm{ideal}}} - \frac{\sigma}{\dot{E}R_{\mathrm{ideal}}} + O(F_i,F_g) \tag{6a}$$

where $R_{\mathrm{ideal}} = R_0\exp(-0.5\dot{E}t)$ is the ideal radial deformation in uniaxial elongational flow. In the above expression, the second term on the right hand side is the correction term arising from capillary effects, and σ is the surface tension coefficient. The final term $O(F_i,F_g)$ accounts for the corrections due to the inertia force F_i and gravitational force F_g, respectively. In the results presented in this paper, this last term is assumed to be negligibly small.

The use of R_{ideal} in eqn. (6a) implies that in the original type I analysis the filament is assumed to deform homogeneously as a cylinder throughout the test. This assumption is clearly a poor one, especially at early times (i.e. small strains), and modification is made in practice by making use of additional experimental knowledge of the evolution of the filament radius $R_{\mathrm{mid}}(t)$ at the axial mid-plane $z = L_p(t)/2$. There are several ways in which this additional information can be utilized. Firstly, the actual mid-point filament radius can be substituted in eqn. (6a) to provide a better estimate of the tensile stress in the filament. We refer to this as a modified type I or *type IB* analysis

$$\bar{\eta}^{+}_{(\mathrm{IB})}(\dot{E},t) = \frac{F_z}{\dot{E}\pi R^2_{\mathrm{mid}}} - \frac{\sigma}{\dot{E}R_{\mathrm{mid}}} + O(F_i,F_g) \tag{6b}$$

The experimental data presented in the present work are analyzed using this type IB formulation.

A further improvement for extensional viscosity calculations is to replace the constant axial extension rate, $\dot{E}$, in eq. (6b) by the time-dependent local effective extension rate, $\dot{\varepsilon}_{\mathrm{eff}}$, defined in eq. (3). This procedure leads to the *Type II* formula defined in ref. [16]

$$\bar{\eta}^{+}_{(\mathrm{II})}(\dot{E},t) = \frac{F_z}{\pi\dot{\varepsilon}_{\mathrm{eff}}R^2_{\mathrm{mid}}} - \frac{\sigma}{\dot{\varepsilon}_{\mathrm{eff}}R_{\mathrm{mid}}} + O(F_i,F_g)\,. \tag{7}$$

For clarity, the type II analysis is used exclusively in the present work for post-processing numerical solutions and for comparing with the type IB analysis. As will be seen later, it provides the best comparison to theoretical predictions of the ideal uniaxial extensional viscosity, $\bar{\eta}^{+}(\dot{E},t)$.

Note that the use of local variables in evaluating the kinematics in eq. (7) means that the computed Tr pertains specifically to the material elements near the mid-plane, even though the

stress difference is measured through the force transducer located at the rigid end-plate. Similar problems are faced in analysis of other extensional flow devices; however the benefit of the filament stretching device is that although the deformation in the filament is spatially non-homogeneous throughout the experiment, the tensile force transmitted axially along the column is constant at any instant in time for all $0 \leq z \leq L(t)$ (assuming inertial forces are negligibly small). By symmetry, shearing deformations are negligible at the axial mid-plane, except for very short times or small aspect ratios and eq. (7) thus should accurately capture the response of a material element to a homogeneous uniaxial elongational flow. Kolte et al. [16] found that although the Type I analysis of eq. (6) gave reasonable predictions (within $\pm 50\%$) for the stress growth in a strain-hardening viscoelastic liquid subjected to an ideal homogeneous uniaxial extensional flow, the type II analysis provided superior, almost quantitative results. In the present work we investigate the applicability of the type II analysis by comparing the experimental measurements using the weakly-strain-hardening concentrated polymer solution with two-dimensional time-dependent numerical simulations of the filament stretching device using the Giesekus model and with the theoretically expected Trouton ratio obtained in an homogeneous uniaxial elongation.

3. NUMERICAL

3.1 Mathematical Description of the Problem

We consider the extensional flow of a viscoelastic liquid contained between two parallel coaxial massless circular disks. The liquid column and the end-plates represent the basic elements comprising a filament stretching apparatus and are usually referred to collectively as a liquid bridge [12]. The typical arrangement is depicted schematically in Fig. 2.

The initial configuration of the liquid bridge is taken to be a cylinder when $t \leq 0^-$, as shown in Fig. 2(a). Let R_0 denote the radius of the two equal end-plates and L_0 the initial separation between the two end-plates. The initial aspect ratio of the liquid bridge is then defined as

$$\Lambda_0 \equiv L_0/R_0 \; . \tag{8}$$

At the instant $t = 0^+$, the top plate is set into vertical motion. The typical subsequent extensional deformation in the fluid filament is illustrated schematically in Fig. 2(b). The top plate will be referred to as the moving end-plate and its axial velocity is $\dot{L}_p = dL_p/dt$. The fluid column is assumed to remain axisymmetric and to wet the end-plates so that the contact line is pinned to the radial edges of the disks at all times. This assumption agrees with experimental observations of the filament profile near the end-plates, except at very high tensile stresses and large strains [18].

The aspect ratio of the filament, $\Lambda_t \equiv L_p(t)/R_0$, increases with time while the volume of the liquid bridge remains constant. At long times the filament will 'fail' or 'rupture', leading to the formation of two separate fluid domains. The location of this singular event depends on the kinematics of the deformation and the material properties of the liquid filament. We do not attempt to capture the local dynamics of the breakup process [21] but focus on the global evolution of the filament profile. The approximate axial location of the failure event can be readily detected from the simulations since the rate of radial thinning rapidly increases with time in this region.

In the absence of gravitational body forces, fluid inertia and the dynamical effects of an outer fluid viscosity, the elongating fluid filament will be symmetric about the axial mid-plane and will fail near the translating origin, $z = 0$, shown in Figure 2. In our experiments, the small size of the initial sample and the large viscous and elastic contributions to the total force ensure that gravitational body forces and inertia are negligible at all strains. In the numerical simulations, the gravitational body force term in the momentum equation is neglected while the inertia term is retained in the computations for numerical purposes. Sizaire and Legat [15] have examined the possible effects of fluid inertia at high strain rates and large axial strains, and Szabo [17] has considered the perturbative effects of weak gravitational forces (i.e. small Bond numbers) on the initial (non-cylindrical or 'sagging') profile of the filament and on the resulting force balance. A detailed study of the dynamical effects of gravity and fluid inertia on elongating liquid bridges will be given in a separate paper [34].

3.2 Governing Equations

To non-dimensionalize the governing equations, we select the radius of the end-plates, R_0, as a characteristic length, and use the imposed axial elongation rate $\dot{E}$ to construct both a time scale $(\dot{E})^{-1}$ and a viscous scale for the stress $\eta_0\dot{E}$. This leads to a set of dimensionless variables given by eq. (2) in ref. [30]. With this choice of scaling, the dimensionless time is equivalent to the axial or end-plate Hencky strain ε_p defined in eq. (2). This set of variables along with the dimensionless groups summarized in Table 2 is used in obtaining the non-dimensional governing equations and boundary conditions given below.

The fluid flow within the liquid bridge is assumed to be isothermal, incompressible, and axi-symmetric, and is governed by the conservation equations for mass and linear momentum

$$\nabla^* \cdot \mathbf{u}^* = 0 \,, \tag{9}$$

$$Re\left(\frac{\partial \mathbf{u}^*}{\partial t^*} + \mathbf{u}^* \cdot \nabla^* \mathbf{u}^*\right) = \nabla^* \cdot \mathbf{T}^* \,. \tag{10}$$

Here $\mathbf{u}^*$ is the velocity vector and $\mathbf{T}^*$ is the Cauchy stress tensor

$$\mathbf{T}^* \equiv -p^*\mathbf{I} + \boldsymbol{\tau}^* \tag{11}$$

where p^* is an isotropic pressure, $\mathbf{I}$ is the unit tensor and $\boldsymbol{\tau}^*$ is the total extra stress tensor.

The appropriate boundary conditions for this problem include: the no-slip condition along the interface between the liquid and the end-plates, axi-symmetry along the z-axis, the following prescribed motion at the moving end-plate

$$L_p^*(t^*) = \dot{L}_p^*(t^*) = \Lambda_0 e^{t^*} \tag{12}$$

and the kinematic and dynamic conditions on the deformable free surface boundary described by eqs. (7) & (8) in [30]. Finally, at time $t^* = 0^-$ the initial conditions for the velocity, pressure and extra stress fields are prescribed by eq. (9) in [30]. For convenience, we drop the asterisk notation in the remaining of the paper and do not explicitly identify variables as dimensionless.

3.3 Constitutive Equations

Successful simulation and prediction of rheologically complex material behavior depends on the accuracy of the constitutive equation which provides the tensorial relationship between the extra stress and the deformation history. In this work, we select the Giesekus model [35], a nonlinear differential constitutive equation based on the concept of deformation-dependent tensorial mobility. It can be derived from the Hookean dumbbell model [10,36] by allowing the Brownian motion and/or the hydrodynamic drag acting on the beads to be anisotropic. In a single-mode formulation of this model, the solvent contribution $\boldsymbol{\tau}_s$ and the polymeric contribution $\boldsymbol{\tau}_p$ to the extra stress are defined as

$$\boldsymbol{\tau} = \boldsymbol{\tau}_s + \boldsymbol{\tau}_p \ , \tag{13}$$

$$\boldsymbol{\tau}_s = 2\beta\mathbf{D} \ , \tag{14}$$

$$\boldsymbol{\tau}_p + De\boldsymbol{\tau}_{p,(1)} + \frac{\alpha De}{1-\beta}(\boldsymbol{\tau}_p \cdot \boldsymbol{\tau}_p) = 2(1-\beta)\mathbf{D} \ , \tag{15}$$

$$\boldsymbol{\tau}_{p,(1)} \equiv \frac{\partial \boldsymbol{\tau}_p}{\partial t} + \mathbf{u}\cdot\nabla\boldsymbol{\tau}_p - (\nabla\mathbf{u})^T\cdot\boldsymbol{\tau}_p - \boldsymbol{\tau}_p\cdot(\nabla\mathbf{u}) \tag{16}$$

where the viscosity ratio $\beta = \eta_s/\eta_0$ and $\mathbf{D}$ is the rate-of-strain tensor. The four physical parameters involved in this model are the solvent viscosity η_s, the polymer contribution to the viscosity η_p, the fluid relaxation time λ_1 and the dimensionless 'mobility factor', α associated with anisotropic effects. Equations (9)-(16) plus the boundary and initial conditions form a complete set of governing equations for this moving boundary problem.

For physically meaningful results with the Giesekus model, we require $0 \leq \alpha \leq 0.5$. In the limit $\alpha \rightarrow 0$ the model reduces to the quasi-linear Oldroyd-B model and, in addition to predicting a constant shear viscosity $\eta_0 = \eta_s + \eta_p$, the transient extensional viscosity function $\bar{\eta}^+$ grows without bound for Deborah numbers $De = \lambda_1 \dot{E} \geq 1/2$. As α is increased the extent of the shear-thinning in both the viscosity and the first normal stress difference increases while the value of the asymptotic or steady-state extensional viscosity decreases. For the values of α given in Table 1, the fluid is heavily shear-thinning (as can be seen in Figure 1) and very weakly strain-hardening.

In order to computationally explore the effects of constitutive non-linearities on the failure or rupture of the liquid column at long times, we have performed additional simulations with the finitely extensible nonlinear elastic (FENE-P) dumbbell model [37,38]. This is a simplified version of the FENE model with the pre-averaging approximation suggested by Peterlin. In this model the evolution of the non-linear dumbbell behavior over time is governed by the following partial differential equations:

$$\lambda_1 \mathbf{A}_{(1)} + \frac{\mathbf{A}}{1 - tr\mathbf{A}/L^2} = \mathbf{I} \tag{17}$$

and the polymeric contribution to the stress is given by the Kramers' expression

$$\boldsymbol{\tau}_p = \frac{\eta_p}{\lambda_1} \left[\frac{\mathbf{A}}{1 - tr\mathbf{A}/L^2} - \mathbf{I} \right] . \tag{18}$$

Here an additional material parameter is introduced, namely, the FENE extensibility parameter L which represents the ratio of the length of a fully-extended dumbbell to its equilibrium length.

The convected derivative in (17) is defined as

$$\mathbf{A}_{(1)} \equiv \frac{\partial \mathbf{A}}{\partial t} + \mathbf{u} \cdot \nabla \mathbf{A} - \left[(\nabla \mathbf{u})^T \cdot \mathbf{A} + \mathbf{A} \cdot \nabla \mathbf{u} \right] , \tag{19}$$

and the configuration tensor $\mathbf{A}$ represents a dimensionless ensemble average of the dyadic product, $\mathbf{QQ}$, of the dumbbell end-to-end vector $\mathbf{Q}$;

$$\mathbf{A} \equiv \langle \mathbf{QQ} \rangle / \langle Q^2 \rangle_{\mathrm{eq}} , \tag{20}$$

where $\langle \cdot \rangle$ denotes the ensemble average value in the phase space [37] and $\langle Q^2 \rangle_{\mathrm{eq}}$ is the equilibrium value of the mean squared end-to-end distance between the two beads when there is no fluid motion.

Both the Giesekus and FENE-P models predict shear-thinning in the viscometric functions, strain-hardening in the transient uniaxial extensional viscosity function $\bar{\eta}^+(\dot{E}, t)$, and a bounded steady-state uniaxial extensional viscosity $\bar{\eta}(\dot{E})$ at large Hencky strains. Asymptotic analysis of steady homogeneous uniaxial extension at Deborah numbers $De > 1/2$ for both models leads to

the following approximations (up to the order of $1/De$) for the steady-state uniaxial extensional viscosity [39]

$$\text{Giesekus}: \qquad \bar{\eta}/\eta_p \approx \frac{2}{\alpha}\left[1 - \frac{1-2\alpha}{2De}\right], \tag{21}$$

$$\text{FENE}-\text{P}: \qquad \bar{\eta}/\eta_p \approx 2L^2(1-1/2De) - 1/De\,. \tag{22}$$

Hence it is possible to select values of L^2 and α for the two different models which result in identical values of the steady extensional viscosity at a given value of De. For large De and strong strain-hardening, the leading-order terms in equations (21) and (22) indicate that we require approximately $\alpha \approx L^{-2}$, although the precise value varies weakly with De.

Finally, as we have shown in section 2, a single relaxation mode only provides an accurate fit to the viscometric material properties of the test liquid within a limited range of shear rates. To investigate the consequences of these limitations in a time-dependent simulation we also explore briefly a multi-mode simulation with the three-mode Giesekus model using the parameters given in Table 2. The total polymeric contribution to the extra stress $\boldsymbol{\tau}_p$ is obtained by adding the individual modal contributions.

3.4 Numerical Techniques

The finite element model used in this study assumes the solution is symmetric with respect to the mid-plane between the two end-plates. Consequently, the computational domain is defined by the region $0 \leq r \leq R(z,t)$ and $0 \leq z \leq L_p(t)/2$ shown in Figure 2, and we refer to this configuration as the 'half-length model'.

The governing equations are solved using the code POLYFLOW, a commercial finite element method (FEM) program primarily designed for the analysis of flow problems dominated by non-linear viscous phenomena and viscoelastic effects. The details of the FEM formulation and numerical techniques used in POLYFLOW are documented in [40]. Galerkin's method is adopted in the FEM discretization for the momentum equations, and the axi-symmetric FEM mesh is built with the 9-node quadratic quadrilateral element, in which velocity and extra stress are approximated by quadratic shape functions. The pressure is approximated as piecewise linear and discontinuous on inter-element boundaries (because the pressure 'nodes' do not coincide with the element nodes). The coordinates of the free surface boundary are interpolated by piecewise linear functions. The transient problem is solved by a predictor-corrector time integration scheme in which the backward Euler method is selected for the corrector. At each time step, the non-linear algebraic system resulting from the FEM discretization is solved by the Newton-Raphson iteration scheme. The

non-linear iteration termination is controlled by a specified iteration convergence tolerance of 10^{-5} for the relative error norms of residuals of the governing equations and free surface update.

Another important aspect for moving boundary problems is the remeshing technique which controls mesh deformation by relocating internal nodes according to the displacement of boundary nodes in order to avoid unacceptable element distortions. The Thompson transformation remeshing rule [41] is used in this work. Based on the solution of a partial differential equation of the elliptic type, the Thompson remeshing technique remains robust even for very large mesh deformations. Spatial and temporal convergence of the simulations has been verified separately. For the single-mode simulations presented in the present work, typical meshes contain 15300 degrees of freedom, and the total number of time steps required to achieve a strain of $\varepsilon_p \sim 5$ is about 800-1200 (depending on Deborah number). A typical computation takes approximately 15-20 hours CPU time on a Silicon Graphics four-processor IRIX Power Challenge (MIPS R8000) machine. Multiple-mode solutions require significantly more CPU time. The exploratory 3-mode calculation presented in section 4.6 took over 40 hours of CPU time on the same machine.

4. RESULTS AND DISCUSSIONS

In this section, we present experimental results and numerical analyses for the weakly strain-hardening fluid 5.0 wt% concentrated polystyrene solution described in section 2.1. The results are based on the conventional design of filament stretching devices in which the two circular end-plates have an equal and fixed diameter throughout the stretching process. As shown in section 2.1, the shear-thinning viscometric material properties of the test fluid can be very well represented by a 3-mode Giesekus model and the 1-mode fit provides a good approximation over a smaller range of shear rates. For simplicity, the numerical results for the shear-thinning fluid presented here will be based mainly on the single-mode Giesekus model, although a short discussion will be presented at the end of this section to show the potential improvement in accuracy of the numerically predicted extensional viscosity when a 3-mode Giesekus model is employed. In order to show the dramatic differences in the extensional rheological behavior between a weakly strain-hardening fluid and a strongly strain-hardening fluid, numerical results using the Oldroyd-B model and the FENE-P model will also be presented. In addition, a Newtonian fluid with the same solvent viscosity as that of the test liquid will serve as a reference for comparison purposes.

The basic geometric parameters and the material properties are listed in Tables 1 and 2. All calculations are performed in non-dimensional form, in which the dimensionless time is equivalent to the Hencky strain ε_p defined in eq. (2). In the variable step time integration, the maximum time-step is set to be $\Delta t = \Delta\varepsilon_p = 0.01$ for all Deborah numbers considered.

4.1 Free Surface Evolution

A direct qualitative characterization of extensional deformations of the liquid bridge in a filament stretching device is the evolution and shape change of the free surface. Due to the pinning condition at the rigid end-plates, the free surface of the liquid bridge cannot remain cylindrical and deforms greatly during the stretching history. For pronounced strain-hardening viscoelastic liquids, such as Boger fluids, previous experimental and numerical studies show that the 'necking' in the central part of the liquid bridge becomes slower than that in the corresponding Newtonian case once the Hencky strain surpasses a critical value. The pronounced strain hardening in the extensional viscosity leads to a progressively more uniform filament in the central part of the bridge. The Newtonian filament, by contrast, does not show any strain hardening, its radius is non-uniform at all times, and the filament becomes very thin at the mid-point between the two end-plates when the Hencky strain becomes large.

For the weakly strain-hardening fluid, a logical expectation is that the 'necking' rate of the liquid filament would be faster than the pronounced strain-hardening material but slower than the Newtonian fluid. However, a principal result of this work suggests that this is not true. In order to show this, we present in Fig. 3 a comparison of the free surface deformation history for three different fluids using the same small initial aspect ratio $\Lambda_0 = 0.54$ and an identical extension rate $\dot{E}$ in each case. The constitutive models considered represent a strongly strain-hardening viscoelastic liquid (simulated by the Oldroyd-B model), a weakly strain-hardening fluid (simulated by a 1-mode Giesekus model) and the corresponding Newtonian fluid. The simulation with the Oldroyd-B fluid model uses the same values of λ_1, η_p and β as chosen for the Giesekus simulation. Both models therefore predict an identical linear viscoelastic response at short times; however, the Oldroyd-B model predicts unbounded growth in the polymeric stress, whereas the Giesekus model predicts a small increase in the extensional viscosity and a finite steady-state plateau at large strains. The initial deformations of the two viscoelastic bridges shown in Fig. 3 are almost identical to that observed in the Newtonian liquid at small Hencky strains of $\varepsilon_p \sim 1$. Differences in the evolution of the free surfaces of the three liquids are seen for $\varepsilon_p \geq 2$. The profiles at $\varepsilon_p = 3.0$ and $\varepsilon_p = 3.4$ show that in the simulation with the Giesekus model the mid-point radius becomes even thinner than the Newtonian fluid. This observation suggests that the necking behavior of the weakly strain-hardening fluid column is thus faster than for the Newtonian fluid filament which shows no strain-hardening at all!

Free surface deformations of the shear-thinning viscoelastic liquid also differ dramatically from those of the pronounced strain-hardening liquid in the vicinity of the 'foot' area close to the

end-plates when the strain becomes large, as indicated by the profiles at $\varepsilon_p = 3.4$ in Fig. 3. To examine the differences, the foot area near the fixed end-plate is shown enlarged in Fig. 4. For the Oldroyd-B model, the axial curvature of the free surface changes dramatically at large strains and the fluid reservoir near the end-plates is depleted of more fluid than in the Giesekus model and the Newtonian fluid. For strongly strain-hardening materials such as Boger fluids, the experimental observations of Spiegelberg et al. [5] show that additional extensional deformation will further drain the fluid from these regions and initiate the onset of a non-axisymmetric elastic instability near the rigid end-plates, which results in the elongating fluid column partially decohering from the test fixtures. The results in Fig. 4 suggest that this type of elastic instability does not develop in the weakly strain-hardening liquid. It is interesting to note the difference in free surface shapes near the end-plates between the Giesekus model and the Newtonian fluid. For the Giesekus model, the diameter of the liquid filament near the end-plates is, in fact, larger than that of the Newtonian fluid. This suggests that the macromolecules in the weakly strain-hardening liquid experience an 'elastic recoil' near the end-plates at large strains. A more quantitative description of this recoil phenomenon is given below in Section 4.2. A comparison of filament shapes observed experimentally for three different fluids in the filament stretching device is shown in Fig. 5. Due to the fixed field of view of the CCD camera, the entire column profile cannot be imaged at large strains; however, comparison of Figs. $3-5$ suggests that the numerically simulated free surface evolutions agree qualitatively well with the experimental observations. In contrast to experiments with Boger fluids, filaments of the 5.0 wt% concentrated polystyrene solution fail (i.e. break) during the course of the experiment before stretching stops. Video-imaging shows that this failure occurs in the mid-region of the fluid column well away from the fluid reservoirs at each end-plate.

To further analyze the free surface evolution, we use the dimensionless shape perturbation $\delta R(z, \varepsilon)$ defined in eq. (1). As discussed in Section 1, for the Oldroyd-B fluid we select the ideal uniaxial elongational flow as the reference state. A typical example of temporal and spatial variations of δR is presented in Fig. 6. The shape perturbation δR is spatially non-uniform at strain $\varepsilon_p = 1.0$, but becomes increasingly homogeneous with increasing strain. The value of δR in the central part of the liquid column approaches a constant value $\delta R \approx -0.1$ at large strains in agreement with the computations of Hassager et al. [23].

For the Giesekus model, it is clear from Fig. 3 that the filament profile never approaches the ideal cylindrical configuration and we thus select the corresponding Newtonian profile as the reference curve. The resulting profiles of the shape defect δR at five strain levels are shown in Fig. 7. In this case, δR describes the relative difference in the necked filament profiles between

the weakly-strain-hardening Giesekus model and a constant viscosity Newtonian fluid under the same flow conditions. The initial deviations are small for low Hencky strains as shown by the curves at $\varepsilon_p = 0.01$, 1.0 and 2.0 in Fig. 7. The deviations in δR at $\varepsilon_p = 1.0$ and 2.0 are positive in the central part of the filament indicating that the decrease of $R(t)$ in the central part of the elongating viscoelastic liquid bridge is slightly slower than that of the Newtonian model at small strains, presumably due to the linear viscoelastic growth of the polymeric stresses. However, at larger strains $\varepsilon_p \geq 3.0$ the shape perturbations become large and negative in the central region of the filament, corresponding to a greatly accelerated necking in viscoelastic filaments characterized by the Giesekus model. For $\varepsilon_p \geq 3.0$, the value of δR is positive near the two end-plates as a result of the elastic recoil discussed above, and fluid is drawn into the end-plate regions even in the absence of a drainage mechanism such as gravity. As we show below, the rate of change in this discrepancy, i.e. $d(\delta R)/d\varepsilon$, also increases monotonically in time near the axial mid-plane indicating that the necking process is in fact destabilized by viscoelasticity and becomes increasingly severe at later times.

4.2 Flow Kinematics

The goal of the filament stretching device is to create a flow field in the fluid sample which approximates ideal uniaxial elongational flow kinematics. The accuracy of the measurements will thus depend on the spatial and temporal homogeneity of the kinematics generated in the device. Since direct experimental measurements of the flow field in a deforming fluid column with a curved free surface are usually difficult, numerical simulations can play an important role in analyzing the actual flow field generated in the liquid bridge.

For homogeneous uniaxial elongation of a cylinder, we expect the radius to decrease in the form

$$R_{\mathrm{ideal}}(t)/R_0 = \exp(-0.5\dot{E}t) \tag{23}$$

In reality, the flow kinematics generated in the liquid bridges are much more complicated and deviate significantly from the ideal irrotational flow field given by eq. (26) in [14]. In experimental studies, the kinematics in the deforming fluid filament are simply characterized by the radial displacement of the free surface at the mid-point between the two end-plates. Comparison of the temporal variations of $R_{\mathrm{mid}}(t)$ with the ideal evolution given by eq. (23) indicates how closely the actual flow kinematics approximate the ideal case.

In Fig. 8 we show the temporal evolution of the mid-plane radius, $R_{\mathrm{mid}}(t)$, for the three constitutive models at the same flow conditions used in Figs. 3 and 4. The variation of $R_{\mathrm{mid}}(t)$ provides a sensitive measure of the extensional flow kinematics in the liquid bridge and the

results indicate significant differences between the dilute polymer solution (Oldroyd-B model) and the concentrated polymer solution (Giesekus model). The former shows a pronounced strain-hardening manifested by a marked decrease in the slope of the $R_{\rm mid}(t)$ curve while the latter appears to exhibit a strain softening characterized by a continuous increase in the rate of change of the radial deformation. The results again suggest that the 'necking' in the shear-thinning liquid column proceeds much faster than a Newtonian fluid, which is consistent with the qualitative characterization based on the free surface evolutions shown in Fig. 3.

From observations of the radial free surface movement at the mid-plane, we can quantify the rate of deformation in the elongating liquid filament via the local extensional strain rate, $\dot{\varepsilon}_{\rm eff}$ defined in eq. (3). The effective extension rate represents the evolving extensional strain rate that the fluid elements experience in the vicinity of the mid-plane during the stretching. It can be shown analytically that for an incompressible fluid $\dot{\varepsilon}_{\rm eff}$ is equivalent to the radially-averaged value of D_{zz} at the mid-plane [42], namely

$$\bar{D}_{zz} \equiv \frac{1}{\pi R_{\rm mid}^2} \int_0^{2\pi} \int_0^{R_{\rm mid}} D_{zz}(r,0)\, r dr d\theta = \dot{\varepsilon}_{\rm eff} \ . \tag{24}$$

Therefore, $\dot{\varepsilon}_{\rm eff}$ provides the essential information required in the type II experimental analysis formulated in eq. (7). To demonstrate how the local extension rate varies with strain for the shear-thinning test fluid, a typical example is presented in Fig. 9 for a moderate Deborah number of $De = 1.68$. In this example, the characteristic extensional strain rate at the mid-plane is estimated in two ways using: 1) the effective extension rate $\dot{\varepsilon}_{\rm eff}$ based on the free surface movement, and 2) the pointwise value of D_{zz} evaluated at the central point $r = z = 0$. Our numerical computations verify that, even for the weakly strain-hardening fluid, $\dot{\varepsilon}_{\rm eff}$ can be used to accurately characterize the actual extensional strain rate that fluid elements experience at the mid-plane. The most pronounced difference between the values of $\dot{\varepsilon}_{\rm eff}$ and the 'pointwise' D_{zz} curves occur for $\varepsilon_p \leq 1.5$ indicating that at small strains the extensional strain rate is radially inhomogeneous on the mid-plane with lower values at the center. For small strains $0 < \varepsilon_p < 0.5$, the pointwise value of D_{zz} shown in Fig. 9 agrees well with the lubrication prediction, $\dot{\varepsilon}_{\rm eff} = 1.5\dot{E}$ [5]. At larger strains when $\varepsilon_p > 2$, both curves merge together suggesting that a radially homogeneous extensional strain rate is achieved and a 1-D slender filament description is increasingly appropriate.

In Fig. 10 we compare the evolution in the effective extensional strain rate as a function of strain. For the Oldroyd-B model, the strain hardening leads to a gradual decrease in the value of $\dot{\varepsilon}_{\rm eff}$ beyond $\varepsilon_p > 0.6$ and, at large strains, the effective extension rate approaches the imposed axial elongation rate. This result indicates that ideal uniaxial elongational flow kinematics can be

achieved at large strains and that the filament stretching device is especially suitable for polymeric liquids exhibiting pronounced strain-hardening. Following the initial linear viscoelastic response in the Giesekus fluid, the value of $\dot{\varepsilon}_{\text{eff}}$ increases rapidly and the filament evolution differs dramatically from the Newtonian or Oldroyd-B predictions. At a strain of $\varepsilon_p = 3.8$, the local extension rate for the shear-thinning fluid is about 5 times higher than the imposed axial extension rate.

If we evaluate the shape perturbation $\delta R(z, \varepsilon)$ at the filament mid-plane ($z = 0$) and denote this as δR_{mid}, then it is straightforward to show that

$$\frac{d\ \ln(1 + \delta R_{\text{mid}})}{d\varepsilon} = -\frac{1}{2}(\dot{\varepsilon}_{\text{eff}} - \dot{\varepsilon}_{\text{ref}}) \tag{25}$$

where $\dot{\varepsilon}_{\text{ref}}$ is defined in terms of the reference radius $R_{\text{ref}}(z = 0, \varepsilon)$ in the same manner as eq. (3). From the semi-logarithmic plot shoqn in Fig. 10(b) it is clear that the difference between the effective extension rate at the mid-point of the Giesekus filament and at the mid-point of the Newtonian filament is increasing almost *exponentially* with time (or strain). The difference in the radii δR_{mid} of the filaments at the mid-plane (corresponding to the 'necking' of the fluid column) thus increases very rapidly indeed. Additional numerical computations performed using the Giesekus model at the same Deborah number, but without surface tension (i.e. by setting $1/Ca = 0$), show that this enhanced necking does not arise due to capillarity, but rather is due solely to the viscoelasticity of the elongating fluid column. For any real fluid with a finite surface tension the enhanced rate of 'necking' will be enhanced even further, and capillary-driven filament breakup will occur much more rapidly. Furthermore, as a result of this rapid increase in the local extension rate, the Hencky strain experienced by fluid elements in the vicinity of the mid-plane becomes much higher than the average strain based on the axial separation of the two end-plates. For example, at an average strain $\varepsilon_p = 3.8$, the local strain at the mid-plane defined by eq. (4) may be as high as $\varepsilon_{\text{eff}} = 9.8$.

The effective extensional strain rate represents the local deformation rate around the mid-plane only. To investigate how the strain rate varies within the entire liquid column, we consider the rate of deformation tensor $\mathbf{D}$. Among its components, the axial velocity gradient D_{zz} is of most interest since it characterizes spatial variations in extension rate within the deforming fluid filament. For a homogeneous uniaxial elongational flow, $D_{zz} = \dot{E}$ everywhere; however, in reality, the flow in the filament stretching device is non-homogeneous and D_{zz} varies both spatially and temporally [14,16]. To demonstrate the significant difference in the deformation history experienced by a weakly-strain-hardening, shear-thinning viscoelastic fluid and by an ideal elastic fluid showing pronounced strain-hardening, we compare the variations of D_{zz} along the centerline at three typical

strains in Fig. 11. The D_{zz} curve at $\varepsilon_p = 0.2$ shown in Fig. 11 suggests that the simple lubrication squeeze-flow solution, valid at small initial aspect ratios for Newtonian fluids, also provides a good approximation of the flow kinematics for the Giesekus model at small strains. The D_{zz} profiles begin to differ when $\varepsilon_p > 1.0$ and the differences becomes quantitatively significant at large strains. For the Oldroyd-B fluid, the spatial profile at $\varepsilon_p = 3.0$ in Fig. 11 indicates that a uniform cylindrical column develops in a large central part of the liquid filament and the value of D_{zz} approaches $\dot{E}$ with increasing strain. By contrast, the deformation in the shear-thinning fluid filament never becomes uniform. The variations in D_{zz} for the Giesekus model at $\varepsilon_p = 3.0$ reveal two important features of the fluid kinematics in the filament stretching rheometer: firstly, the high extensional strain rate localization around the mid-plane and the development of the local necking instability; and secondly, the local recoil phenomenon near the end-plates. As we can see, at a strain of $\varepsilon_p = 3.0$, the value of D_{zz} for the Giesekus model becomes negative over 40% of the filament length, indicating that the fluid elements near the end-plates in fact undergo recoil (i.e. elastic unloading of the accumulated deformation) even though the filament as a whole is increasing in length. This local elastic recoil further accelerates the local extensional rate at the central part of the liquid column and leads to the 'necking' of the liquid filament at a rate that is much faster than that found in the corresponding Newtonian liquid filament.

4.3 Transient Extensional Viscosity

The primary function of the filament stretching rheometer is to measure the extensional viscosity, $\bar{\eta}^+$, as a function of Hencky strain and Deborah number. It is known from theoretical analysis that the extensional viscosity of the weakly strain-hardening fluid (simulated by the Giesekus model) differs significantly from that of the pronounced strain-hardening fluid (represented by the Oldroyd-B model). The Oldroyd-B model predicts an unbounded polymer stress growth, whereas in the Giesekus model the transient stress growth function approaches a steady-state at large strains. In this subsection, we compare measured values of the transient extensional viscosity for the weakly strain-hardening test fluid with numerical simulations of the filament stretching device and with theoretical predictions for homogeneous uniaxial elongation.

The operating conditions and geometric parameters for the three experimental tests considered in the present work are given in Table 2. The experimental test fluid is a concentrated solution of 5.0 wt% polystyrene and its material properties are summarized in Table 1. The experimental observables are the total normal force at the lower (fixed) end-plate, F_z, and the free surface profile $R(z,t)$ from which the mid-plane radius, $R_{\mathrm{mid}}(t)$, can be extracted. These experimental data are then used to calculate the transient extensional viscosity based on the type IB formulation

described in eq. (6b). In Figure 12(a), the transient extensional viscosity $\bar{\eta}^{+}_{(\mathrm{IB})}$ measured at an imposed extension rate of $\dot{E} = 2.32\ s^{-1}$ is plotted as a transient Trouton ratio, versus a non-dimensional time, or axial Hencky strain ε_p defined by eq. (2). Also presented in the same figures are the results of the single-mode numerical simulation post-processed using the same 'type IB' analysis. The simulations were performed both including surface tension (corresponding to a capillary number $Ca^{-1} = 0.106$) and without ($Ca^{-1} = 0$). Clearly the effects of surface tension are small and will become progressively less important at higher Deborah numbers as the tensile viscoelastic stresses in the fluid column become even larger. The agreement between experiments and simulations is excellent except for short times. The discrepancy between the measurements and the numerical results within this small strain range arises from the following two sources. Firstly, in the experiments, there is a finite ramping time (approximately 0.05 s for the present device) required for the motor to accelerate from rest to its initial velocity, whereas in numerical calculations it is assumed that the moving plate attains its initial velocity $V_0 = L_0\dot{E}$ instantaneously. Secondly, it is known from previous work [5] that errors in the measured force induced by additional shearing deformation near the rigid end-plates vary inversely with the initial aspect ratio, Λ_0. For the small aspect ratios used in the tests, the error is expected to be appreciable during the initial stage, especially in the single mode calculation due to the larger initial solvent viscosity. This second error source can be greatly reduced when the multiple relaxation mode model is used, as we show later.

As we have pointed out in Section 2, the extensional viscosity calculated in eq. (6) represents the extensional stress growth of the fluid elements in the vicinity of the mid-plane between the two end-plates. Consequently, an accurate estimate of the local extensional strain rate at the mid-plane is necessary. Apparently, the imposed axial extension rate $\dot{E}$ used in the type IB analysis is a poor approximation, since the computed curve and the experimental measurements do not agree well with the predicted response of the Giesekus model in homogeneous shear-free flow (shown in Fig 12(b) by the solid line). In particular, $\dot{E}$ underestimates the local extensional strain rate $\dot{\varepsilon}_{\mathrm{eff}}$ at the mid-plane, especially at large strains. As a result, the Trouton ratio presented in Fig. 12(a) does not approach a steady state; instead, it increases monotonically with strain (time). In interpreting experimental results for filament stretching devices, it should be noted that, in general, the type IB analysis provides an upper bound of the actual extensional viscosity since the actual deformation rate is always higher than the imposed axial deformation rate.

The results of numerical simulations can also be post-processed using the type II analysis given in eq. (7) and the predicted Trouton ratio, η^{+}_{II}, is plotted in Fig. 12(b) as a function of the effective

strain ε_{eff} accumulated at the mid-plane. As we can see, the local strain ε_{eff} is much higher than the average axial strain ε_p. The use of $\dot{\varepsilon}_{\text{eff}}$ in the type II analysis provides a far superior approximation of the local extensional strain rate at the mid-plane. As a result, the numerical prediction shown in Fig. 12(b) approaches a steady-state value that agrees well with the theoretical value expected for $\alpha = 0.32$. The 'Constant Stretch Rate' curve shown by the solid line in Fig. 12(b) is the theoretical prediction of the 1-mode Giesekus model for ideal uniaxial elongational flow at a constant Deborah number $De \equiv \lambda_1 \dot{E}$. Of course, the extension rate experienced in the actual experiment by the fluid element at the mid-plane is temporally inhomogeneous. The 'Variable Stretch Rate' curve (broken line) in Fig. 12(b) shows the predicted transient extensional viscosity of the Giesekus model obtained by numerically integrating the ordinary differential equations for the axial and radial stress components in ideal elongational deformation with a time-varying extension rate given by $\lambda_1 \dot{\varepsilon}_{\text{eff}}(t)$. It can be seen that the difference between these two curves is, in fact, extremely small since the extensional viscosity predicted by the Giesekus model (and also many other constitutive models) is primarily a function of the strain and is only a very weak function of $\lambda_1 \dot{\varepsilon}_{\text{eff}}$, provided that $\lambda_1 \dot{\varepsilon}_{\text{eff}}(t) \gg 0.5$.

Similar results are shown in Figures 13 and 14 at stretch rates of $\dot{E} = 3.42\ s^{-1}$ and $\dot{E} = 4.68\ s^{-1}$ respectively. In each figure the experimental measurements are again analyzed using the type IB analysis and are shown as solid circles, whilst the corresponding simulation values are shown as hollow squares. The same numerically-computed values of force and radius are also used in conjunction with eq. (7) to compute the transient Trouton ratio using the type II analysis and are shown as solid diamonds. For clarity, we have chosen not to re-plot the experimental data using the type II analysis on the same figure; however, it is clear from the good agreement between the type IB experimental and numerical curves that the resulting data values will follow the theoretical curve as closely as the numerical computations. In comparing figures $12-14$ it should be noted that for data points computed using the type IB analysis the relevant strain measure for the abscissa is the total axial strain $\dot{E}t$, whereas for the data computed using the type II analysis the appropriate measure is the effective strain ε_{eff} experienced by fluid elements near the mid-plane which can be computed using eq. (4).

The predicted results from the simulations are truncated when numerical convergence is lost, as indicated by the growth of small-amplitude spatial oscillations in the free surface profile. Attempts to axially refine the mesh can extend the maximum critical strain slightly, however the elements near the column midpoint always develop extremely high aspect ratios and large tensile stresses as the filament necking develops. The dynamical evolution of the column at larger strains is better

suited to a one-dimensional slender filament theory (see e.g. [28-30]). Furthermore, since the local extension rate $\dot{\varepsilon}_{\text{eff}}(t)$ rapidly increases near breakup, viscoelastic contributions to the total tensile stress in the filament will also arise from the additional 'fast' relaxation modes. This will also retard the ultimate breakup dynamics since the dimensionless stretching rate for these modes $\lambda_i D_{zz}(z,t)(\text{where}\, i = 2, 3...)$ only exceeds the critical value of 0.5 in the middle 'necked' region of the column.

The results shown in Figs. $12-14$ indicate that the accurate measurement of R_{mid} and the use of $\dot{\varepsilon}_{\text{eff}}$ in the calculation of Tr are extremely important in quantitative computation of the transient Trouton ratio for weakly strain-hardening fluids such as concentrated polymer solutions. The comparisons presented in this subsection also serve as a validation of the choice of constitutive equation for this polymer solution. As we have shown, numerical simulations based on the 1-mode Giesekus model provide reasonable kinematic and dynamic predictions which agree both qualitatively and quantitatively with experimental observations for the test fluid. With this in mind, we now proceed to investigate numerically some important issues involved in the experimental design and modeling of filament stretching devices which are difficult to explore experimentally.

4.4 Effects of the Initial Aspect Ratio

In the design of the filament stretching rheometer, the initial aspect ratio Λ_0, defined in eq. (8), is an important geometric parameter that deserves special attention. During experiments the rigid end-plates and the no-slip constraint at the solid-liquid interface result in a significantly non-homogeneous flow at short times. This flow inhomogeneity and pre-shear history will, in turn, affect the dynamic behavior of the viscoelastic liquid filament at large strains. For a Boger fluid with a constant shear viscosity and pronounced strain hardening, a previous experimental study [5] and numerical analysis [14] have both shown that the initial non-homogeneous flow and the induced shear stress depend strongly on the initial aspect ratio of the liquid column. No studies on the effect of the initial aspect ratio have been reported to date for a weakly strain-hardening fluid with appreciable shear-thinning in the viscometric functions.

To investigate the effects of Λ_0 for the present test fluid, a series of simulations are conducted at identical imposed axial extension rates, with the initial aspect ratio as the variable parameter. The three characteristic values of the aspect ratio considered are $\Lambda_0 = 0.54$ (to match the experiments in Section 4.3) and $\Lambda_0 = 1.0$ and 2.0. The Deborah number is the same for all the three cases, $De \approx 2.0$. Such tests are difficult to perform experimentally in concentrated polymer solutions since the maximum axial length of the initial liquid bridge is constrained by gravitational sagging and the corresponding Plateau stability criterion [17,21]. Conversely, shrinking the end-plate radius

reduces the total tensile force exerted by the elongating thread below the minimum transducer sensitivity.

We first examine the effect of Λ_0 on the radial flow kinematics by analyzing the profiles of the non-dimensional mid-plane radius, $R_{\rm mid}/R_0$, as a function of the Hencky strain ε_p, as shown in Fig. 15. It can be seen that the evolution of the filament is greatly affected by the initial aspect ratio and the necking at the mid-plane in general decreases with increasing Λ_0. For small initial aspect ratios $\Lambda_0 \leq 1.0$, the necking in the middle of the test fluid filament is accelerated with respect to the Newtonian fluid. The smaller the value of Λ_0, the faster the rate of necking develops or, equivalently, the more unstable the homogeneous uniaxial elongation of an initially cylindrical viscoelastic liquid column is. Increasing the value of Λ_0 helps improve the stability of the liquid column, and for $\Lambda_0 = 2.0$, the evolution of $R_{\rm mid}(t)$ is more characteristic of the deformation observed in an Oldroyd-like fluid as might naively be expected for a weakly strain-hardening fluid in a uniaxial elongational flow.

A quantitative comparison of the local extensional strain rate, $\dot{\varepsilon}_{\rm eff}$, at the mid-plane is shown in Fig. 16. In the early stages of deformation there is a similar linear viscoelastic response in all three geometries, with the characteristic value of $\dot{\varepsilon}_{\rm eff}$ set by the aspect ratio. As expected, the simulation with the smallest value of initial aspect ratio results in an extension rate to the value $\dot{\varepsilon}_{\rm eff} \approx 1.5\dot{E}$ predicted by lubrication theory. The local extensional strain rate starts to increase for $\varepsilon_p > 1.0$ with the rate of increase in $\dot{\varepsilon}_{\rm eff}$ varying inversely with the initial aspect ratio. Finally for $\varepsilon_p > 3.5$ we observe a second stage of strain-hardening for the $\Lambda_0 = 2.0$ case.

This evolution in flow kinematics at the mid-plane has a direct impact on the stress profile developed in the elongating liquid column as a result of the non-uniform deformation history and the initial non-homogeneous shear flow. To demonstrate this fact we present in Figure 17 the radial variations in the axial component of the polymeric stress, $\tau_{p,zz}$, at the filament mid-plane. At a small strain $\varepsilon_p = 0.2$ the radial stress profile is strongly affected by the initial aspect ratio. The non-homogeneity in stress develops mainly near the free surface as a consequence of the non-cylindrical free surface deformation. For small initial aspect ratios $\Lambda_0 \leq 1$, a stress boundary layer develops directly adjacent to the free surface. The results show that lower values of Λ_0 lead to steeper stress boundary layers and the spatial non-homogeneity in stress can be alleviated by increasing the initial aspect ratio, as shown by the $\Lambda_0 = 2$ case in Fig. 17(a). The numerical solutions further indicate that the radial gradients in stress arising from the non-homogeneous deformation history at short times decay with increasing strain. At a strain of $\varepsilon_p = 3.8$, the radial profile of $\tau_{p,zz}$ becomes uniform for all three initial aspect ratios as can be seen in Fig. 17(b), although the

magnitude of the polymeric stress is still significantly affected and varies inversely with the aspect ratio. Furthermore, it should be noted that axial variations of $\tau_{p,zz}$ within the fluid column persist throughout the entire stretching history.

The effect of initial aspect ratio on the extensional viscosity computed from measurements of the end-plate force and the mid-point radius is shown in Fig. 18. Here the calculation of extensional viscosity is based on the more accurate type II analysis. For the smallest aspect ratio, $\Lambda_0 = 0.54$, there is a significant discrepancy between the numerical prediction and one-dimensional theory at small strains. This error arises from the lubrication-like shear flow induced by the initial geometry of the device and can be effectively eliminated by increasing Λ_0. Of the three values of Λ_0 shown in Fig. 18, the $\Lambda_0 = 2.0$ case provides the best comparison to the ideal transient Trouton ratio expected theoretically, with less than 10% error throughout the imposed deformation history. However, even an increase in the aspect ratio to $\Lambda_0 = 1.0$ provides improved accuracy at shorter times, and also allows larger Hencky strains to be achieved before the filament begins to undergo a necking failure. Despite the variations in both the effective deformation rate (Fig. 16) and the tensile stress in the column (Fig. 17), it is clear from Fig. 18 that the transient uniaxial elongation viscosity of the fluid can be measured for all of the aspect ratios we have considered numerically.

4.5 Effects of the Mobility Factor α

The Giesekus constitutive equation contains a single nonlinear term, weighted by the dimensionless mobility factor α, which is associated with anisotropic Brownian motion and/or anisotropic hydrodynamic drag on the constituent polymer molecules [36,37]. This nonlinear term controls both the magnitude of shear-thinning in the viscometric functions and the extent of strain-hardening in uniaxial elongation. The physically realistic range of the mobility factor is $0 \leq \alpha \leq 0.5$. In the limit $\alpha \to 0$, the Oldroyd-B model is recovered, which predicts a constant shear viscosity and unbounded stress growth in elongation. For the test fluid considered in this work, the best fit of the viscometric data to a single-mode Giesekus model yields $\alpha = 0.3162$ [25] corresponding to pronounced shear-thinning and a very weakly strain-hardening extensional viscosity. By decreasing the value of α, the extent of shear-thinning can be reduced and, at the same time, the magnitude of the tensile stress growth can be increased.

To examine the effects of the mobility factor on the predicted kinematic and dynamic response of the elongating liquid column in a filament stretching device, we present the results of three simulations with the mobility factor as the variable parameter. The same moderate Deborah number $De = 1.97$ and small initial aspect ratio $\Lambda_0 = 0.54$ are used in all three simulations to match the experiments discussed in Section 4.3. The values of α for the three simulations are

$\alpha = 0.32$ (corresponding to the heavily shear-thinning and weakly strain-hardening test fluid used in the experiment), plus $\alpha = 0.032$ and 0.0032, respectively. A comparison of the two geometric and kinematic measures entering in the definition of the extensional viscosity are presented in Figure 19. The variation in the temporal history of the mid-plane radius, $R_{\rm mid}$, with α is shown in Fig. 19(a), and the local effective extensional strain rate, $\dot{\varepsilon}_{\rm eff}$ is shown in Fig. 19(b). The effect of the nonlinear mobility factor is not observable within the small strain range $\varepsilon \leq 0.6$ when the fluid exhibits a purely linear viscoelastic response and all three simulations predict almost identical kinematics at the mid-plane. At larger strains, the three profiles deviate significantly and the results show that materials with less shear-thinning and greater strain-hardening exhibit reduced rates of 'necking' and the stability of the liquid column is correspondingly enhanced. As we show below in Section 5, the stability is in fact most influenced by the *rate* of increase in the tensile stress with increasing Hencky strain. A comparison of Fig. 19 with Figs. 8 and 10 indicates that the filament evolution for $\alpha = 0.0032$ is very similar to the Oldroyd-B fluid response with pronounced strain-hardening manifested by a distinct decrease in the rate of necking curve and a corresponding decrease in $\dot{\varepsilon}_{\rm eff}$.

Fig. 20 shows the effect of the mobility factor on the predicted surface shape in the vicinity of the 'foot' near the end-plates. The $\alpha = 0.32$ case represents the typical, weakly strain-hardening viscoelastic behavior in which the ultimate filament stability is controlled by the ductile necking failure in the middle of the filament. The $\alpha = 0.0032$ case is very close to the typical behavior of an Oldroyd-B fluid in which the maximum extent of stretching is controlled by the onset of an elastic instability that develops near the end-plates and leads to the decoherence of the liquid column. In this regard, the $\alpha = 0.32$ and $\alpha = 0.0032$ simulations represent two extreme cases in which the stretching capability of a filament stretching device is controlled by two entirely distinct instability mechanisms. The most interesting case is perhaps the intermediate $\alpha = 0.032$ case which exhibits more moderate shear-thinning and strain-hardening. From a numerical point of view, this case is relatively easier for the remeshing scheme and for convergence of the nonlinear iteration. As we can see from Fig. 19, for a given finite element mesh, this case has the highest numerically accessible Hencky strain, $\varepsilon_p \approx 4.4$. In contrast, the $\alpha = 0.0032$ case is the most difficult one to resolve and the numerical solution fails to converge at $\varepsilon_p \approx 3.6$. The lack of convergence arises because the curvature of the free surface changes dramatically with axial position at large strains and the reservoir near the fixed end-plate is rapidly depleted of more liquid leading to very large local distortions in the finite elements.

Despite this huge variation in the dynamical evolution of the filament profile, the simulations

suggest that in each case a filament stretching rheometer can be used to accurately measure the tensile stress growth in the test fluids. In Fig. 21 we present the transient Trouton ratio computed using the type II analysis for the three numerical simulations (indicated by symbols) and compare them to the corresponding theoretical predictions for start-up of ideal uniaxial elongational flow at constant extension rate (the three curves). It is readily apparent that the value of the steady-state extensional viscosity plateau, and also the rate of stress growth at moderate strains ($1 \leq \varepsilon \leq 3$), both increase as α decreases; however, in each case the computed Trouton ratio agrees well with theory. The strain measure used in Fig. 21 is the effective Hencky strain relevant to the mid-plane (eq. 4) and large strains are attained as α is increased due to the enhanced rate of necking near the filament midplane.

The numerical calculations presented in Figs. 19-21 suggest that the filament stretching device is a versatile rheometric tool that can be used for characterizing a wide spectrum of viscoelastic fluids ranging from dilute solutions with constant shear viscosity and strong strain-hardening characteristics to concentrated solutions and low viscosity melts with heavily shear-thinning viscometric functions and little strain-hardening.

4.6 An Exploratory Multi-Mode Calculation

The numerical results presented throughout this paper are based on a single-mode Giesekus model, and it is clear from Figs. 12-14 that we are able to accurately capture the stress growth observed experimentally, except at very small strains. Furthermore, from examination of Figs. 19-21 it can be seen that this deviation is not connected with the nonlinear properties of the fluid and, in fact, the short time response is governed by the linear viscoelastic response of the material. In a single mode calculation, the short-time responses of the fluid are deliberately not resolved and the contributions of these modes to the total shear viscosity are collapsed into the instantaneous 'solvent' response. This artificially-elevated viscous contribution to the stress masks the true material response by amplifying the effect of the initial radial 'squeeze flow' on the net force exerted on the end-plate.

To quantify this effect, a numerical test was also conducted using the 3-mode Giesekus parameters given in Table 1 at a stretch rate of $\dot{E} = 4.48\ s^{-1}$ corresponding to a Deborah number (based on the longest relaxation time λ_1) of $De = 1.89$. We first calculate the extensional viscosity based on the type IB analysis and compare the results of the two numerical simulations with experiment in Fig. 22(a). Then we also post-process the numerical solution using the type II analysis and compare the resulting data with one-dimensional theory in Fig. 22(b). Note that here the curve denoted 'theory' is based on the 3-mode Giesekus model with a constant

dimensionless rate of stretching ($\lambda_i \dot{E}$) for each mode. As we can see, the multi-mode calculation provides a much better prediction for the initial stress growth of the material within the small strain range $\varepsilon_p \leq 0.6$, and compares very favorably to both experimental measurement and theoretical prediction. However, the difference in the predicted Trouton ratio between the 3-mode and the 1-mode simulations becomes small when $\varepsilon_p > 0.5$. This exploratory calculation suggests that single-mode calculations can provide adequate accuracy at far lower computational cost for most of the Hencky strains examined in the present work. A more detailed study of the multi-mode simulations and comparisons between multi-mode and single-mode solutions are discussed elsewhere [30].

5. NECKING IN ELONGATING VISCOELASTIC FILAMENTS

The experiments and calculations presented above have shown that filament stretching devices can be used to measure the transient Trouton ratio in weakly strain-hardening materials, even though the evolution of the filament is markedly different to that observed in either Newtonian liquids or strongly strain-hardening dilute polymer solutions. Most importantly, numerical simulations show that the fluid reservoirs near the rigid end-plates undergo an elastic recoil or unloading (i.e. the local elongation rate is $D_{zz} = \partial u_z / \partial z < 0$) and the local deformation rate $\dot{\varepsilon}_{\text{eff}}$ at the filament mid-plane rapidly increases as the radius decreases towards zero. Following Malkin & Petrie [27] we refer to this as a *ductile necking failure* driven by the viscoelasticity of the fluid. This failure mechanism is distinct from those of either capillary-driven breakup (e.g. in a Newtonian thread) or cohesive fracture, although all these mechanisms lead to what may generically be defined as rupture of the filament into two topologically distinct fluid domains.

In contrast to related considerations of 'intrinsic spinnability' in fiber spin lines [43] the tensile force in the elongating filament varies with time, although it is constant along the axis of the fluid column at any instant in time (provided fluid inertia is negligible). Furthermore, the material element at the axial mid-plane of the column experiences the entire Lagrangian history of the deformation in contrast to the finite residence time of material elements and the Eulerian steadiness of the spin-line. However, despite these differences, the present problem shares much in common with analyses of 'spinnability', in particular the constitutive rheology of the elongating filament plays a key role in determining whether the maximum Hencky strain that may be imposed on the material is limited by the onset of a ductile failure near the filament mid-plane [23] or by an elastic end-plate instability [5,19].

The physical mechanisms leading to the unstable necking observed in our simulations with the Giesekus model can be simply understood in terms of the Considère criterion commonly employed in solid mechanics to understand necking in ductile metals and polymers [44]. In its simplest form,

the criterion states that the homogeneous elongation of a uniform elastic cylinder is unstable and a 'neck' will form if the net tensile force in the column passes through a maximum at a critical strain ε_c. Even if a material is strain-hardening, the increase in the true (or Cauchy) stress with Hencky strain may be insufficient to offset the decrease in the cross-sectional area, and the tensile force (or 'engineering stress') can pass through a maximum. As an example, for a hypothetical material with radius decreasing at the rate given in eq. (23) and a tensile stress difference given by $\Delta\tau = E\varepsilon$ (where E is the Young's modulus and $\Delta\tau$ is defined as the tensile stress difference in the column), continued elongation as a uniform cylinder is unstable beyond a critical strain $\varepsilon_c = 1$. The Considère criterion is essentially a quasi-static or 'energy' stability criterion which can be derived from the principle of virtual work [45]. Physically, beyond the critical strain, the sample may lower its total elastically-stored energy by contracting or 'necking' in a single localized region and elastically-unloading elsewhere. Energy arguments have proven useful in other aspects of viscoelastic flow stability [46] and the close connections between viscoelastic constitutive equations for polymeric fluids and viscoplastic equations for metals has been noted by Rubin and Yarin [47].

For a viscoelastic liquid column being elongated in a filament stretching device, the situation is more complex than the simple example given above, since the initial profile of the filament is never cylindrical and furthermore the work done in elongating the filament is partially stored elastically and partially dissipated viscously. Nonetheless, Hassager et al. [23] have shown that for the K-BKZ model in the limit $De \to \infty$ (such that viscous dissipation is negligible) the Considère criterion can quantitatively predict the onset of a rapid and catastrophic necking in the filament profile near the mid-plane. The onset of unstable necking observed in the present simulations is more gradual than observed in [23] since the Deborah number is much lower ($De \approx 2.0$ rather than $De = 100$) and there is a large solvent viscosity. Surprisingly, the Considère criterion can still be used to rationalize the evolution of the filament profile with strain; however, a quasi-static energy analysis cannot provide information about the *rate* of evolution of the unstable necked region.

To incorporate such effects requires either a theoretical linear stability analysis or direct numerical simulation of the full equations of motion. Ide & White [48] and Olagunju [28] have considered the former approach for the UCM and Oldroyd-B models for the case of a uniform cylindrical column and for a one-dimensional slender-body approximation to the governing equations. However, in the absence of analytical expressions for the filament radius profile $R(z,t)$ and the corresponding polymeric stress tensor for more complex non-linear constitutive models, we have instead pursued the latter approach.

We consider the transient evolution of an initially-cylindrical sample at a Deborah number $De = \lambda_1 \dot{E} = 2.0$ in which the fluid rheology is characterized by either the Oldroyd-B, Giesekus or FENE-P model. For the Oldroyd-B model at Deborah numbers $De > 1/2$ and Hencky strains $\varepsilon \geq 2$, the polymeric contribution to the tensile stress difference in the elongating column is given approximately by the expression

$$\Delta\tau_p \approx \frac{2\eta_p}{\lambda_1(2-1/De)}\left[e^{(2-1/De)\varepsilon} - \frac{3}{2(De+1)}\right] . \tag{26}$$

Since the cross-sectional area is decreasing exponentially with Hencky strain, the tensile force in the column passes through a maximum for $De < 1$, but grows without bound at larger De. For the solvent contribution to the total viscosity we retain the value $\beta = 0.262$ and for the nonlinear constitutive equations select $\alpha = 0.1$ and $L^2 \approx 11.0$ so that the two models predict identical steady-state extensional viscosities $\bar{\eta}(\dot{E})/\eta_0 \approx 12.6$ at $De = 2.0$. The relative propensity of these constitutive models to undergo ductile failure may then be understood by comparing how the transient uniaxial stress growth during extension (i.e. the transient Trouton ratio) compares to that given by eq. (26) for the Oldroyd-B model.

In Figure 23 we show the predicted evolution in the mid-plane radius with strain for each model. Each simulation is truncated when numerical convergence is lost. At small strains, all profiles follow the expected Newtonian lubrication profile with an effective strain rate 50% larger than the imposed elongation rate. However, at larger strains the response of each constitutive model leads to a uniquely different profile in the mid-point radius. As previously documented in Fig. 10, the deformation rate in the Newtonian filament slowly increases as the sample undergoes capillary necking, whereas the deformation rate in the strongly hardening Oldroyd-B fluid decreases and approaches the imposed ideal value. For the two fluids with bounded elongational viscosities, the rate of necking is initially slowed by the strain-hardening in the transient elongational viscosity and the curves of $R_{\mathrm{mid}}(t)$ deviate above the Newtonian simulation and the lubrication solution. However, as the extensional viscosity saturates, the profiles of $R_{\mathrm{mid}}(t)$ show a downward turn and the effective extension rate begins to climb as the rate of necking in the column increases. For the Giesekus model this necking is very rapid due to the elastic recoil in the fluid near both end-plates shown in Fig. 11(c) and the mid-point radius becomes narrower than the Newtonian filament for strains $\varepsilon_p \geq 3.5$. For the FENE-P filament the rate of necking is much slower (for reasons explained below); however, it is clear that the filament has begun to fail, and both the effective extension rate computed from the slope of the $R_{\mathrm{mid}}(t)$ curve according to eq. (3) and the mid-point shape perturbation δR_{mid} increases monotonically beyond $\varepsilon_p \geq 1.5$.

Since the transient Trouton ratio is directly related to the axial force in the filament, the Considère stability constraint for stable elongation of the filament with increasing end-plate Hencky strain may be written as:

$$\frac{dF_z}{d\varepsilon_p} = \frac{d}{d\varepsilon_p}(Tr \cdot \eta_0 \dot{E} \cdot R_0^2 e^{-\varepsilon_p}) > 0 \tag{27}$$

or by differentiating and re-arranging, for stable necking we require

$$\frac{dTr}{d\varepsilon_p} > Tr\ . \tag{28}$$

The left-hand and right-hand sides of eq. (28) are plotted for both the Giesekus and FENE-P model in Fig. 24(a) and (b) respectively. At short times the Trouton ratio grows rapidly with strain for both materials and the necking is 'stable' in the sense that the column evolves in similar manner to the Newtonian filament. However, beyond a critical strain $\varepsilon_c \approx 1.4$, the transient Trouton ratio for the Giesekus fluid deviates below the Oldroyd-B curve and approaches a steady state. The criterion (28) is thus violated and the column begins to rapidly neck down in the middle whilst elastically unloading near either end-plate. In this case viscoelasticity destabilizes the evolution of the necked filament. By contrast, for the FENE-P material - which strain-hardens even more rapidly than the exponential dependence of the Oldroyd-B model - the necking is initially stabilized by the fluid viscoelasticity and the effective stretch rate in the middle of the filament begins to decrease with strain. However, eventually the extensional viscosity in the thread begins to saturate, $d(Tr)/d\varepsilon_{\rm p}$ decreases, and the rate of necking begins to increase monotonically. The thinning and eventual break-up of a FENE-P fluid thread in a 'micro-filament rheometer' (in which there is no imposed exponential stretching) has also been discussed recently by Entov & Hinch [49].

Despite the very different time evolutions in the filament mid-plane radius (and the associated variations in the time histories of the force $F_z(t)$ and $\dot{\varepsilon}_{\rm eff}(t)$) predicted by the FENE-P and Giesekus simulations, the filament stretching device is still able to accurately monitor the evolution in the transient extensional viscosity for each class of fluid. In Fig. 25 we show the predicted transient Trouton ratios (computed using the type II force balance given in eq. (7)) for each simulation together with the equivalent theoretical curves expected in a homogeneous uniaxial elongation at constant extension rate $\dot{E}$. Clearly the Type II analysis, which incorporates the history of the actual force, radius and elongation rate experienced by the fluid element at the mid-plane of the elongating column, provides an accurate estimate of the desired material function. Curves similar to those computed in Fig. 25 at large strains may be very hard to realize experimentally, however, due to the rapid decrease in the tensile force and the increasing rate of necking in the mid-plane radius of the filament.

An important observation from the constraint in eq. (28) is that any viscoelastic constitutive model with a bounded extensional viscosity at large strains can undergo a ductile failure near the middle of the filament. Of course, this failure may only happen at Hencky strains sufficiently large that it cannot be observed experimentally in a typical filament stretching device. Our numerical simulations thus suggest that there is an intrinsic limitation to the maximum Hencky strain that can be obtained in filament stretching devices and other similar elongational rheometers. The transient Trouton ratio predicted for a single mode Giesekus model at $De = 0.98$ is shown on a linear scale in Fig. 26 as a function of both the axial Hencky strain ε_p (i.e. the strain based on the motion of the end-plates, see eq. (2)) and the effective strain $\varepsilon_{\rm eff}$ (based on the deformation of the mid-plane radius). At the end of the simulation the elapsed time is $t_{\rm final}/\lambda_1 = 3.89$, corresponding to a maximum axial strain of $\varepsilon_p = 3.8$. However, the total effective strain experienced by fluid elements at the mid-plane is much larger due to the rapid necking in the filament mid-plane radius at later times and can be computed from equation (4) to be $\varepsilon_{\rm eff} \approx 9.78$. Since the polymeric stress has saturated, whereas the effective extensional strain rate continues to increase, the apparent Trouton ratio computed from eq. (7) passes through a maximum at an intermediate value of the Hencky strain and then begins to decrease before numerical convergence of the solution is ultimately lost at $\varepsilon_p \approx 3.85$. We have never observed such behavior in our experiments, possibly because of limitations in the minimum measurable tensile force and total attainable strain; however, both Münstedt & Laun and Meissner have observed similar overshoots in their measurements of the transient Trouton ratio in LDPE [50]. In these experiments the tensile stress was found to grow, saturate as the material attained its steady uniaxial extensional viscosity and then, showed a small decrease immediately before the elongating strip of polymer failed. It thus appears plausible that the physical mechanism leading to this measured overshoot is the onset of a ductile viscoelastic failure in the sample.

6. CONCLUSIONS

In this paper we have used computational rheology to investigate the utility of filament stretching devices in measuring the tensile stress growth of weakly strain-hardening fluids during uniaxial elongation. Numerical simulations using single and multi-mode formulations of the Giesekus model coupled with experimental measurements using a 5.0 wt.% monodisperse polystyrene solution have shown that it is possible to quantitatively measure the transient uniaxial extensional viscosity over a range of strain rates. Although the deformation in the elongating fluid filament is neither spatially nor temporally homogeneous when a single uniaxial stretching profile is applied to the end-plate of the device, accurate measurements of the tensile force and the rate of deformation

of fluid elements near the mid-plane of the filament, in combination with an appropriate force balance, are sufficient to extract the transient extensional viscosity function. The results are expected to be even more accurate over a wider range of deformation rates if the experiments are performed using a modified velocity profile that ensures temporal homogeneity of the mid-plane kinematics. However such measurements have not been attempted yet for these weakly-strain-hardening materials.

Excellent agreement is obtained between the experiments and the numerical simulations performed using nonlinear model parameters obtained from regression to independent rheological experiments in shear and mixed shearing-extensional flows [23]. This indicates that, with careful analysis, data obtained from filament stretching devices are accurate enough for the *a priori* fitting of nonlinear constitutive parameters rather than the *a posteriori* confirmation of parameter values that have already been determined in other rheological experiments . This predictive ability will prove especially useful for fluids that are rheologically more complex than the relatively simple entangled solution of monodisperse linear homopolymer that was employed in the present study. Many of the nonlinear constitutive equations that characterize complex fluids (e.g. such as branched polymeric fluids) frequently contain model parameters which have little or no effect on the steady or transient shear flow material functions, and accurate measurements of the transient extensional viscosity using filament stretching devices can thus be used to obtain appropriate values of these material constants.

Numerical simulations with the Giesekus model at moderate Deborah numbers have also shown that the rate of necking in the fluid filament increases exponentially with Hencky strain and thus appear to indicate that the filament will eventually fail or 'rupture' in a finite time, although of course numerical calculations are terminated before this event due to lack of spatial mesh resolution in the middle of the filament. This necking down in the filament profile can be understood, at least qualitatively, in terms of a Considére criterion in which homogeneous elongation of a viscoelastic filament is unstable when the tensile force passes through a maximum. Similar arguments were first made by Pearson and Connelly [51] and the criterion has been shown to provide quantitative results at very high Deborah numbers by Hassager et al. [23].

Of course, this simple criterion cannot capture other features of the necking such as the dependence of the filament evolution on initial aspect ratio nor can it predict the rate of necking that develops. However, our simulations with FENE-P and Giesekus models having identical *steady state* extensional viscosities show that the study of such dynamical phenomena as evolution and failure of viscoelastic filaments is intimately connected with detailed knowledge of the *transient*

extensional rheology of the material.

From an experimental viewpoint, viscoelastic enhancement of the rate of necking (and the possibility of filament failure at a finite time) places an intrinsic limit on the maximum Hencky strain that can be achieved for many viscoelastic materials regardless of mechanical limitations in stage length, motor torque and force transducer sensitivity. Despite this limitation, our numerical and experimental results show that even during the dynamic event of failure, accurate measurements of the total viscoelastic force and the rate of necking can be used to monitor the evolution in the elongational viscosity of the fluid. Furthermore, as pointed by Malkin and Petrie [27], failure and rupture are some of the least understood features of the rheological behavior of polymeric liquids. Filament stretching experiments have now documented several modes of material failure (e.g. gradual cohesive necking near the mid-plane and meniscus instability leading to fibril formation near a solid substrate) that are commonly observed in adhesives and other viscoelastic materials, and in the future filament stretching rheometers may prove to be ideal devices to study such mechanisms under carefully controlled kinematic conditions.

ACKNOWLEDGMENTS

This work was supported by NASA's Microgravity Science and Application Program. We would like to thank Benoit Debbaut at Polyflow, s.a. for his technical support for solving transient multi-mode free surface problems with Polyflow. Computer system and graphics support from David A. Thompson at the Computational Microgravity Lab, NASA Lewis Research Center is acknowledged. GHM would like to acknowledge the insightful comments of O. Harlen, O. Hassager and J.W. Hutchinson.

REFERENCES

[1] J.E. Matta and R.P. Tytus, *J. Non-Newtonian Fluid Mech.* **35** (1990) 215-229.

[2] T. Sridhar, V. Tirtaatmadja, D.A. Nguyen and R.K. Gupta, *J. Non-Newtonian Fluid Mech.* **40** (1991) 271-280.

[3] V. Tirtaatmadja and T. Sridhar, *J. Rheol.* **37** (1993) 1081-1102.

[4] S. Berg, R. Kröger and H.J. Rath, *J. Non-Newtonian Fluid Mech.* **55** (1994) 307-319.

[5] S.H. Spiegelberg, D.C. Ables and G.H. McKinley, *J. Non-Newtonian Fluid Mech.* **64** (1996) 229-267.

[6] M.J. Solomon and S.J. Muller, *J. Rheol.,* **40** (1996) 837-856.

[7] A. Jain, D.S. Shackleford and K.W. Koelling, *The 68th Society of Rheology Annual Meeting* (1997).

[8] J. van Nieuwkoop and M.M.O. Muller von Czernicki, *J. Non-Newtonian Fluid Mech.* **67** (1996) 105-123.

[9] M.R.J. Verhoef, B.H.A.A. van den Brule and M.A. Hulsen, *J. Non-Newtonian Fluid Mech.* **80** (1997) 155-182.

[10] R.B. Bird, R.C. Armstrong, and O. Hassager, *Dynamics of Polymeric Liquids*, Vol. 1 *Fluid Mechanics*, 2nd edn, John Wiley & Sons, 1987.

[11] R.W.G. Shipman, M.M. Denn and R. Keunings, *J. Non-Newtonian Fluid Mech.* **40** (1991) 281-288.

[12] S. Gaudet, G.H. McKinley and H.A. Stone, *Phys. Fluids.,* **8** (1996) 2568-2579.

[13] S. Gaudet and G.H. McKinley, *Comput. Mech.* **21** (1998) 461-476.

[14] M. Yao and G.H. McKinley, *J. Non-Newtonian Fluid Mech.* **74** (1998) 47-88.

[15] R. Sizaire and V. Legat, *J. Non-Newtonian Fluid Mech.* **71** (1997) 89-107.

[16] M.I. Kolte, H.K. Rasmussen and O. Hassager, *Rheol. Acta* **36** (1997) 285-302.

[17] P. Szabo, *Rheol. Acta* **36** (1997) 277-284.

[18] S.H. Spiegelberg and G.H. McKinley, *J. Non-Newtonian Fluid Mech.* **67** (1997) 49-76.

[19] H.K. Rasmussen and O. Hassager, *J. Non-Newtonian Fluid Mech.* (1998), In Press.

[20] X. Zhang, R. S. Padgett and O. Basaran, *J. Fluid Mech.* **329** (1996) 207-245.

[21] J. Eggers, *Rev. Mod. Phys.,* **69** (1997) 865-929.

[22] Tomotika, *Proc. Roy. Soc. Ser. A,* **153** (1936) 302-318.

[23] O. Hassager, M.I. Kolte and M. Renardy, *J. Non-Newtonian Fluid Mech.* **76** (1998) 137-152.

[24] J. Meissner, *Ann. Rev. Fluid Mech.* **17** (1985) 45-64.

[25] J.M. Li, W. Burghardt, B. Yang and B. Khomami, *J. Non-Newtonian Fluid Mech.* **74** (1998) 151-194.

[26] Y.W. Ooi and T. Sridhar, *J. Non-Newtonian Fluid Mech.* **52** (1994) 153-162.

[27] A.Y. Malkin and C.J.S. Petrie, *J. Rheol.* **41** (1997) 1-25.

[28] D.O. Olagunju, Viscoelastic Filament Under Exponential Stretching, *J. Non-Newtonian Fluid Mech.* (1999), submitted.

[29] M. Renardy, *J. Non-Newtonian Fluid Mech.* **59** (1995) 267-282.

[30] M. Yao, G.H. McKinley and B. Debbaut, *J. Non-Newtonian Fluid Mech.* **79** (1998) 469-501.

[31] M. Considère, *Annales des Ponts et Chaussées,* **9** (1885) 574.

[32] E.W. Hart, *Acta Metallurgica,* **15** (1967) 351-355.

[33] D.F. James and K.A. Walters, in A.A. Collyer (ed.), *Techniques in Rheological Measurement*, Chapman & Hall, London, 1993, Chapter 2.

[34] M. Yao and G.H. McKinley, in preparation (1999).

[35] H. Giesekus, *J. Non-Newtonian Fluid Mech.* **11** (1982) 69-109.

[36] R.B. Bird and J.M. Wiest, *J. Rheol.* **29** (1985) 519-532.

[37] R.B. Bird, R.C. Armstrong, and O. Hassager, *Dynamics of Polymeric Liquids*, Vol. 2 *Kinetic Theory*, 2nd edn, John Wiley & Sons, 1987.

[38] R.B. Bird, P.J. Dotson and N.L. Johnson, *J. Non-Newtonian Fluid Mech.* **7** (1980) 213-235.

[39] C.J.S. Petrie, *J. Non-Newtonian Fluid Mech.* **34** (1990) 37-62.

[40] Polyflow User's Manual, ver. 3.5.0, Polyflow s.a., Place de l'Université 16, B-1348 Louvain-la-Neuve, Belgium (1996).

[41] J.F. Thompson, Z.U.A. Warsi and C. Wayne Mastin, *Numerical Grid Generation - Foundations and Applications*, Elsevier, 1985.

[42] O. Hassager, Private communication (1998).

[43] R.G. Larson, *J. Non-Newtonian Fluid Mech.* **12** (1983) 303-315.

[44] E. Chater and J.W. Hutchinson, Mechanical Analogs of Coexistent Phases, in *Phase Transitions and Material Instabilities in Solids*, Academic Press, New York, 1984.

[45] L.E. Malvern, *Introduction to the Mechanics of a Continuous Medium*, Prentice-Hall, Englewood Cliffs, N.J., 1969.

[46] Y.L. Joo and E.S.G. Shaqfeh, *Phys. Fluids A,* **4** (1992) 2415-2431.

[47] M.B. Rubin and A.L. Yarin, *J. Non-Newtonian Fluid Mech.* **50** (1993) 79-88.

[48] Y. Ide and J.L. White, *J. Appl. Polym. Sci.* **22** (1978) 1061-1079.

[49] V.M. Entov and E.J. Hinch, *J. Non-Newtonian Fluid Mech.* **72** (1997) 31-54.

[50] J. Meissner, *Chem. Eng. Commun.* **33** (1985) 159-180.

[51] G.H. Pearson and R.W. Connelley, *J. Appl. Polym. Sci.* **27** (1982) 969-981.

FIGURE CAPTIONS

Figure 1. Steady viscometric properties of the test fluid at a reference temperature of 22°C and non-linear fits using multi-mode Giesekus model. (a) Steady shear viscosity η as a function of shear rate $\dot{\gamma}$; (b) First normal stress difference coefficient, Ψ_1.

Figure 2. Mathematical model of the filament stretching device. (a) Initial configuration of the cylindrical liquid bridge. (b) Subsequent extensional deformation of the liquid bridge.

Figure 3. Comparison of extensional deformations characterized by free surface profiles of the filament as a function of Hencky strain ε_p for three typical constitutive models: a viscous Newtonian fluid (N), a weakly strain-hardening fluid simulated by a 1-mode Giesekus model (G) and a strongly strain-hardening fluid simulated using the Oldroyd-B model (O). The material properties of the shear-thinning test fluid are given in Table 1 and the stretching rate is $\dot{E} = 4.68 s^{-1}$ corresponding to $De \approx 2.0$ for the viscoelastic fluids.

Figure 4. An enlarged view of the extensional deformations at a Hencky strain of $\varepsilon_p = 3.4$ in the local 'foot' area near the stationary end-plate for the three different fluid filaments shown in Fig. 3. The locations of the individual mesh points are shown by the symbols.

Figure 5. Images of the free surface during extensional deformation in the filament stretching device, recorded using a CCD camera with 640×480 pixels and 8 bit gray-scale resolution.

Figure 6. Evolution of the free surface perturbation $\delta R(z, \varepsilon_p)$ defined in eq. (1) measuring the deviation between the actual axial profile computed for the Oldroyd-B fluid and the ideal uniaxial elongational flow.

Figure 7. Free surface perturbation $\delta R(z, \varepsilon)$ shows the growing difference between the axial free surface profile computed for the Giesekus model and the corresponding response of a Newtonian fluid.

Figure 8. Time history of the mid-plane radius, R_{mid}, for three different constitutive models. The curve labeled $e^{-0.5\varepsilon}$ corresponds to homogeneous deformation in uniaxial elongational flow. The curve marked $e^{-0.75\varepsilon}$ is the prediction from the lubrication solution [5].

Figure 9. Temporal variation of the local extension strain rate at the mid-plane between the two end-plates at a Deborah number $De = 1.68$. The local strain rate is characterized by the effective extension strain rate, $\dot{\varepsilon}_{\mathrm{eff}}$ defined in eq. (3), and the pointwise value of D_{zz} at the center of the liquid bridge, $r = 0$, $z = 0$.

Figure 10. (a) Evolution in the effective extension strain rate for three different constitutive models. (b) The non-dimensional enhancement in extension rate $(\dot{\varepsilon}_{\text{eff}}-\dot{\varepsilon}_{\text{ref}})/\dot{\varepsilon}_{\text{ref}}$ for the Giesekus model, where the Newtonian curve shown in (a) is used as the reference. The imposed axial extension rate is $\dot{E}=4.68s^{-1}$ in each case. The difference between the Newtonian and the viscoelastic deformation rate grows exponentially with Hencky strain.

Figure 11. A quantitative comparison of the flow kinematics for three constitutive models. The extensional flow kinematics are characterized by the axial velocity gradient D_{zz} along the centerline $r=0$. The relevant parameter values are $De=1.97$, $1/Ca=0$, $\Lambda_0=0.54$, $\beta=0.26$ and $\alpha=0.3162$.

Figure 12. Test run 1: $De=0.98$ and $\Lambda_0=0.58$. Comparison of the Trouton ratio predicted by a 1-mode Giesekus model with the experimental data for a weakly strain-hardening fluid described in Table 1. (a) Comparison based on the type IB analysis defined in eq. (6b). The curves $1/Ca=0.106$ and 0 correspond to computations with and without surface tension, respectively. (b) Comparison based on the type II analysis defined in eq. (7). The curve denoted 'Constant Stretch Rate' refers to the theoretical solution for the 1-mode Giesekus model under homogeneous uniaxial elongational flow conditions with a constant extension rate $\dot{E}$; while the curve labeled 'Variable Stretch Rate' is the theoretical solution calculated using the time-dependent deformation rate $\dot{\varepsilon}_{\text{eff}}$.

Figure 13. Test run 2: $De=1.44$ and $\Lambda_0=0.63$. Comparison of the Trouton ratio predicted by a 1-mode Giesekus model with experimental data for the polystyrene solution. (•) Experimental measurements processed using the type IB analysis; (- - -) numerical computation processed using the type IB analysis; (solid triangle) numerical computation processed using the type II analysis; (—) theoretical solution for homogeneous uniaxial elongation at constant Deborah number $De=1.44$.

Figure 14. Test run 3: $De=1.89$ and $\Lambda_0=0.54$. Comparison of the Trouton ratio predicted by a 1-mode Giesekus model with experimental data for the polystyrene solution. (•) Experimental measurements processed using the type IB analysis; (- - -) numerical computation processed using the type IB analysis; (solid triangle) numerical computation processed using the type II analysis; (—) theoretical solution for homogeneous uniaxial elongation at constant Deborah number $De=1.89$.

Figure 15. Effects of the initial aspect ratio on the radial deformation of a viscoelastic liquid bridge simulated using a 1-mode Giesekus model. The non-dimensional mid-plane radius is

shown as a function of the imposed axial Hencky strain ε_p defined in eq. (2). The curves labeled $e^{-0.5\varepsilon}$ and $e^{-0.75\varepsilon}$ are the same as explained in the caption of Fig. 8.

Figure 16. Effects of the initial aspect ratio on the local extensional deformation at the mid-plane between the two end-plates. The rate of deformation is characterized by the effective extensional strain rate $\dot{\varepsilon}_{\text{eff}}$.

Figure 17. Effect of the initial aspect ratio on spatial non-homogeneity of polymer stress characterized by the radial variation of the tensile stress component, $\tau_{p,zz}$, on the mid-plane between the end-plates ($z = 0$). The radial profiles are shown at (a) a small Hencky strain of $\varepsilon_p = 0.2$ and (b) a large strain of $\varepsilon_p = 3.8$.

Figure 18. Effect of the initial aspect ratio on the predicted transient Trouton ratio analyzed using the type II formulation given in eq. (7). The 'Theory' curve refers to the theoretical prediction of the 1-mode Giesekus model for ideal uniaxial flow kinematics at constant De. The local strain ε_{eff} pertains to fluid elements at the mid-plane and is calculated according to eq. (4).

Figure 19. Effect of the mobility factor α in the 1-mode Giesekus model on flow kinematics characterized by; (a) the mid-plane radius, R_{mid}; (b) The effective extensional strain rate $\dot{\varepsilon}_{\text{eff}}$ defined in eq. (3). The broken lines labeled $e^{-0.5\varepsilon}$ and $e^{-0.75\varepsilon}$ are explained in the caption of Fig. 8.

Figure 20. Effect of the mobility factor on the free surface shape in the 'foot' area near the end-plates at a large Hencky strain of $\varepsilon_p = 3.6$.

Figure 21. Effect of the mobility factor on the transient Trouton ratio. Numerical solutions are post-processed using the type II analysis and the resulting values of the transient Trouton ratio are shown by the symbols. The three curves are theoretical predictions for the 1-mode Giesekus model based on ideal uniaxial elongational flow kinematics. The dashed line corresponding to $\alpha = 0$ is the Oldroyd-B limit.

Figure 22. Comparison of the predicted transient Trouton ratio for the multi-mode model versus the single-mode model. The experiment refers to test run 3 in Table 2. (a) Using the type IB analysis; (b) Based on the type II analysis.

Figure 23. Comparison of the simulated evolution in the mid-plane radius, R_{mid} for four different fluid models. The same axial extensional strain rate of $\dot{E} = 4.68\ s^{-1}$ is imposed for all the cases. The lines labeled $e^{-0.5\varepsilon}$ and $e^{-0.75\varepsilon}$ are explained in the caption of Fig. 8.

Figure 24. Two examples of the generalized Considère stability criterion for (a) the Giesekus model and (b) the FENE-P model, with model parameters chosen so that the steady state extensional viscosity of the two fluids is the same.

Figure 25. The predicted transient Trouton ratios for the two test simulations in which the values of α and L^2 are selected such that the two models have the same steady-state asymptotic value of extensional viscosity. The type II formulation is used for the data analysis. The curves labeled 'Theory' correspond to predictions for ideal uniaxial elongation at a constant Deborah number.

Figure 26. The local maximum in the transient Trouton ratio predicted by the 1-mode Giesekus model. The numerical results are plotted on a linear scale as a function of both the axial Hencky strain ε_p imposed by the end-plates and also as a function of the effective strain ε_{eff} experienced near the mid-plane of the filament.

TABLE 1. Material properties of a weakly strain-hardening, 5 wt% solution of polystyrene and parameters of a three relaxation-mode Giesekus model fit given by Li and Burghardt [25]

Parameter	Symbol [Unit]	Mode 1	Mode 2	Mode 3
Relaxation Time	λ_i [s]	0.421	0.0563	0.00306
Polymer Viscosity	η_i [Pa·s]	25.8	7.71	1.37
Mobility Factor	α_i [-]	0.3162	0.2422	0.0993
Density	ρ [kg/m^3]	1030		
Solvent Viscosity	η_s [Pa·s]	0.069		
Surface Tension Coef.	σ [N/m]	0.030		

TABLE 2. Geometric Parameters and Non-Dimensional Numbers

Parameter	Symbol [Unit]	Test 1	Test 2	Test 3
Plate Radius	R_0 [m]	0.0035	0.0035	0.0035
Initial Aspect Ratio	Λ_0 [-]	0.583	0.629	0.54
Extension Rate	$\dot{E}$ [s^{-1}]	2.32	3.42	4.48
Reynolds Number	$Re = \rho \dot{E} R_0^2 / \eta_0$	8.4×10^{-4}	1.2×10^{-3}	1.6×10^{-3}
Capillary Number	$Ca = \eta_0 \dot{E} R_0 / \sigma$	9.46	13.94	18.27
Bond Number	$Bo = \rho g R_0^2 / \sigma$	~ 0	~ 0	~ 0
Deborah Number	$De = \lambda_1 \dot{E}$	0.98	1.44	1.89

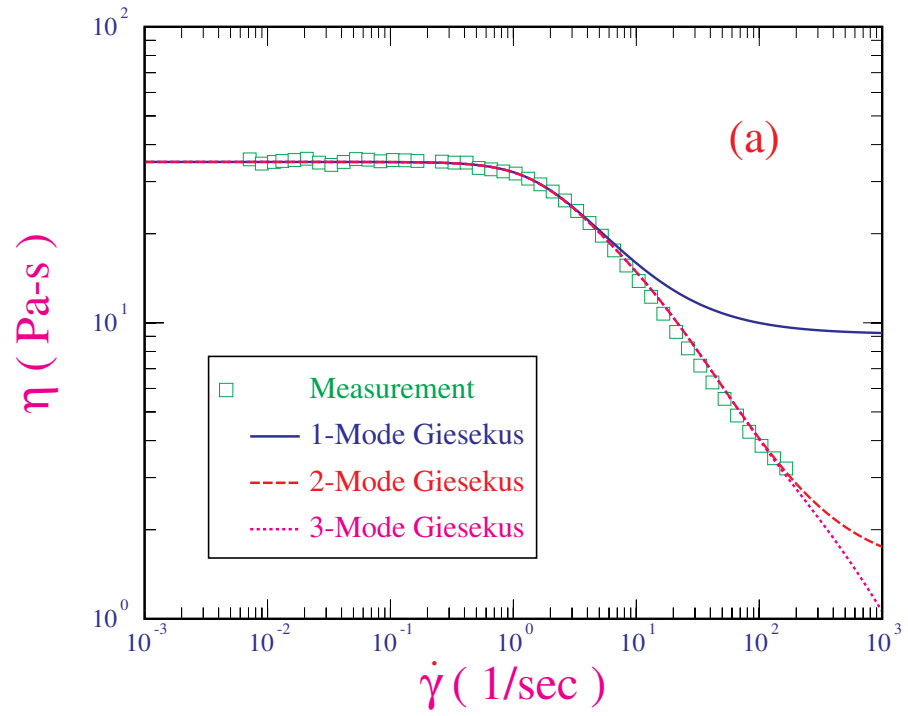
(a)
η (Pa-s)
Measurement
1-Mode Giesekus
2-Mode Giesekus
3-Mode Giesekus
γ̇ (1/sec)

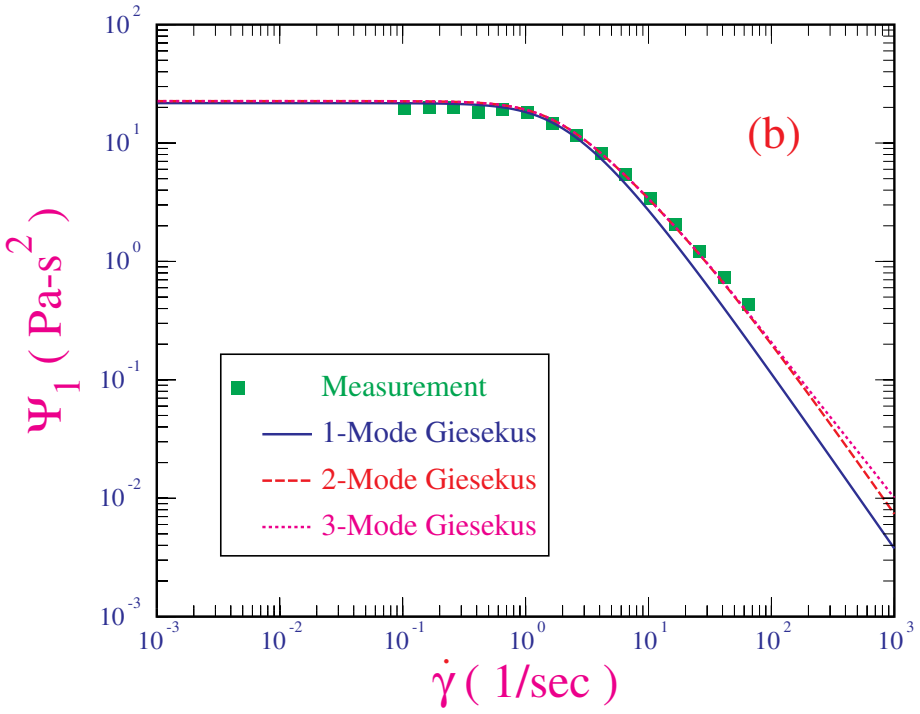
(b)
Ψ1 (Pa-s2)
Measurement
1-Mode Giesekus
2-Mode Giesekus
3-Mode Giesekus
γ̇ (1/sec)

Figure 1

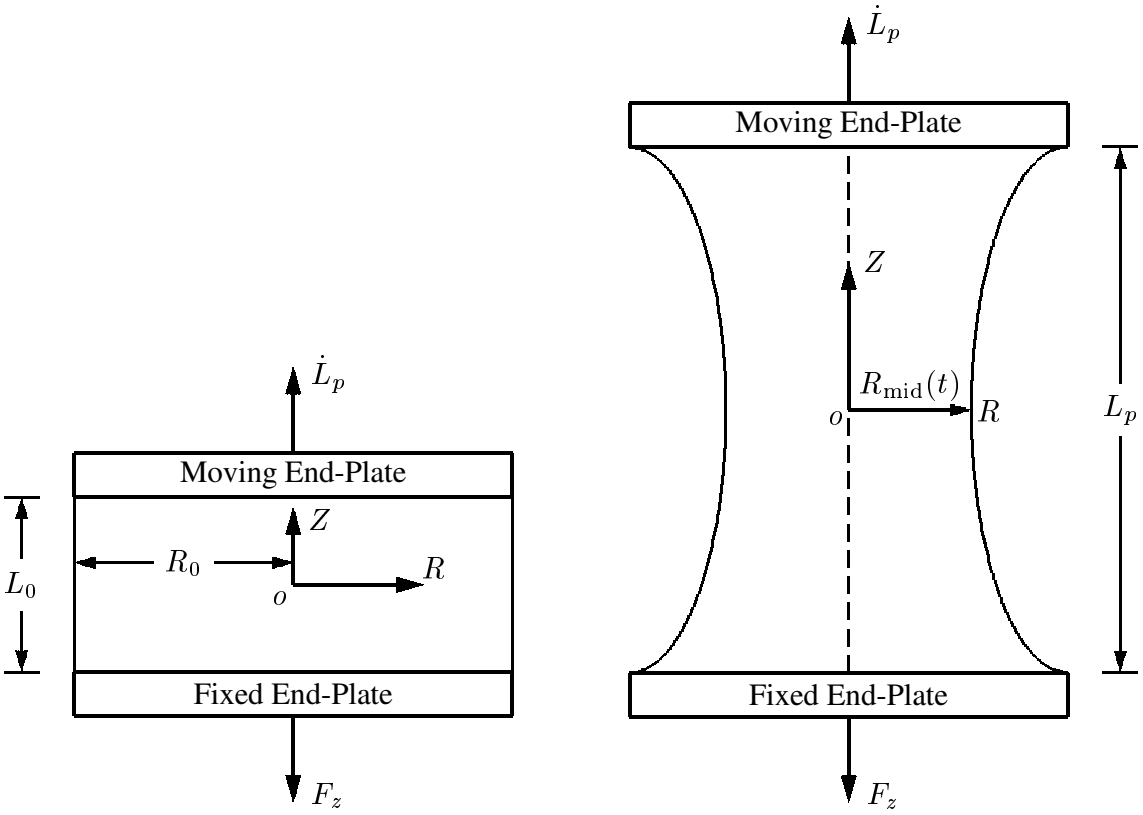

(a) $t = 0$ (b) $t > 0$

Figure 2

De = 1.97

1/Ca = 0

$\Lambda_0 = 0.54$

$\beta = 0.261$

$\alpha = 0.316$

N - Newtonian

G - Giesekus

O - Oldroyd-B

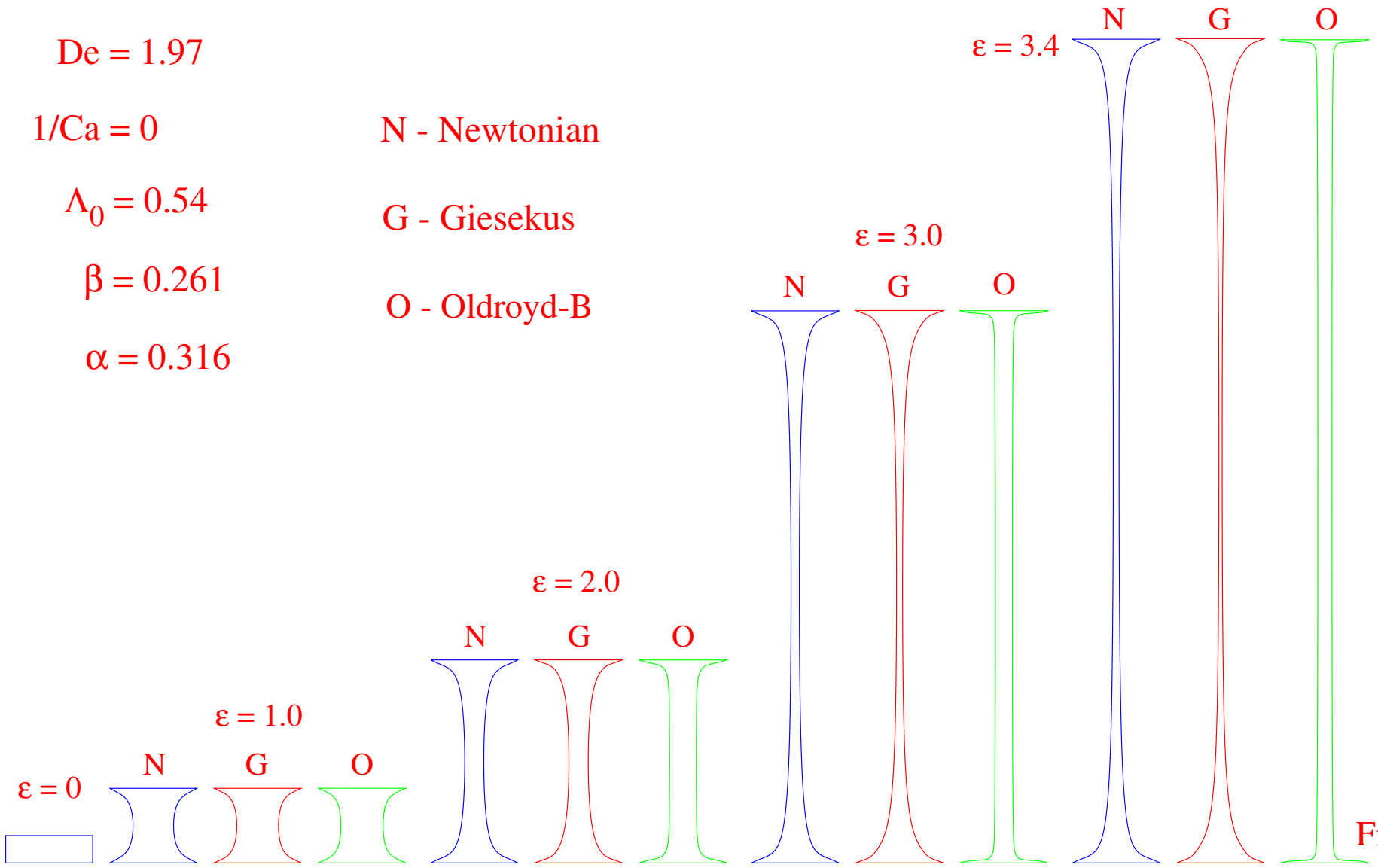

Figure 3

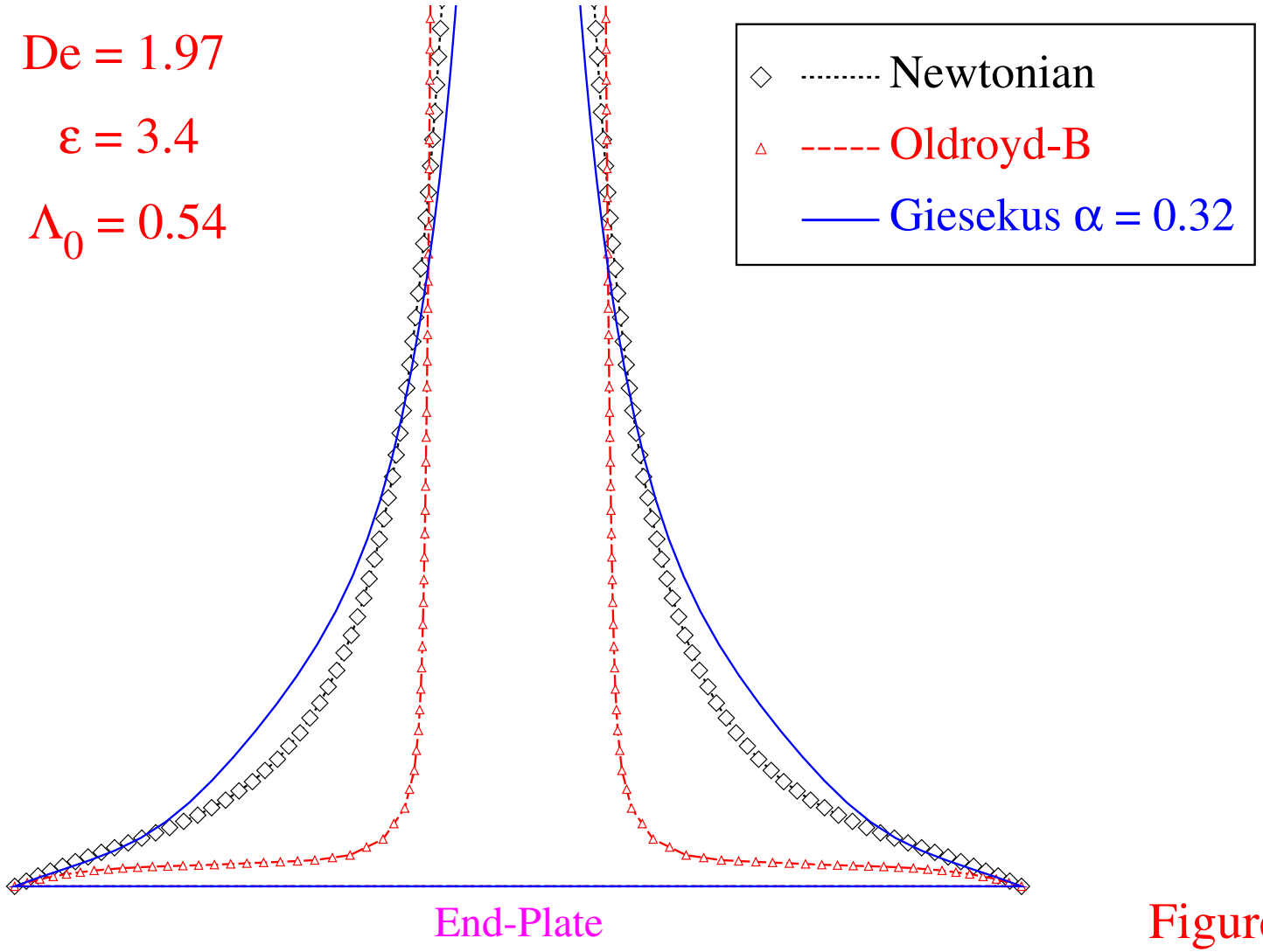
De = 1.97
ε = 3.4
Λ0 = 0.54
Newtonian
Oldroyd-B
Giesekus α = 0.32
End-Plate

Figure 4

$\varepsilon = 3.9$

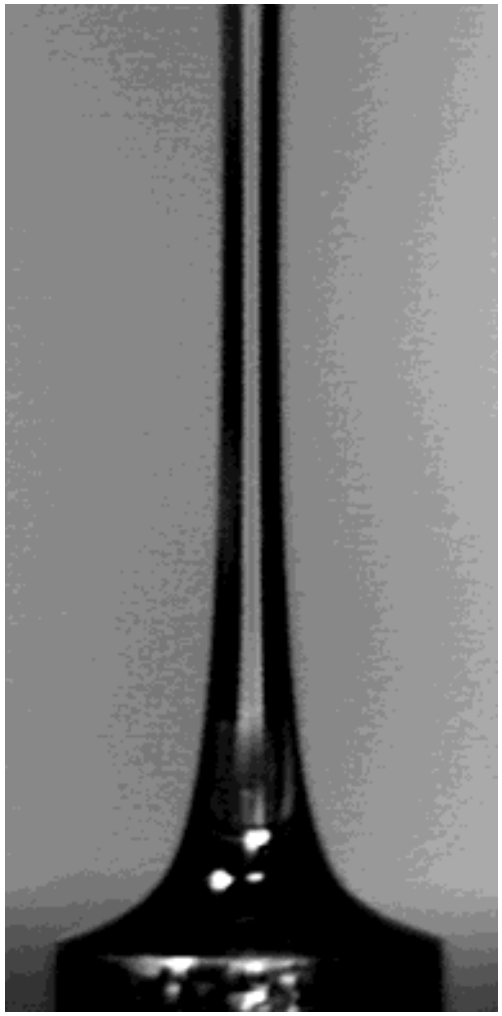

Newtonian fluid

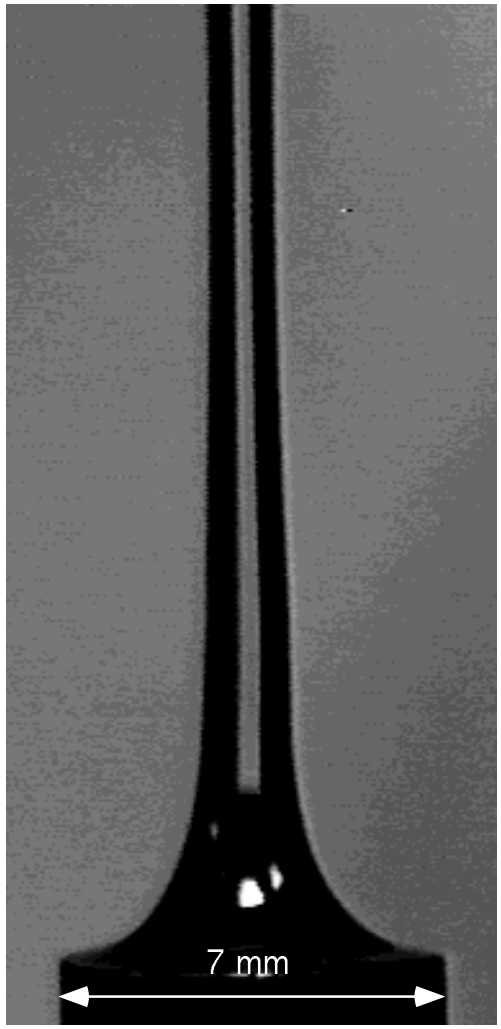

Shear-thinning fluid

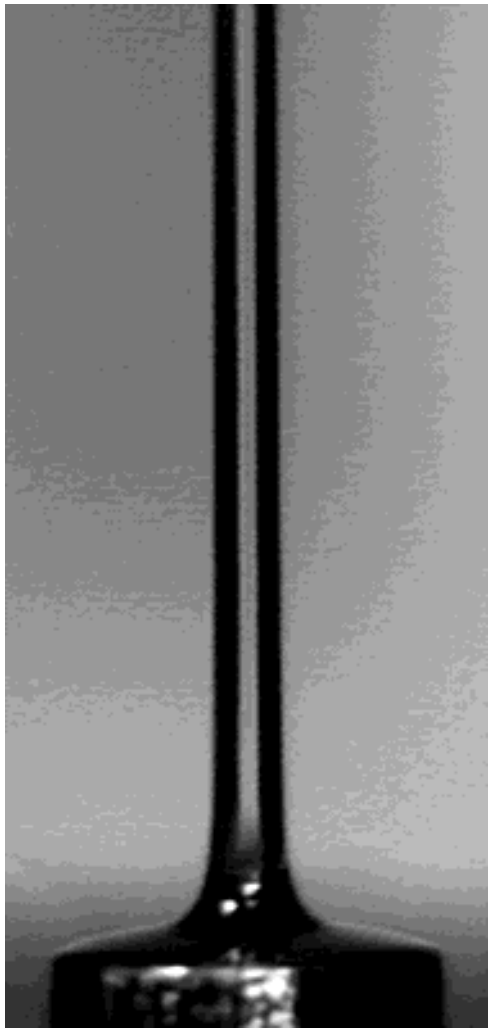

Strain-thickening fluid

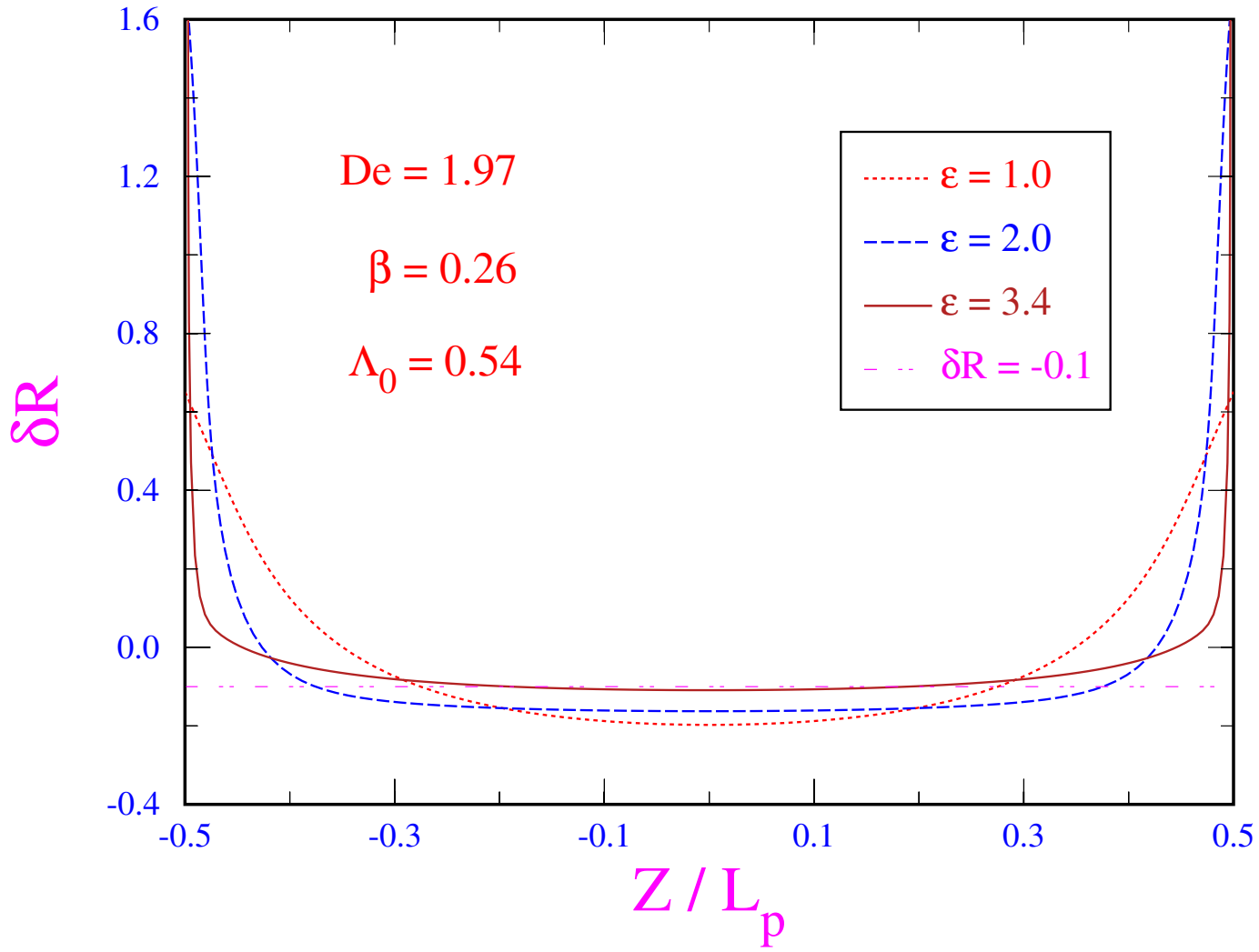
1.6
1.2
0.8
0.4
0.0
-0.4
-0.5
-0.3
-0.1
0.1
0.3
0.5
δR
Z / L_p
De = 1.97
β = 0.26
Λ_0 = 0.54
ε = 1.0
ε = 2.0
ε = 3.4
δR = -0.1

Figure 6

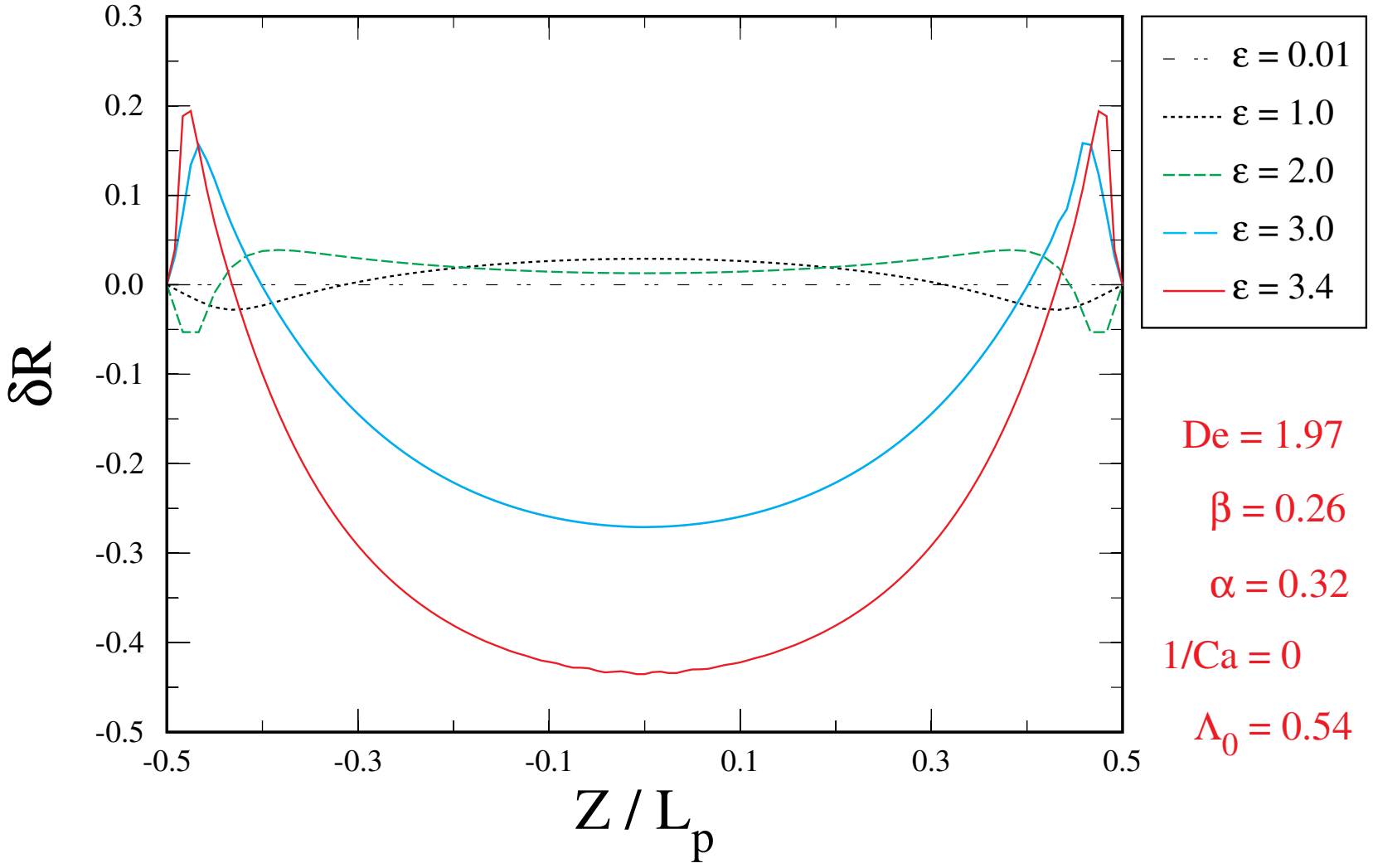
0.3
0.2
0.1
0.0
-0.1
-0.2
-0.3
-0.4
-0.5
δR
-0.5
-0.3
-0.1
0.1
0.3
0.5
Z / L_p
ε = 0.01
ε = 1.0
ε = 2.0
ε = 3.0
ε = 3.4
De = 1.97
β = 0.26
α = 0.32
1/Ca = 0
Λ_0 = 0.54

Figure 7

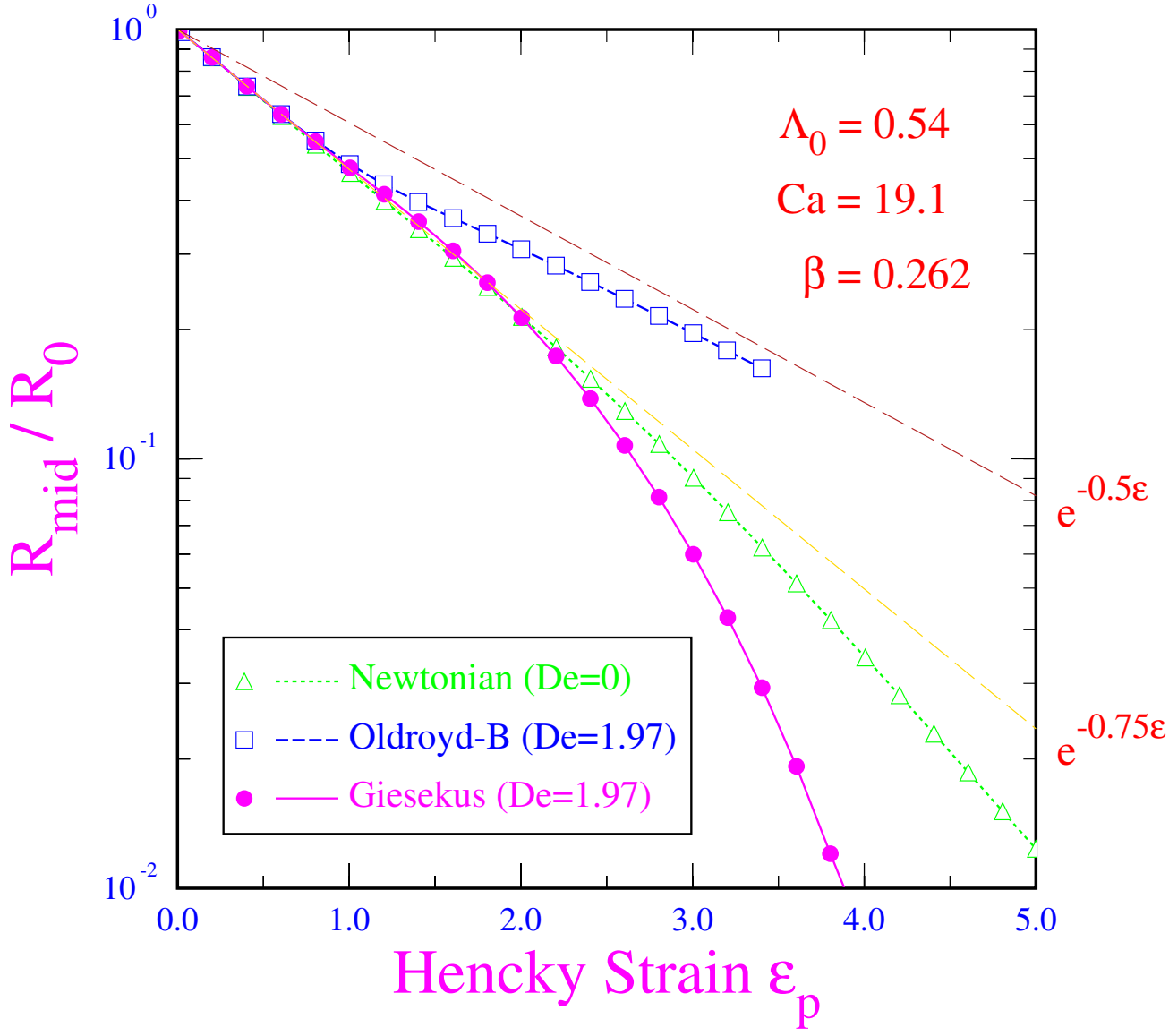
10^0
10^{-1}
10^{-2}
R_{mid} / R_0
$\Lambda_0 = 0.54$
Ca = 19.1
β = 0.262
$e^{-0.5\varepsilon}$
$e^{-0.75\varepsilon}$
Newtonian (De=0)
Oldroyd-B (De=1.97)
Giesekus (De=1.97)
0.0
1.0
2.0
3.0
4.0
5.0
Hencky Strain ε_p

Figure 8

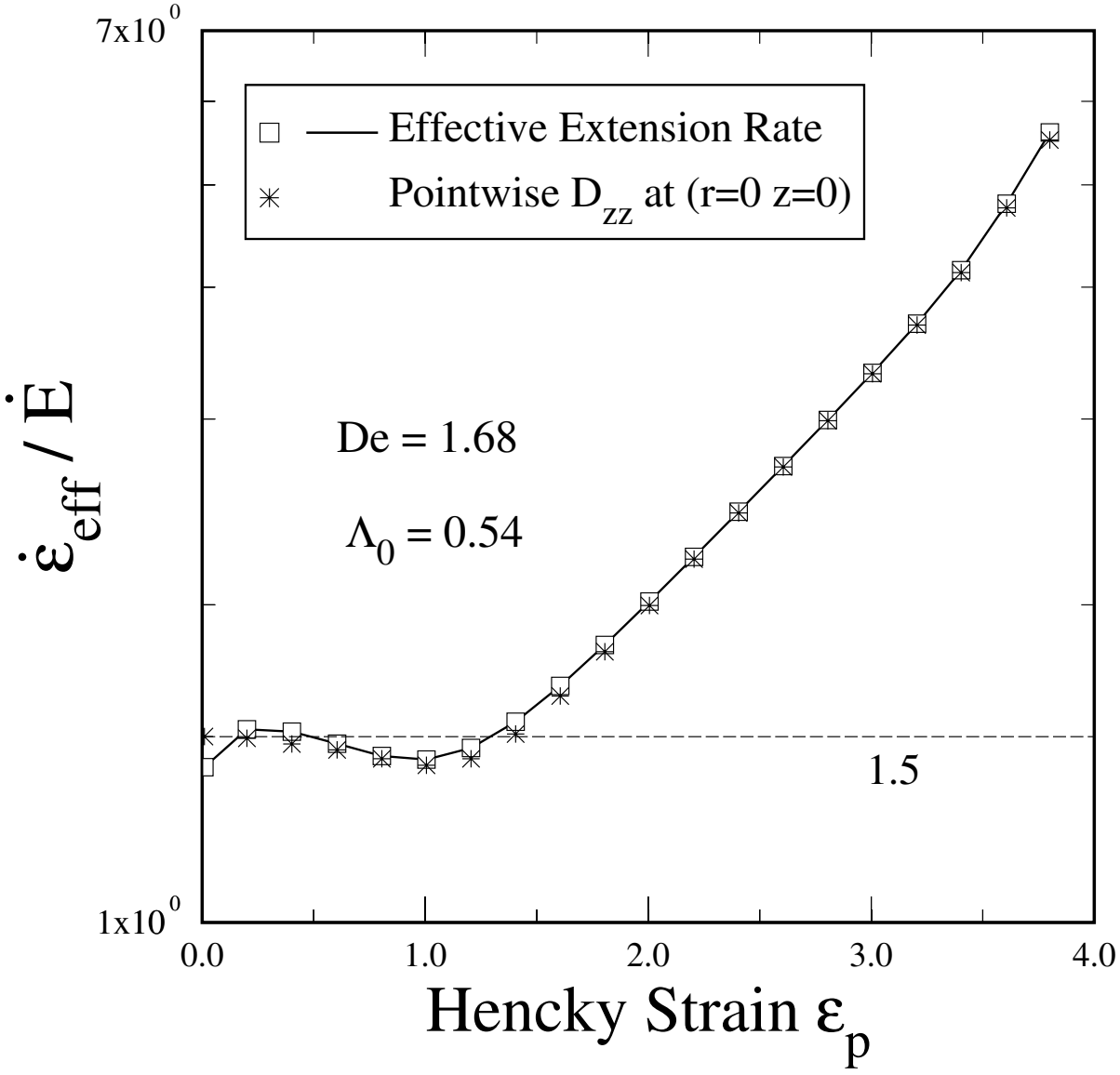
7x10^0
1x10^0
Effective Extension Rate
Pointwise D_zz at (r=0 z=0)
De = 1.68
Λ_0 = 0.54
1.5
0.0
1.0
2.0
3.0
4.0
ε̇_eff / Ė
Hencky Strain ε_p

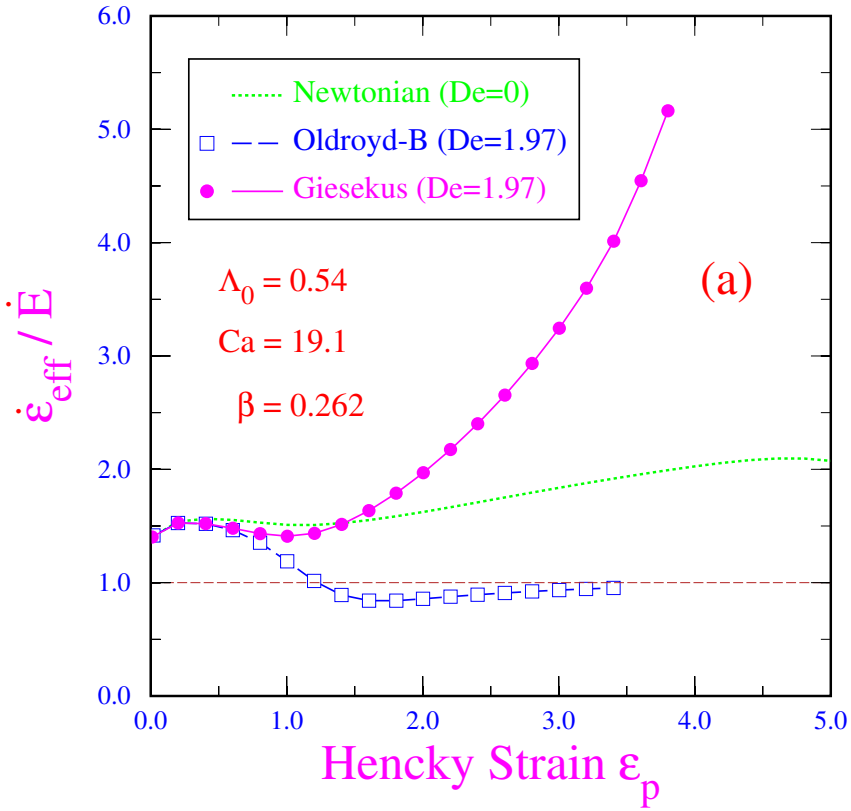
Newtonian (De=0)
Oldroyd-B (De=1.97)
Giesekus (De=1.97)
Λ_0 = 0.54
Ca = 19.1
β = 0.262
(a)
$\dot{\varepsilon}_{eff}$ / $\dot{E}$
Hencky Strain ε_p

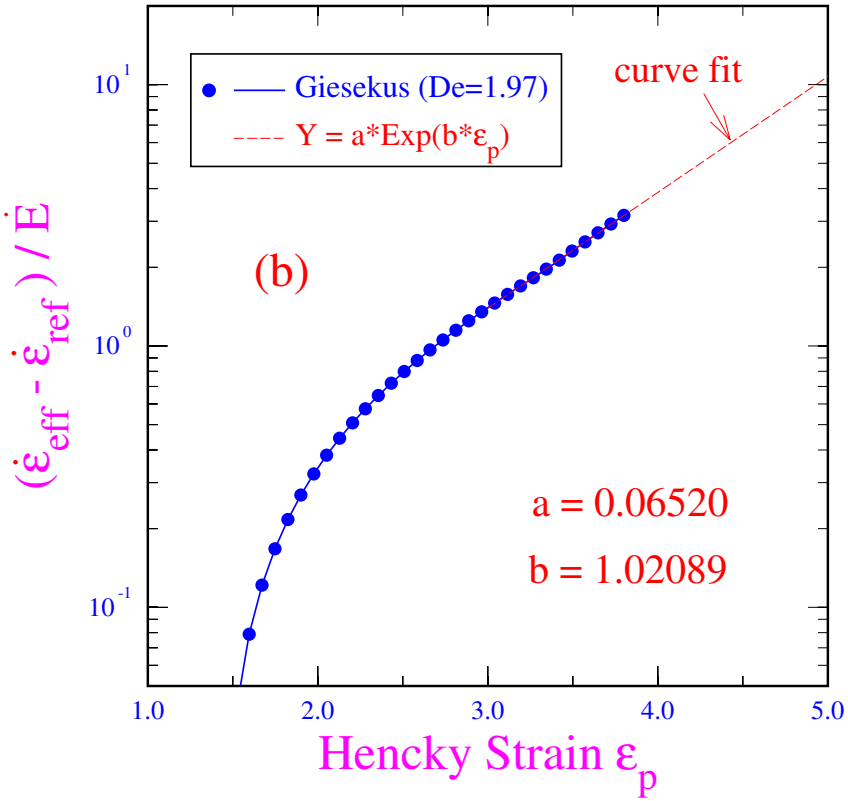
Giesekus (De=1.97)
Y = a*Exp(b*ε_p)
curve fit
(b)
a = 0.06520
b = 1.02089
($\dot{\varepsilon}_{eff}$ - $\dot{\varepsilon}_{ref}$) / $\dot{E}$
Hencky Strain ε_p

Figure 10

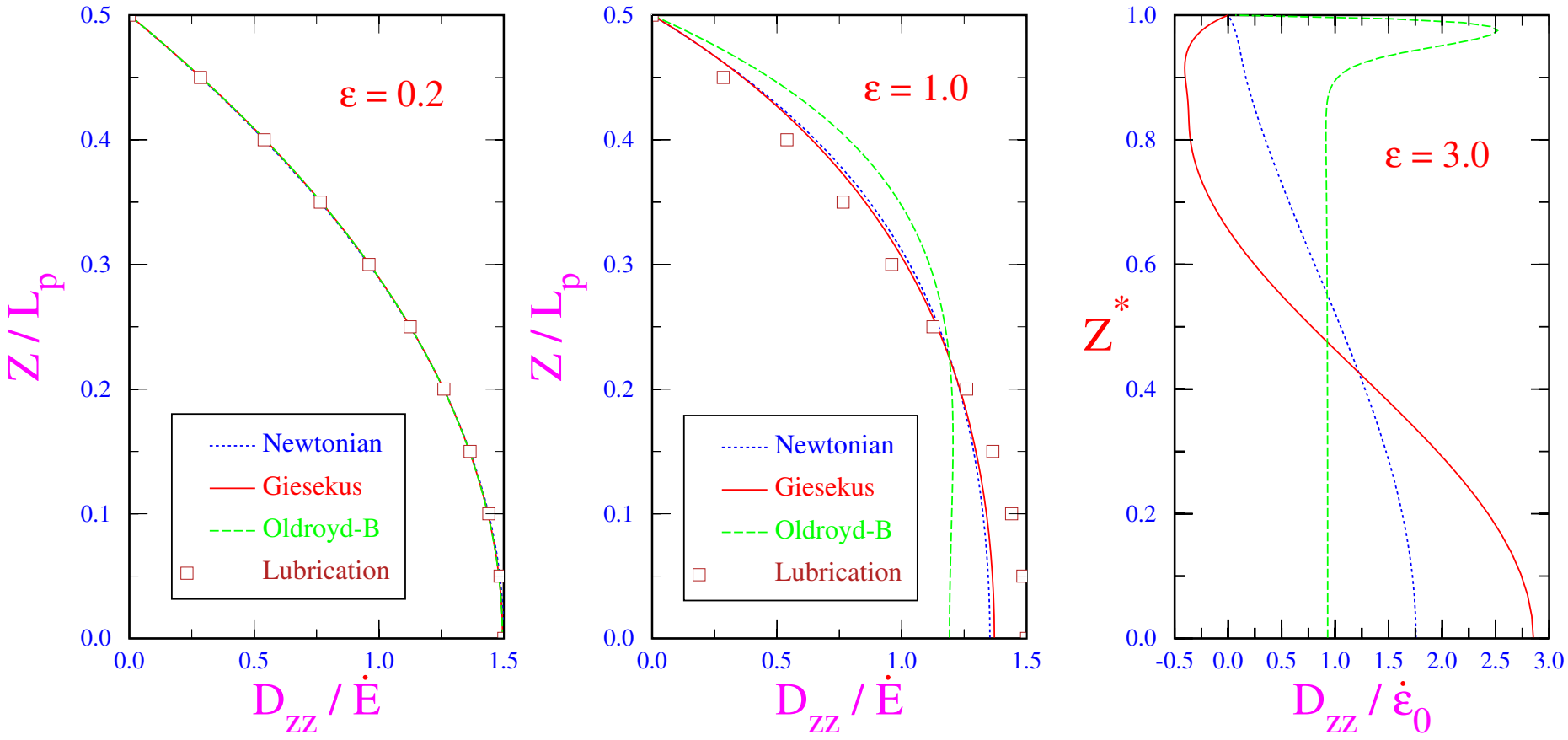
ε = 0.2
ε = 1.0
ε = 3.0
Newtonian
Giesekus
Oldroyd-B
Lubrication
Z / L_p
Z*
D_zz / Ė
D_zz / ε̇_0

Figure 11

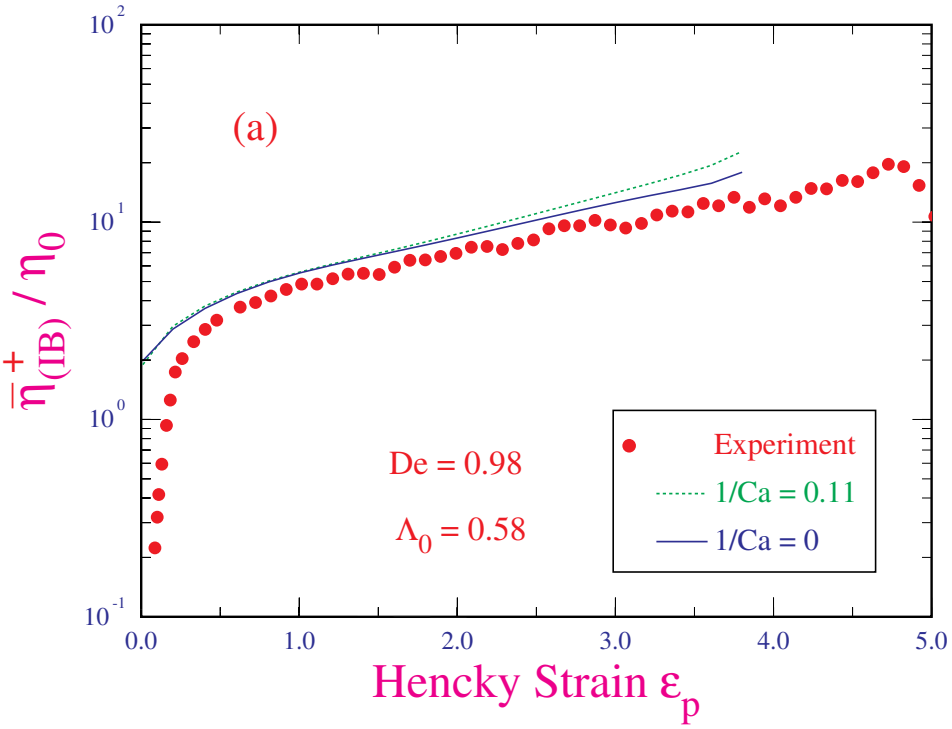
(a)
De = 0.98
Λ_0 = 0.58
Experiment
1/Ca = 0.11
1/Ca = 0
$\bar{\eta}^+_{(IB)} / \eta_0$
Hencky Strain ε_p

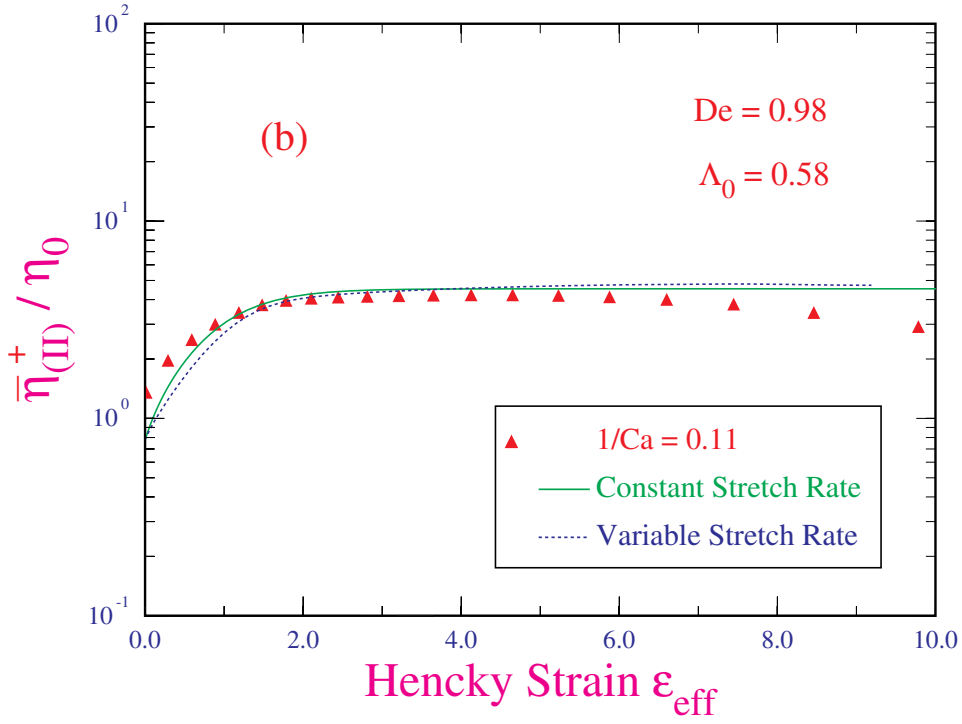
(b)
De = 0.98
Λ_0 = 0.58
1/Ca = 0.11
Constant Stretch Rate
Variable Stretch Rate
$\bar{\eta}^+_{(II)} / \eta_0$
Hencky Strain ε_{eff}

Figure 12

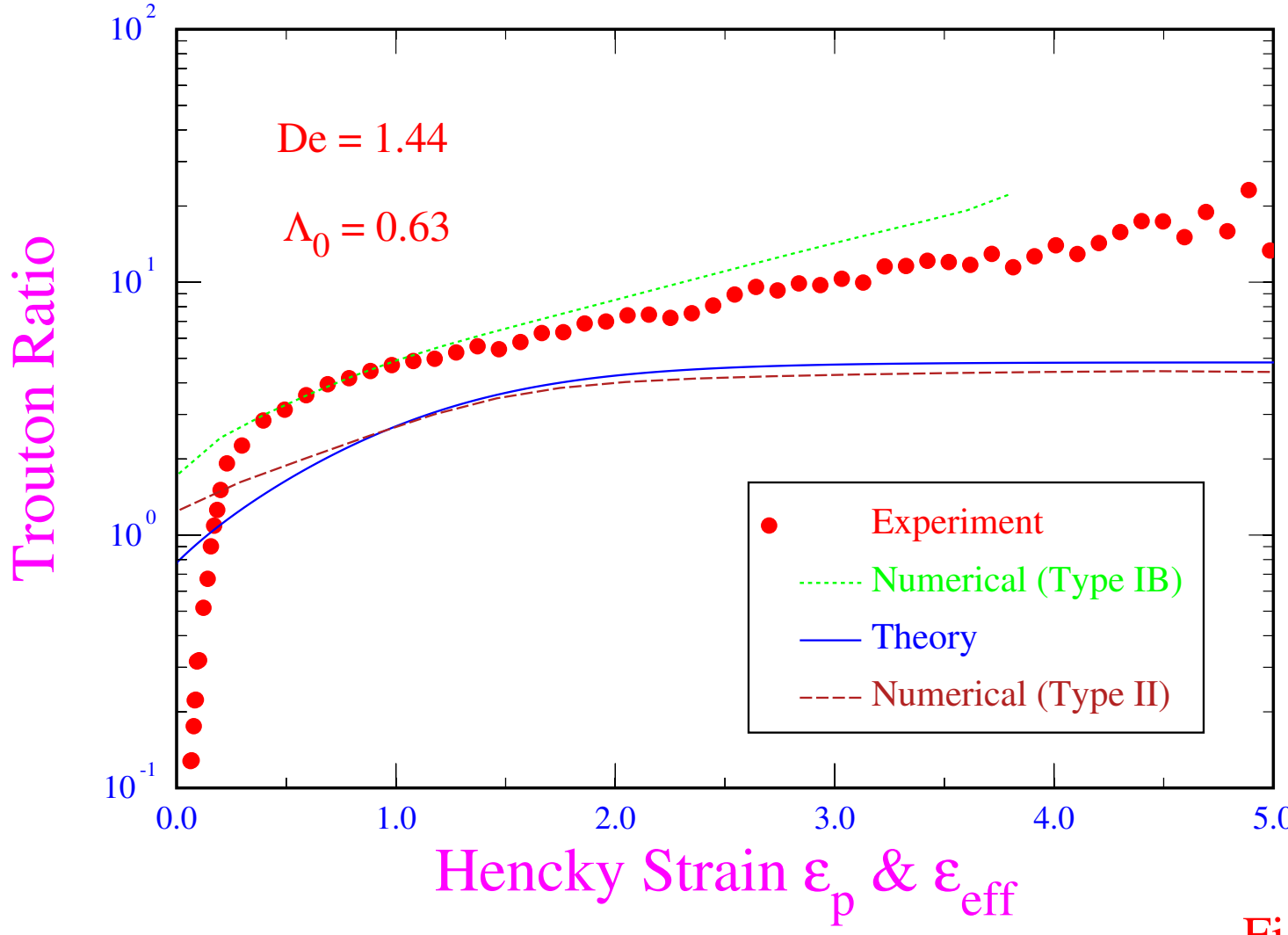
De = 1.44
Λ_0 = 0.63
Experiment
Numerical (Type IB)
Theory
Numerical (Type II)
Trouton Ratio
Hencky Strain ε_p & ε_{eff}
10^2
10^1
10^0
10^{-1}
0.0
1.0
2.0
3.0
4.0
5.0

Figure 13

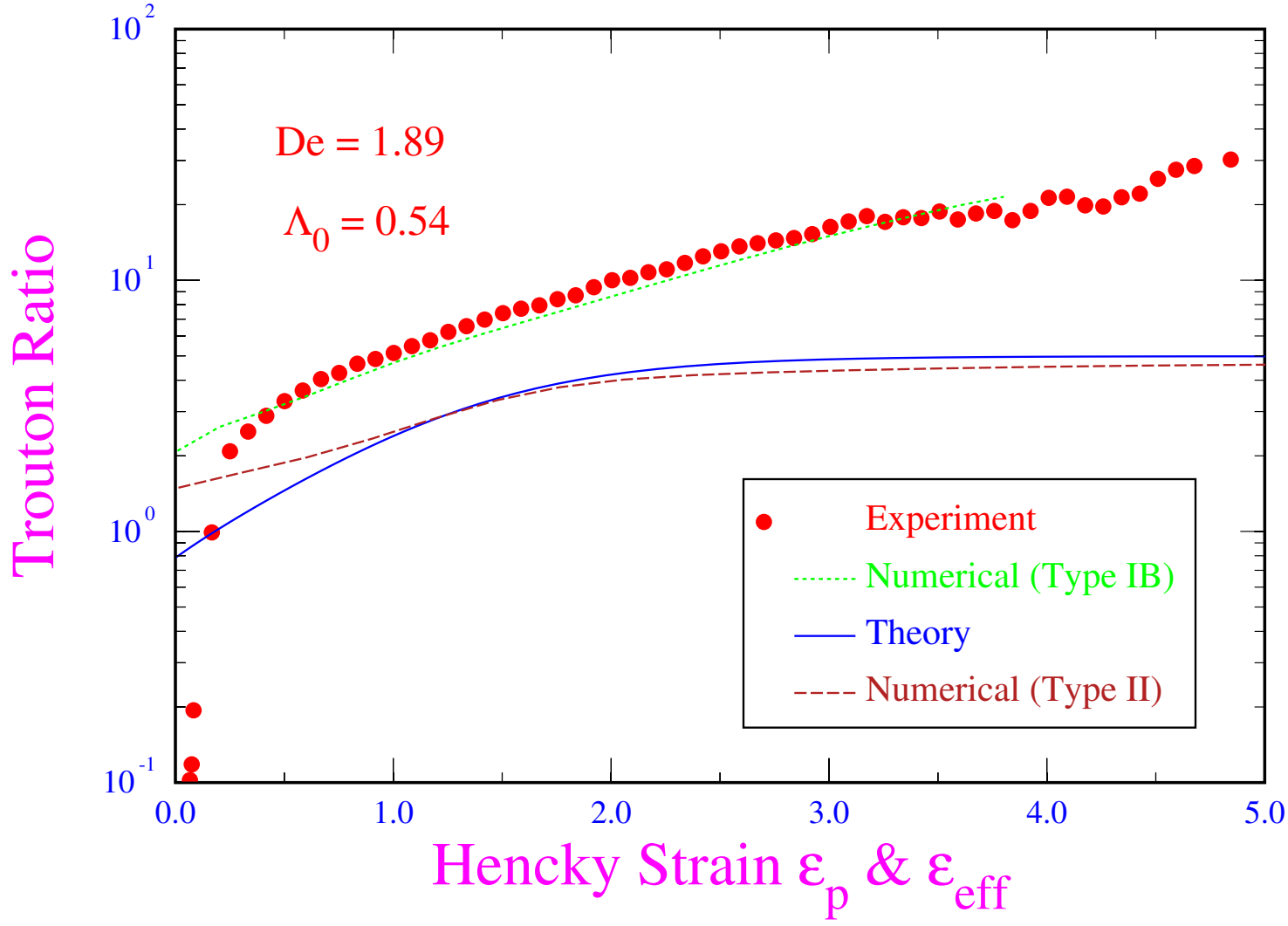
De = 1.89
Λ_0 = 0.54
Experiment
Numerical (Type IB)
Theory
Numerical (Type II)
Trouton Ratio
Hencky Strain ε_p & ε_{eff}
10^2
10^1
10^0
10^{-1}
0.0
1.0
2.0
3.0
4.0
5.0

Figure 14

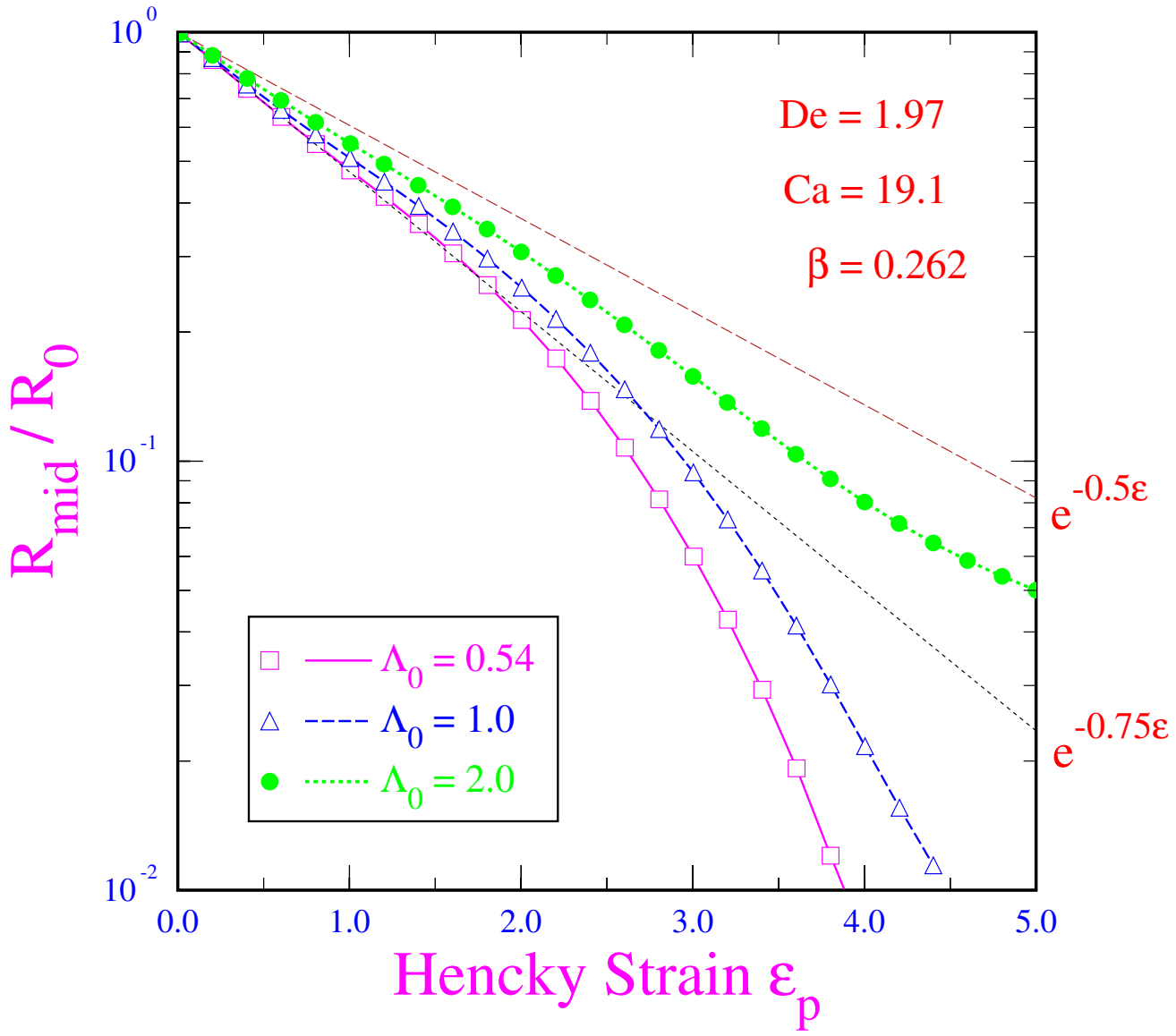
De = 1.97
Ca = 19.1
β = 0.262
Λ_0 = 0.54
Λ_0 = 1.0
Λ_0 = 2.0
$e^{-0.5\varepsilon}$
$e^{-0.75\varepsilon}$
R_{mid} / R_0
Hencky Strain ε_p
10^0
10^{-1}
10^{-2}
0.0
1.0
2.0
3.0
4.0
5.0

Figure 15

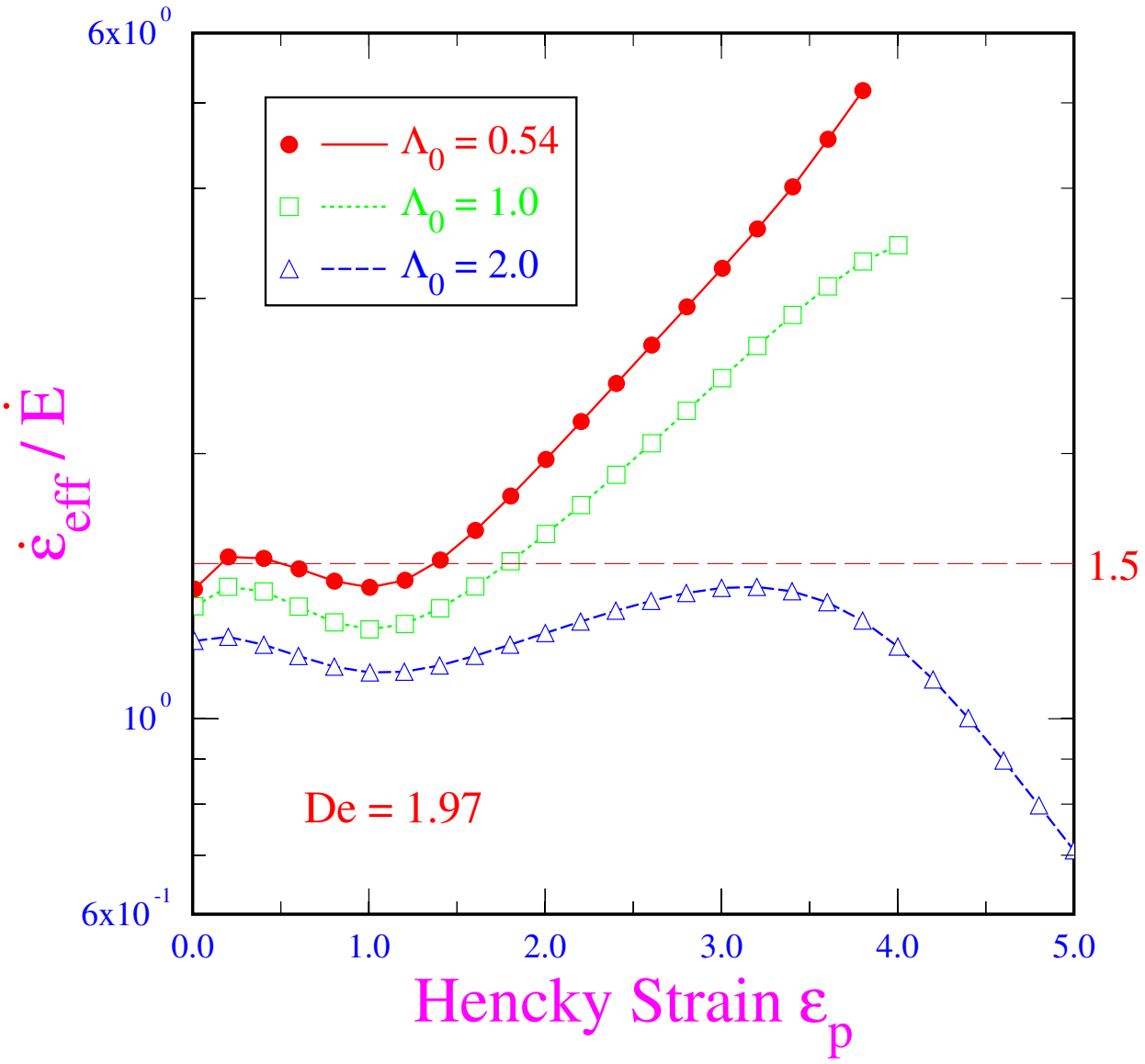
6x10^0
10^0
6x10^-1
0.0
1.0
2.0
3.0
4.0
5.0
Λ0 = 0.54
Λ0 = 1.0
Λ0 = 2.0
De = 1.97
1.5
ε̇eff / Ė
Hencky Strain εp

Figure 16

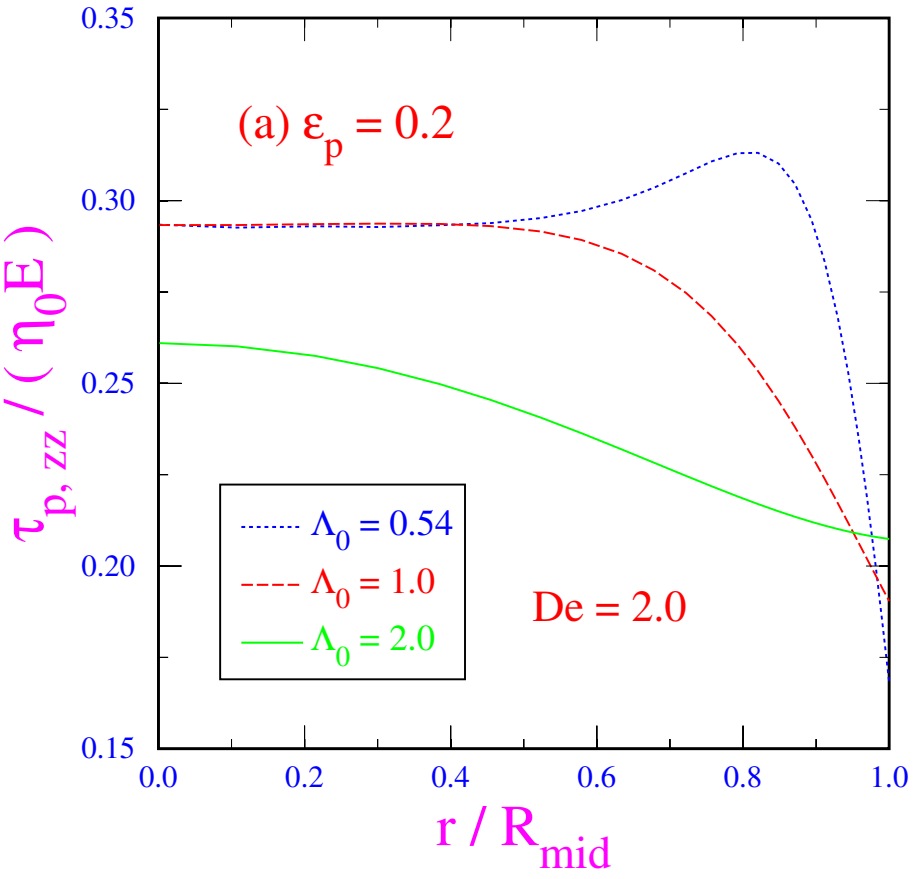
(a) $\varepsilon_p = 0.2$
$\Lambda_0 = 0.54$
$\Lambda_0 = 1.0$
$\Lambda_0 = 2.0$
De = 2.0
$\tau_{p,zz} / (\eta_0 \dot{E})$
r / R_{mid}
0.35
0.30
0.25
0.20
0.15
0.0
0.2
0.4
0.6
0.8
1.0

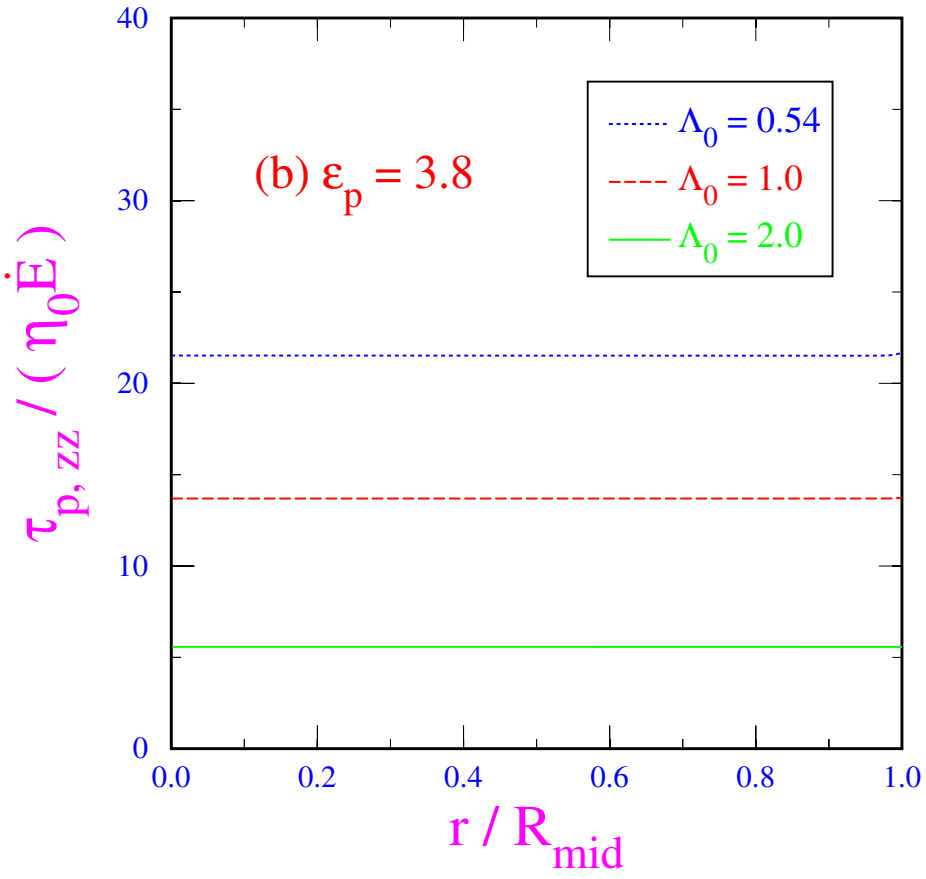
(b) $\varepsilon_p = 3.8$
$\Lambda_0 = 0.54$
$\Lambda_0 = 1.0$
$\Lambda_0 = 2.0$
$\tau_{p,zz} / (\eta_0 \dot{E})$
r / R_{mid}
40
30
20
10
0
0.0
0.2
0.4
0.6
0.8
1.0

Figure 17

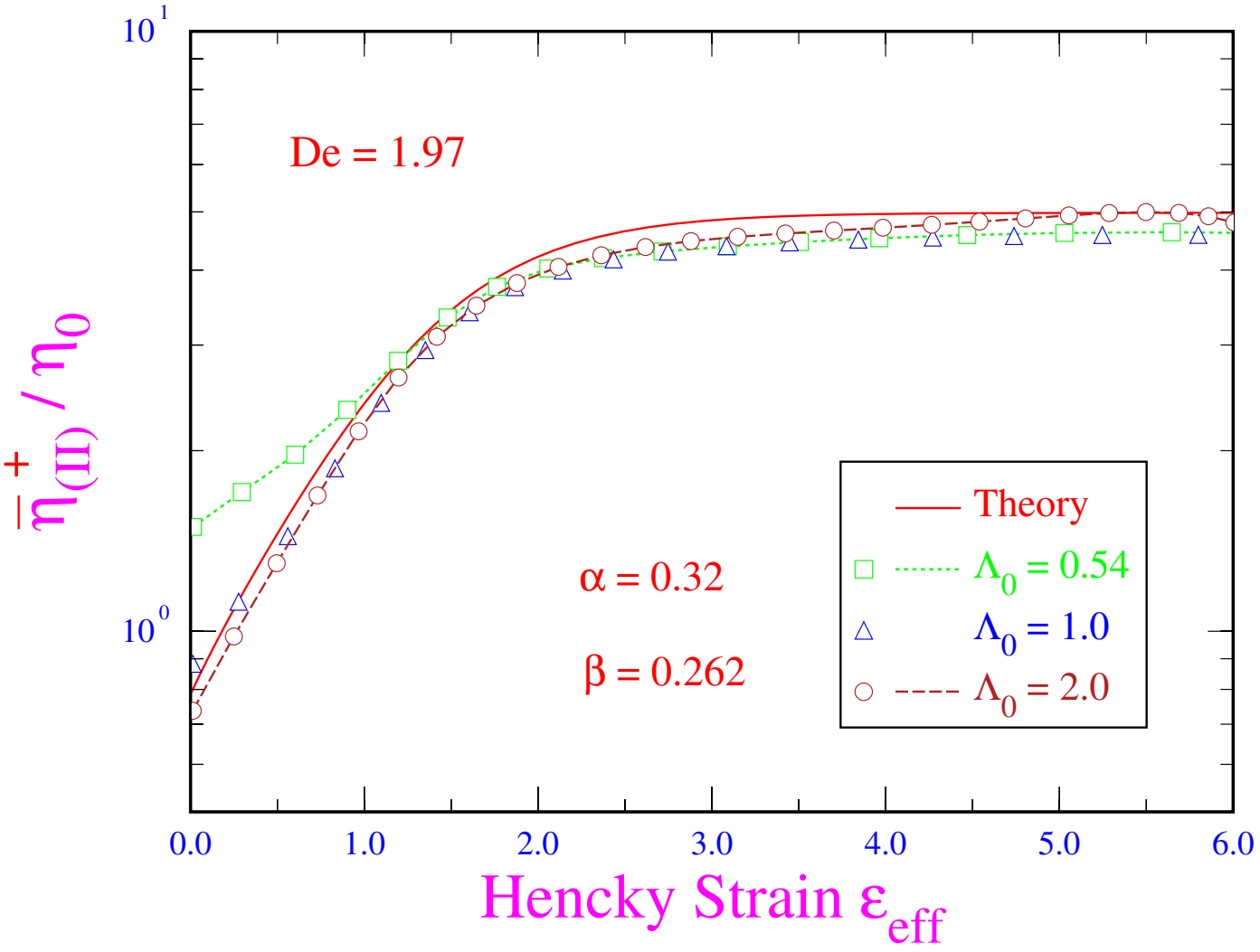
De = 1.97
α = 0.32
β = 0.262
Theory
Λ0 = 0.54
Λ0 = 1.0
Λ0 = 2.0
10^1
10^0
0.0
1.0
2.0
3.0
4.0
5.0
6.0
η+(II) / η0
Hencky Strain εeff

Figure 18

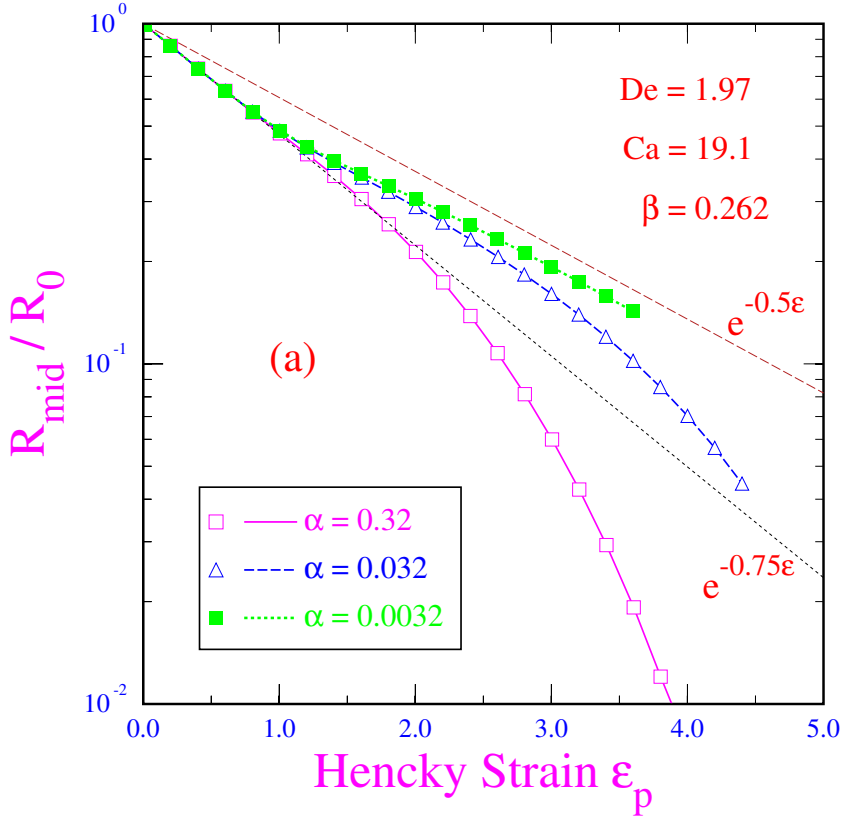
De = 1.97
Ca = 19.1
β = 0.262
(a)
α = 0.32
α = 0.032
α = 0.0032
e^-0.5ε
e^-0.75ε
R_mid / R_0
Hencky Strain ε_p

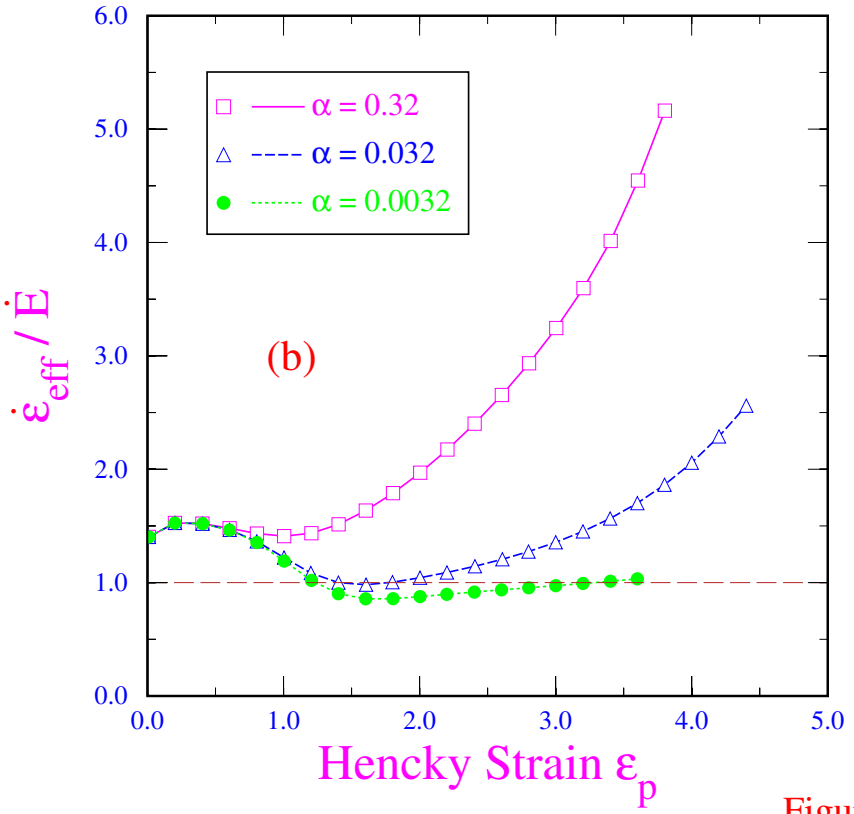
(b)
α = 0.32
α = 0.032
α = 0.0032
ε̇_eff / Ė
Hencky Strain ε_p

Figure 19

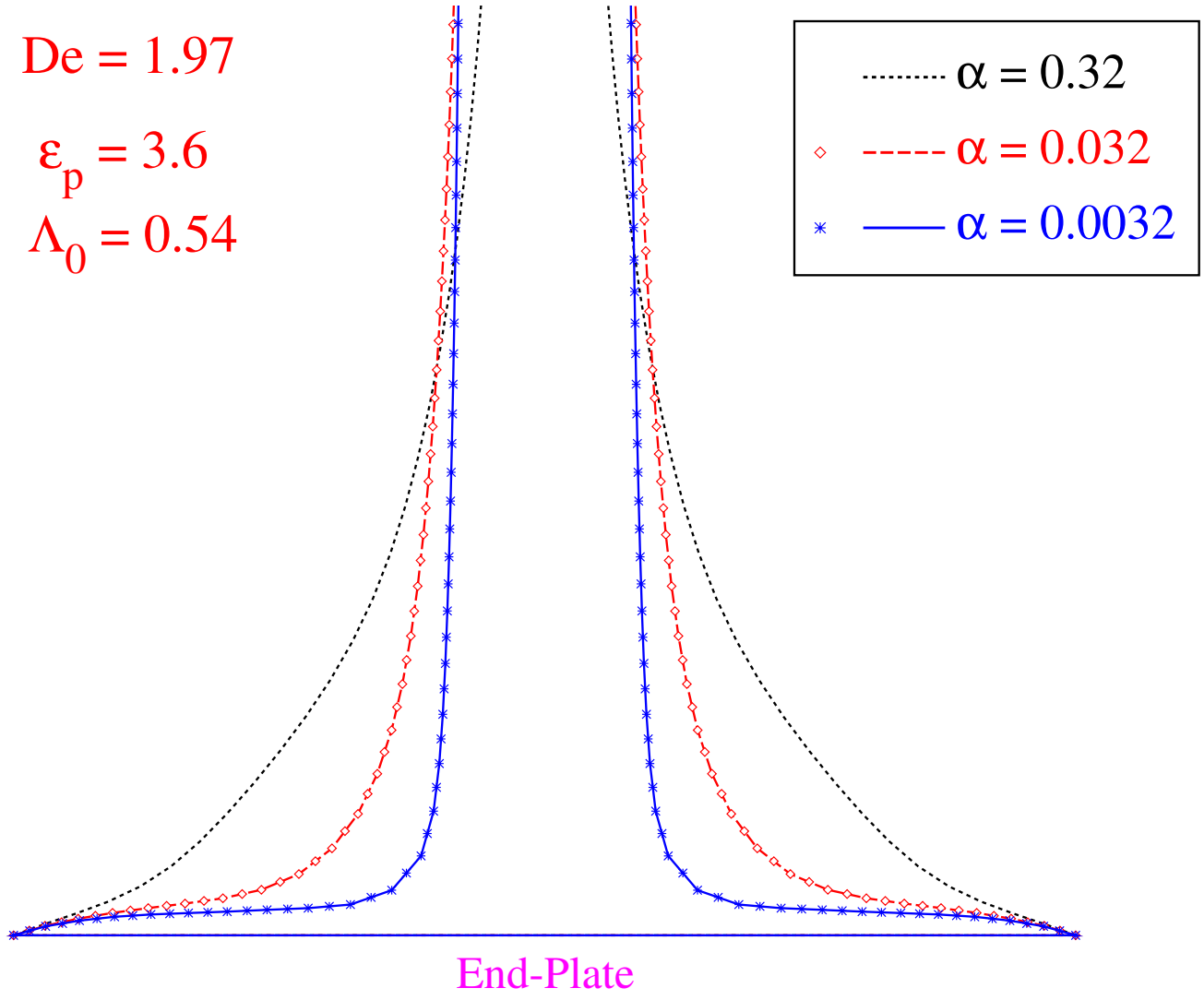
De = 1.97
$\varepsilon_p = 3.6$
$\Lambda_0 = 0.54$
α = 0.32
α = 0.032
α = 0.0032
End-Plate

Figure 20

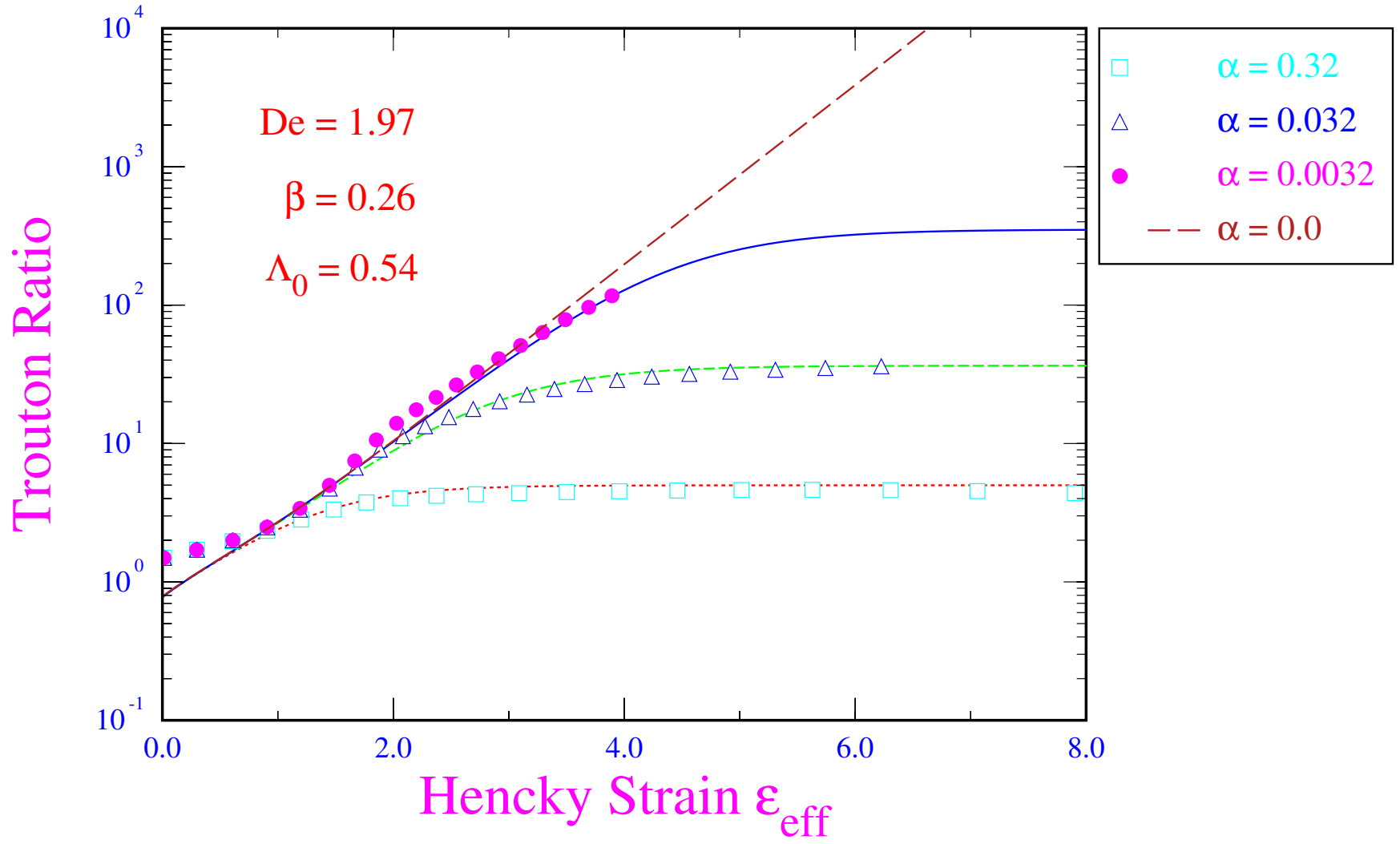
Trouton Ratio
Hencky Strain ε_{eff}
De = 1.97
β = 0.26
Λ_0 = 0.54
α = 0.32
α = 0.032
α = 0.0032
α = 0.0
10^4
10^3
10^2
10^1
10^0
10^{-1}
0.0
2.0
4.0
6.0
8.0

Figure 21

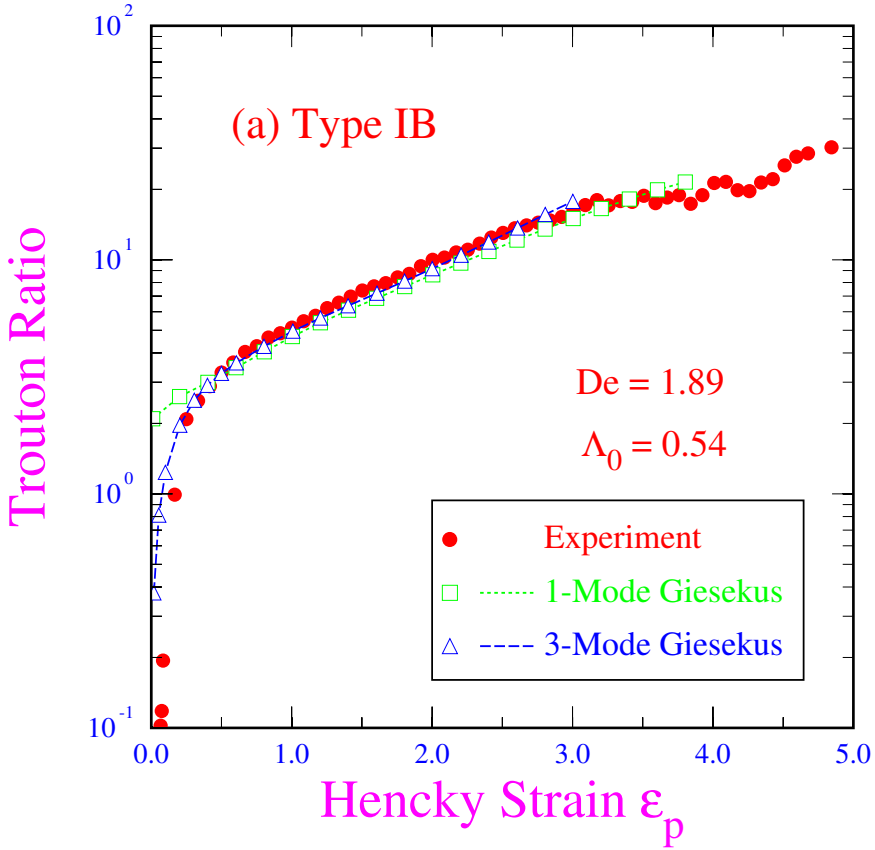
(a) Type IB
De = 1.89
Λ_0 = 0.54
Experiment
1-Mode Giesekus
3-Mode Giesekus
Trouton Ratio
Hencky Strain ε_p
10^2
10^1
10^0
10^{-1}
0.0
1.0
2.0
3.0
4.0
5.0

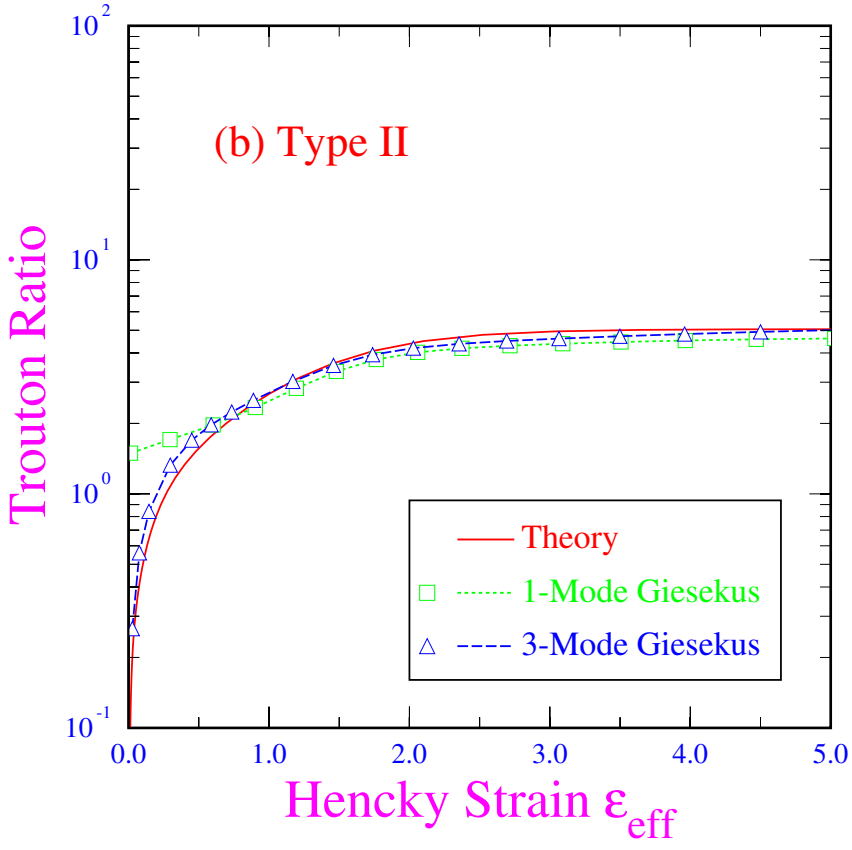
(b) Type II
Theory
1-Mode Giesekus
3-Mode Giesekus
Trouton Ratio
Hencky Strain ε_{eff}
10^2
10^1
10^0
10^{-1}
0.0
1.0
2.0
3.0
4.0
5.0

Figure 22

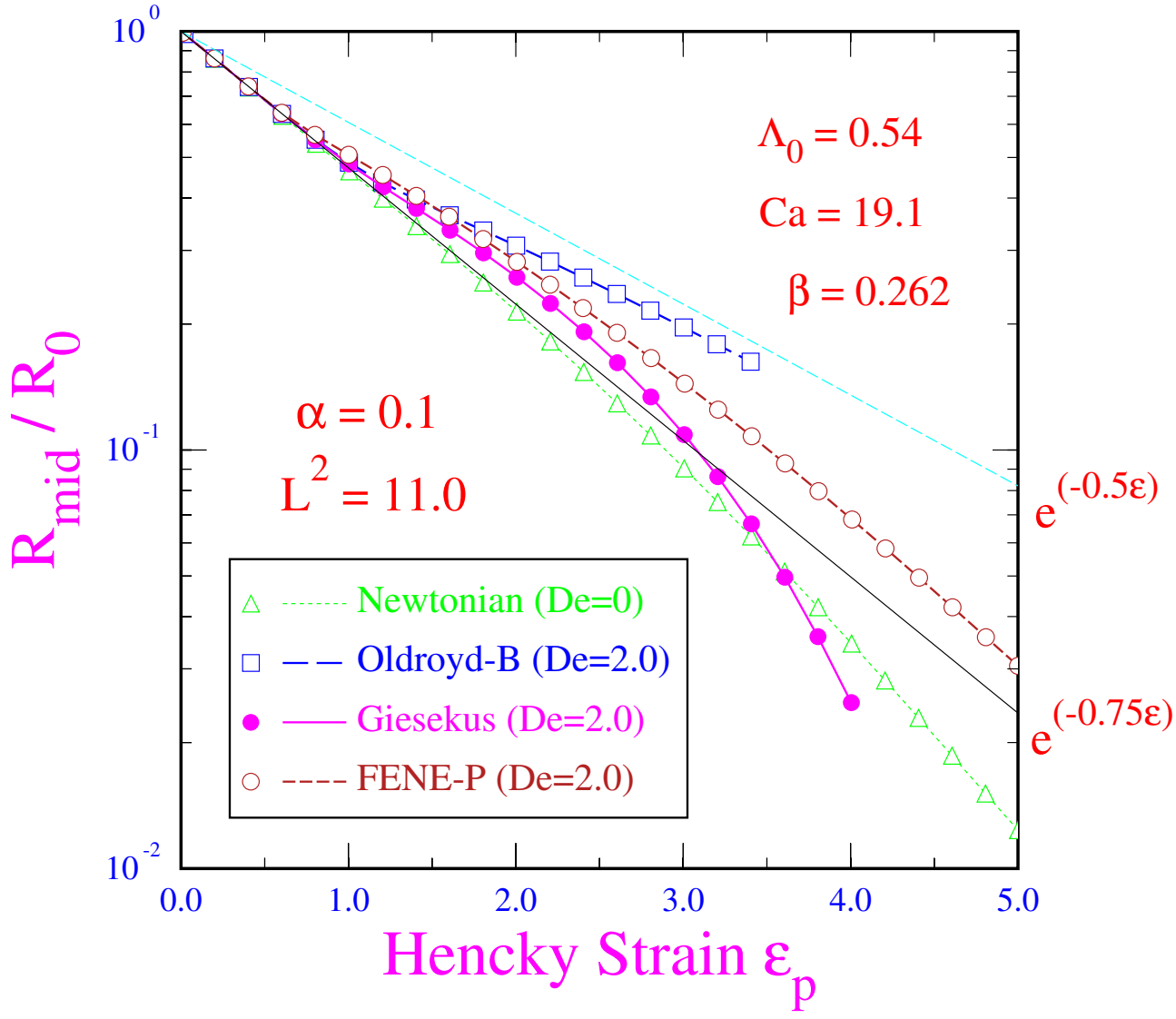
10^0
10^{-1}
10^{-2}
R_{mid} / R_0
$\Lambda_0 = 0.54$
Ca = 19.1
$\beta = 0.262$
$\alpha = 0.1$
$L^2 = 11.0$
Newtonian (De=0)
Oldroyd-B (De=2.0)
Giesekus (De=2.0)
FENE-P (De=2.0)
$e^{(-0.5\varepsilon)}$
$e^{(-0.75\varepsilon)}$
0.0
1.0
2.0
3.0
4.0
5.0
Hencky Strain ε_p

Figure 23

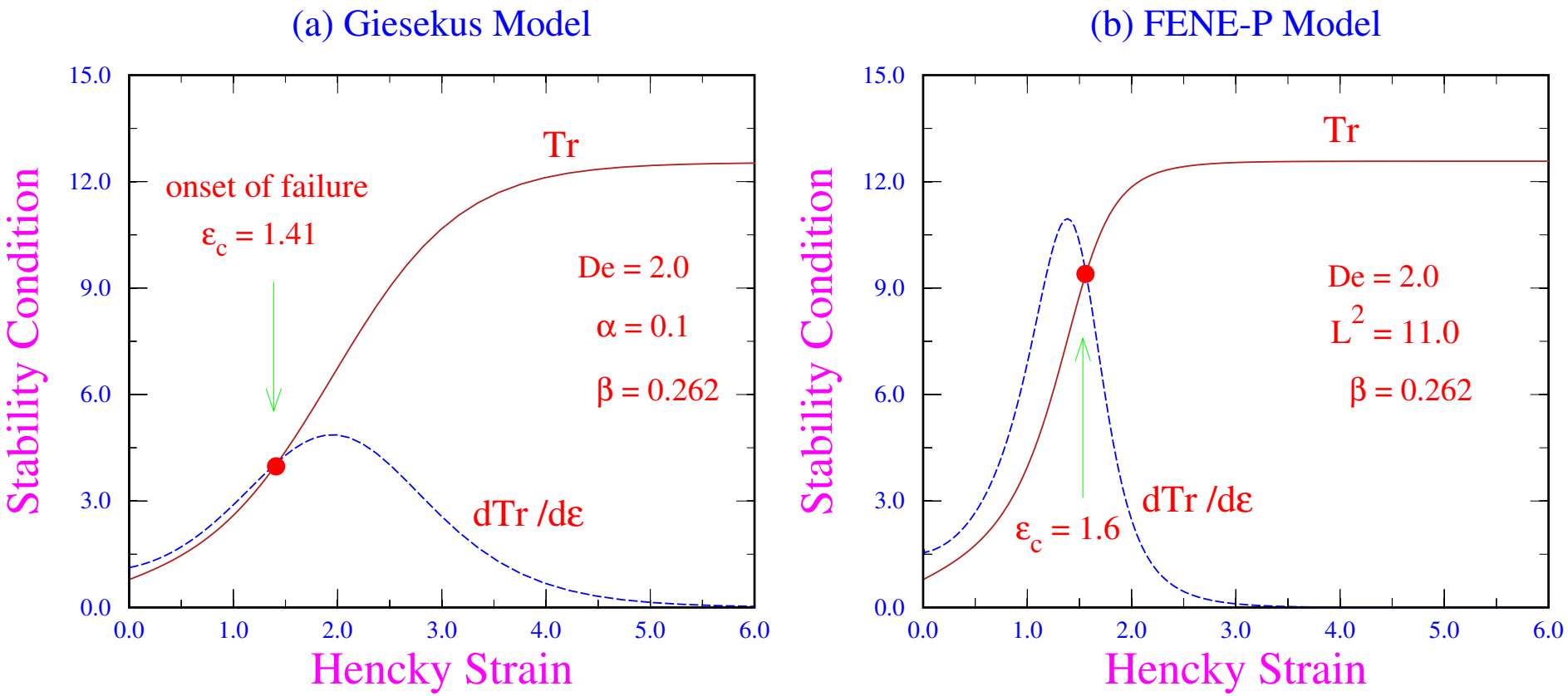
(a) Giesekus Model
(b) FENE-P Model
Stability Condition
Hencky Strain
Tr
dTr /dε
onset of failure
ε_c = 1.41
De = 2.0
α = 0.1
β = 0.262
L^2 = 11.0
ε_c = 1.6
0.0
3.0
6.0
9.0
12.0
15.0
1.0
2.0
4.0
5.0

Figure 24

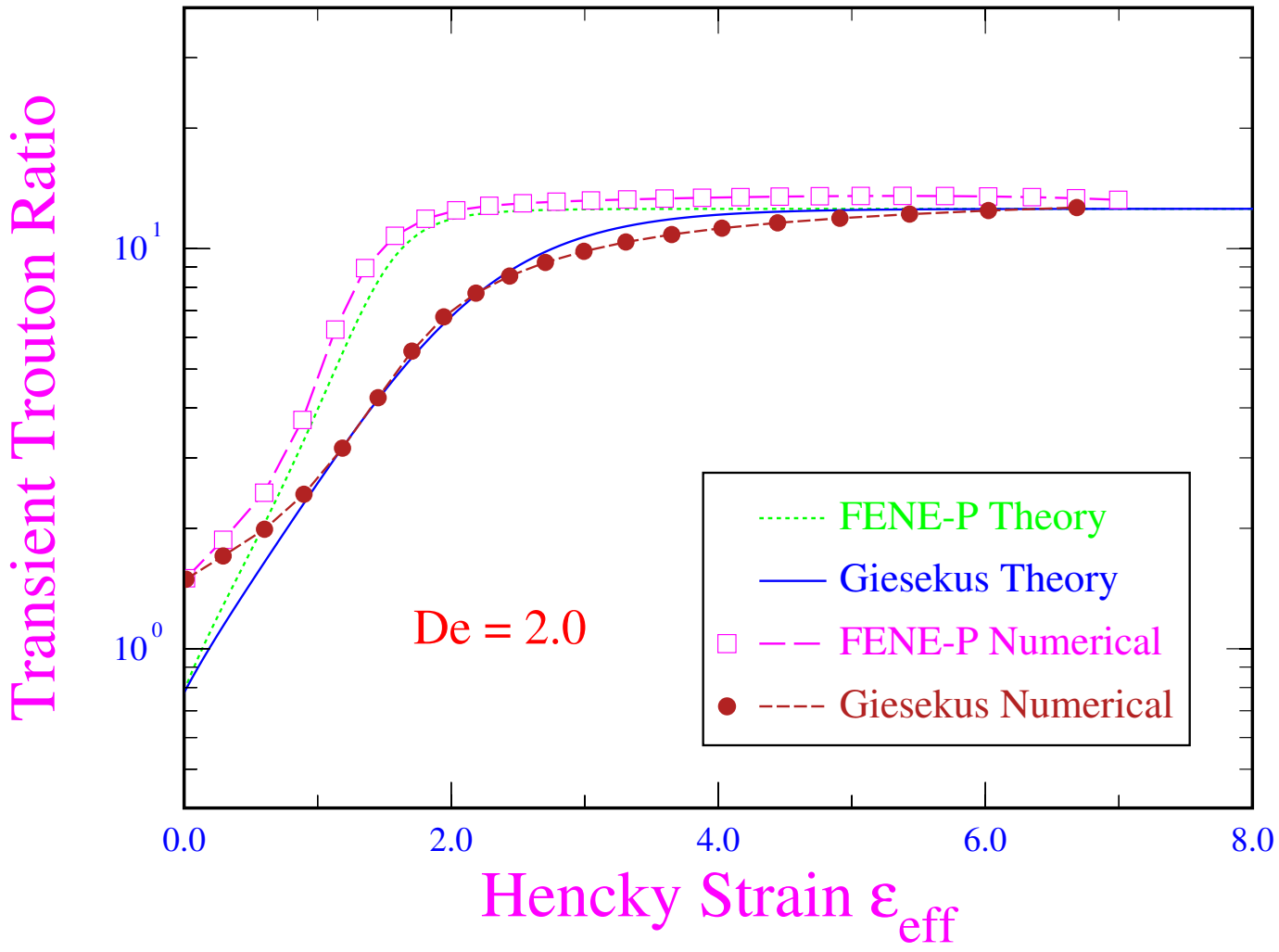
Transient Trouton Ratio
10^1
10^0
0.0
2.0
4.0
6.0
8.0
Hencky Strain ε_{eff}
De = 2.0
FENE-P Theory
Giesekus Theory
FENE-P Numerical
Giesekus Numerical

Figure 25

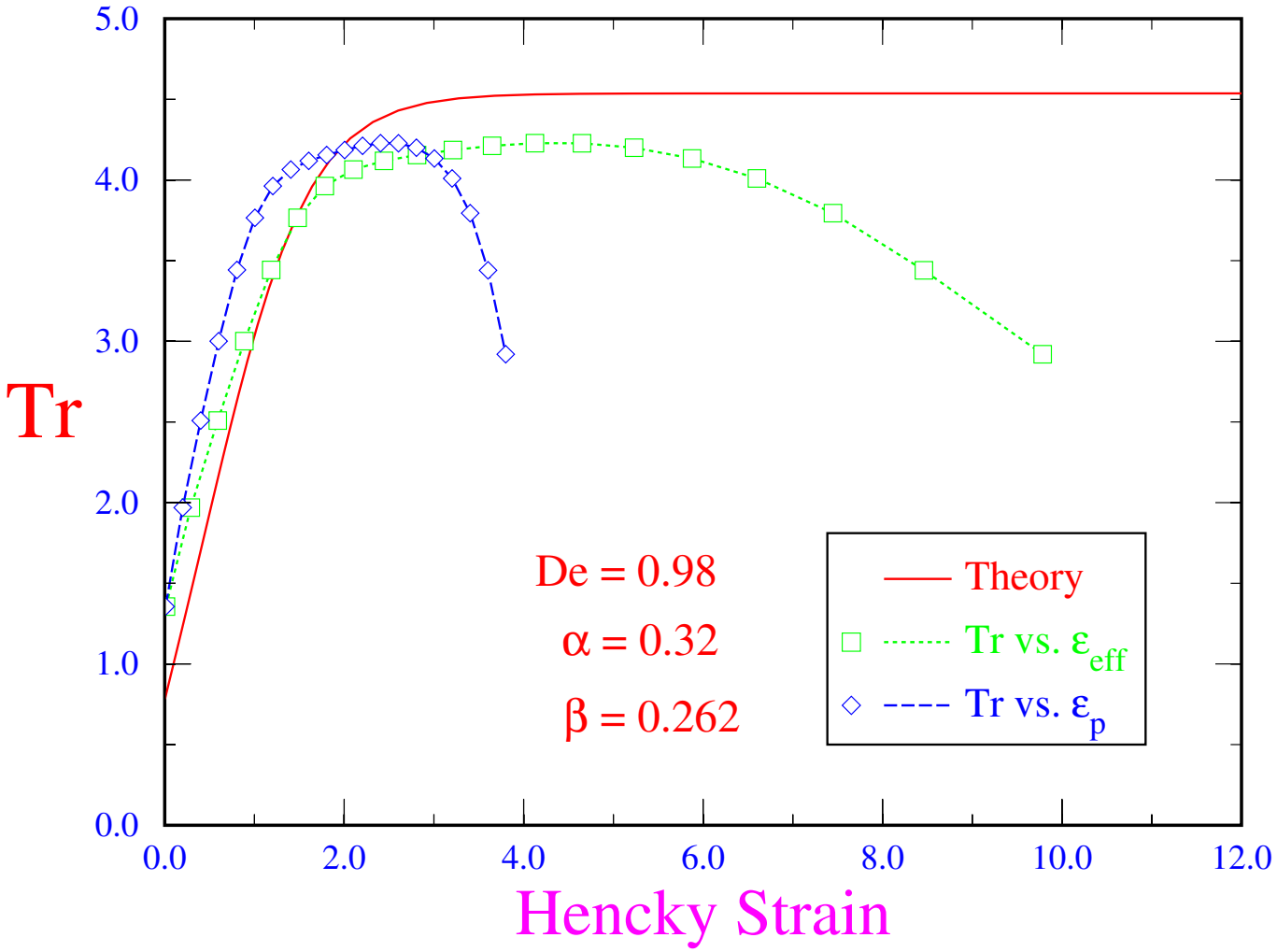
5.0
4.0
3.0
2.0
1.0
0.0
Tr
0.0
2.0
4.0
6.0
8.0
10.0
12.0
Hencky Strain
De = 0.98
α = 0.32
β = 0.262
Theory
Tr vs. ε_eff
Tr vs. ε_p

Figure 26